

Hydrodynamic Characterization of an Arterial Flow Bioreactor

Elizabeth Elena Voigt

Thesis submitted to the faculty of the Virginia Polytechnic Institute and State University in
partial fulfillment of the requirements for the degree of

Master of Science
In
Mechanical Engineering

Pavlos P. Vlachos
M. Nichole Rylander
Cameron D. Tropea
Peter F. Pelz

July 14, 2010
Blacksburg, Virginia, USA

Keywords: PIV, bioreactor, arterial flow, wall shear stress

Copyright © 2010 by Elizabeth Voigt

Hydrodynamic Characterization of an Arterial Flow Bioreactor

Elizabeth Elena Voigt

ABSTRACT

An *in vitro* arterial flow bioreactor system for the generation of physiological flows in a biological environment was designed, constructed, and characterized. The design was based on models previously used to investigate the response of endothelial cells to shear. The model interfaces a bioreactor with flow elements to compose a flow loop that reproduces arterial flow conditions within the bioreactor. High-resolution (8.6 microns) time-resolved (4 ms) velocity field measurements within the bioreactor were obtained using Particle Image Velocimetry (PIV). Two physiological flows were considered, corresponding to medium human arteries at rest and exercise conditions: first, with an average Reynolds number of 150 and a Womersley parameter of 6.4, and second, with an average Reynolds number of 300 and a Womersley parameter of 9.0. Two cases were considered: first, using a smooth artery section, and second, with a confluent layer of human microvascular endothelial cells grown on the inner surface of the artery section. The instantaneous wall shear stress, time-averaged wall shear stress, and oscillatory shear index were computed from the velocity field measurements and compared for the cases with and without cells. These measurements were used to assess the value of the system for measurement of correlations between fluid dynamics and the response of biological tissue. It was determined that the flow present in such a system is not an accurate reproduction of physiological flow, and that direct measurement of the flow is necessary for accurate quantification of cellular response to fluid parameters.

Hydrodynamic Characterization of an Arterial Flow Bioreactor

Elizabeth Elena Voigt

ABSTRACT

Ein *in vitro* Arterienströmungsbioreaktor für die Erzeugung physiologischer Strömung in einer biologischen Umgebung wurde konstruiert und charakterisiert. Die Konstruktion wurde nach vorliegenden Modellen zur Untersuchung der Reaktion von Endothelzellen auf Scherspannung entwickelt. Die Modelle koppeln einen Bioreaktor an Strömungselemente um einen Strömungskreis zu gestalten, der arterielle Strömungsbedingungen innerhalb des Bioreaktors nachbildet. Hochauflösende ($8,6\ \mu\text{m}$) zeitaufgelöste ($4\ \text{ms}$) Geschwindigkeitsfeldmessungen innerhalb des Bioreaktors wurden mit „Particle Image Velocimetry“ (PIV) gemacht. Zwei physiologische Strömungen wurden betrachtet, die mittelgroßen menschlichen Arterien bei Ruhe und Aktivität entsprechen: die erste mit einer durchschnittlichen Reynoldszahl von 150 und einer Womersleyzahl von 6,4, und die zweite mit einer durchschnittlichen Reynoldszahl von 300 und einer Womersleyzahl von 9,0. Zwei Fälle wurden auch betrachtet: die erste mit einem glatten Arterienprofil, und die zweite mit einer konfluenten Schicht menschlicher Mikrogefäßzellen auf der inneren Seite der Blutgefäß. Die unmittelbare Wandscherspannung, zeitgemittelte Wandscherspannung, und oszillierende Spannungsindex wurden aus den Geschwindigkeitsfeldmessungen berechnet und für die Fälle mit Zellen und ohne Zellen verglichen. Diese Größen wurden zur Bewertung des Systems für Messungen des Zusammenhangs zwischen der Strömungsdynamik und der Reaktion biologischer Gewebe benutzt. Es wurde festgestellt, dass die Strömung innerhalb eines solchen Reaktors keine richtige Reproduktion physiologischer Strömung ist, und dass direkte Messungen der Strömung benötigt werden, um die Reaktion der Zellen auf Strömungsparametern quantitativ zu bestimmen.

Acknowledgements

I would like to thank everyone who has helped me reach this point in my studies, but the resulting list would be longer than the thesis itself. So, in the interests of document length, I will here acknowledge only those who particularly assisted with this work. Special thanks are due:

To my advisors at Virginia Tech, Dr. Pavlos Vlachos and Dr. Nichole Rylander, for directing a lost masters' student and always providing just the right amount of guidance,

To my advisors at the TU Darmstadt, Dr. Tropea and Dr. Pelz, for being willing to work with a different sort of masters' thesis and a student an ocean away,

To Cara Buchanan, for coaxing suicidal endothelial cells to hang in there just long enough for PIV,

To Jaime Schmieg, for translating the PIV of journal articles into the PIV of experiments,

To everyone in AETHER and ICTAS, for being generous with hoards of amplifiers and media, for sharing and demystifying code, and for knowing everything about anything and taking the time to explain something,

And finally to Dr. Jan-Helge Bøhn and Dr. Manfred Hampe, without whom this dual degree would not even exist.

Declaration of Originality – Erklärung

I hereby affirm that I have prepared this Master Thesis without third party assistance and that I have used only the sources and resources stated. All information obtained from an external source has been identified as such. This work has not been provided in the same or in a similar form to any other examination board.

Hiermit versichere ich, die vorliegende Master Thesis ohne Hilfe Dritter nur mit den angegebenen Quellen und Hilfsmitteln angefertigt zu haben. Alle Stellen, die den Quellen entnommen wurden, sind als solche kenntlich gemacht worden. Diese Arbeit hat in gleicher oder ähnlicher Form noch keiner Prüfungsbehörde vorgelegen.

Blacksburg, 14 July 2010



Elizabeth Voigt

Table of Contents

Acknowledgements	iv
Declaration of Originality – Erklärung	v
Table of Contents	vi
List of Figures	vii
List of Tables	viii
List of Abbreviations and Symbols	ix
1 Introduction	1
1.1 Motivation	1
1.2 State of Research	4
1.3 Present Work	6
2 Design and Testing of an Arterial Flow Bioreactor	7
2.1 Introduction	7
2.2 System Design	11
2.2.1 Bioreactor	11
2.2.2 Flow Components	15
2.2.3 Instrumentation	19
2.3 Global Flow Parameters	21
2.4 Summary	22
3 Particle Image Velocimetry of an Arterial Flow Bioreactor	23
3.1 Introduction	23
3.2 Experimental Methods	25
3.2.1 Endothelial Layer	25
3.2.2 PIV System	32
3.2.3 PIV Processing	35
3.3 Results and Discussion	38
3.3.1 Case without cell layer	41
3.3.2 Case with cell layer	44
3.3.3 Error Analysis	52
3.3.4 Estimation of PIV Error	53
4 Conclusions and Recommendations	57
References	59
Appendix A: Additional Pressure Data	64
Appendix B: Additional Figures	68
B.1 Time Variation of Velocity and Instantaneous WSS	68
B.2 Statistical Variation of OSI and Time-Averaged WSS	78

List of Figures

Figure 1: Metastasis cascade. (Alberts 2002) (with permission).....	2
Figure 2: Drug targeting by antibody targeting of intravascularly injected drug-laden particles...	3
Figure 3: Wake Forest bioreactor. (Yazdani and Berry 2009) (with permission)	12
Figure 4: Bioreactor in refraction box.	15
Figure 5: Pressure reservoir.	17
Figure 6: Pulse dampener.....	18
Figure 7: Bioreactor flow loop.....	19
Figure 8: LabVIEW VI front panel.....	20
Figure 9: Pressure and flow for center of vessel with no cells present.	21
Figure 10: Diagram of basic PIV experiment. (Raffel 2007)	23
Figure 11: HMEC-1 on FEP sheet.	27
Figure 12: Bioreactor on motor shaft.....	28
Figure 13: HMEC-1 on FEP tubing.....	31
Figure 14: Laser plane passing through vessel cross-section.	32
Figure 15: Diagram of PIV synchronization.....	33
Figure 16: Imaging locations in vessel (mm).	34
Figure 17: Bright field image (left) and corresponding mask (right).	36
Figure 18: Time-averaged WSS and OSI for quasi-steady case.....	39
Figure 19: $Re \sim 150$ pulsatile flow; no cells; peak flow ($t = 0$).	40
Figure 20: $Re \sim 150$ pulsatile flow; no cells; $t = T/4$	42
Figure 21: $Re \sim 150$ pulsatile flow; no cells; $t = T/2$	42
Figure 22: $Re \sim 150$ pulsatile flow; no cells; $t = 3T/4$	42
Figure 23: Time-averaged WSS and OSI for $Re \sim 150$ pulsatile flow; no cells.	43
Figure 24: Time-averaged WSS and OSI for $Re \sim 300$ pulsatile flow; no cells.	43
Figure 25: Bright field images of vessel without cells (top) and with cells (bottom).	44
Figure 26: Particle images of vessel with cells.	45
Figure 27: Time-averaged WSS and OSI for $Re \sim 150$ pulsatile flow; with cells.....	46
Figure 28: $Re \sim 150$ pulsatile flow; with cells; peak flow ($t=0$).	47
Figure 29: Time-averaged WSS and OSI for $Re \sim 300$ pulsatile flow; with cells.....	48
Figure 30: Statistical distribution of top wall time-averaged WSS at location A.....	49
Figure 31: Statistical distribution of bottom wall time-averaged WSS at location A.	49
Figure 32: Statistical distribution of top wall OSI at location A.	50
Figure 33: Statistical distribution of bottom wall OSI at location A.	50
Figure 34: Statistical distribution of top wall OSI at location C.....	51
Figure 35: Statistical distribution of bottom wall OSI at location C.	51

List of Tables

Table 1: Summary of bioreactor and physiological flow loop literature.	9
Table 2: Comparison of vessel materials and fluids used in PIV experiments.	13
Table 3: Properties of FEP.	14
Table 4: Range of Reynolds and Womersley numbers attainable with available equipment.	16
Table 5: Experimental parameters for waveforms in Figure 9.	22
Table 6: alamarBlue assay results.	29
Table 7: PIV processing parameters.	36
Table 8: Error estimation parameters.	56

List of Abbreviations and Symbols

Abbreviation	Description
BSA	bovine serum albumin
DAQ	data acquisition
DWO	discrete window offset
EC	endothelial cell
EtO	ethylene oxide
FBS	fetal bovine serum
FEP	fluorinated ethylene propylene
FFT	fast Fourier transform
HMEC	human microvascular endothelial cell
ID	inside diameter
LVAD	left ventricular assist device
MAP	mean arterial pressure
μ PIV	microscopic particle image velocimetry
OSI	oscillatory shear index
PCB	printed circuit board
PIV	particle image velocimetry
RBC	red blood cell
RPC	robust phase correlation
RI	refractive index

RPM	revolutions per minute
VI	virtual instrument
WSS	wall shear stress

The first column of the following table lists the symbols used in this thesis for physical and mathematical parameters. A brief description of each is provided in the second column, while the third column gives the dimension (if any) of the parameter using the non-specific base units mass [M], length [L], and time [T].

Symbol	Description	Dimension
α	Womersley number	
ε	measurement uncertainty	
η	dynamic viscosity	$[M][L]^{-1}[T]^{-1}$
ν	kinematic viscosity	$[L]^2[T]^{-1}$
$\tau(r)$	radially-dependent shear stress	$[M][L]^{-1}[T]^{-2}$
$\tau_w(x,t)$	instantaneous wall shear stress	$[M][L]^{-1}[T]^{-2}$
$\overline{\tau_w}(x)$	time-averaged wall shear stress	$[M][L]^{-1}[T]^{-2}$
ω	angular frequency	$[T]^{-1}$
$A_{entrance}$	cross-sectional area of vessel inlet	$[L]^2$
A_{vessel}	vessel cross-sectional area	$[L]^2$
D	vessel diameter	$[L]$
H	image height	$[L]$
MAP	mean arterial pressure	$[M][L]^{-1}[T]^{-2}$

P	pressure	$[M][L]^{-1}[T]^{-2}$
P_{dias}	diastolic pressure	$[M][L]^{-1}[T]^{-2}$
P_{sys}	systolic pressure	$[M][L]^{-1}[T]^{-2}$
q	volumetric flow rate	$[L]^3[T]^{-1}$
r	radial position	[L]
R	vessel radius	[L]
Re	Reynolds number	
t	time	[T]
Δt	interframe time between paired images	[T]
T	image pair period (inverse of frequency)	[T]
T_w	wave duration	[T]
u_{avg}	mean longitudinal velocity	$[L][T]^{-1}$
$u(r)$	longitudinal velocity	$[L][T]^{-1}$
x	axial position	[L]
x^*	nondimensional axial coordinate	
y^*	nondimensional radial coordinate	

1 Introduction

1.1 Motivation

The study of physiological flows is a multidisciplinary field of research with a wide range of biomedical applications. These flows bridge the gap between applied science (fluid mechanics) and life science (biological and chemical interactions). Fluid-mechanical characterization of physiological flows can not only lead to a better understanding of many biological phenomena such as cardiovascular disease and cancer metastasis, but can also be applied to the design of better medical drug targeting and delivery systems.

Cancer and cardiovascular system disorders, including heart disease and stroke, cause nearly 60% of deaths each year in the U.S. (CDC 2010). To better understand the mechanisms causing these diseases, the underlying vascular flow must be understood. The characterization of vascular flow is vital for better understanding, treatment, and prevention of many cardiovascular diseases.

Metastasis is a mechanism by which malignant tumors spread from the initial location to secondary sites. During metastasis, tumor cells detach from the primary tumor and enter the bloodstream, which distributes them throughout the body. A cascade of events occurs during metastasis, beginning with cell detachment and ending with secondary tumor growth at the new location (Figure 1) (Alberts 2002; Oppenheimer 2006). One of these events, the migration of cells from the tumor to a new site, cannot be adequately measured or predicted without detailed knowledge of the vascular flows involved.

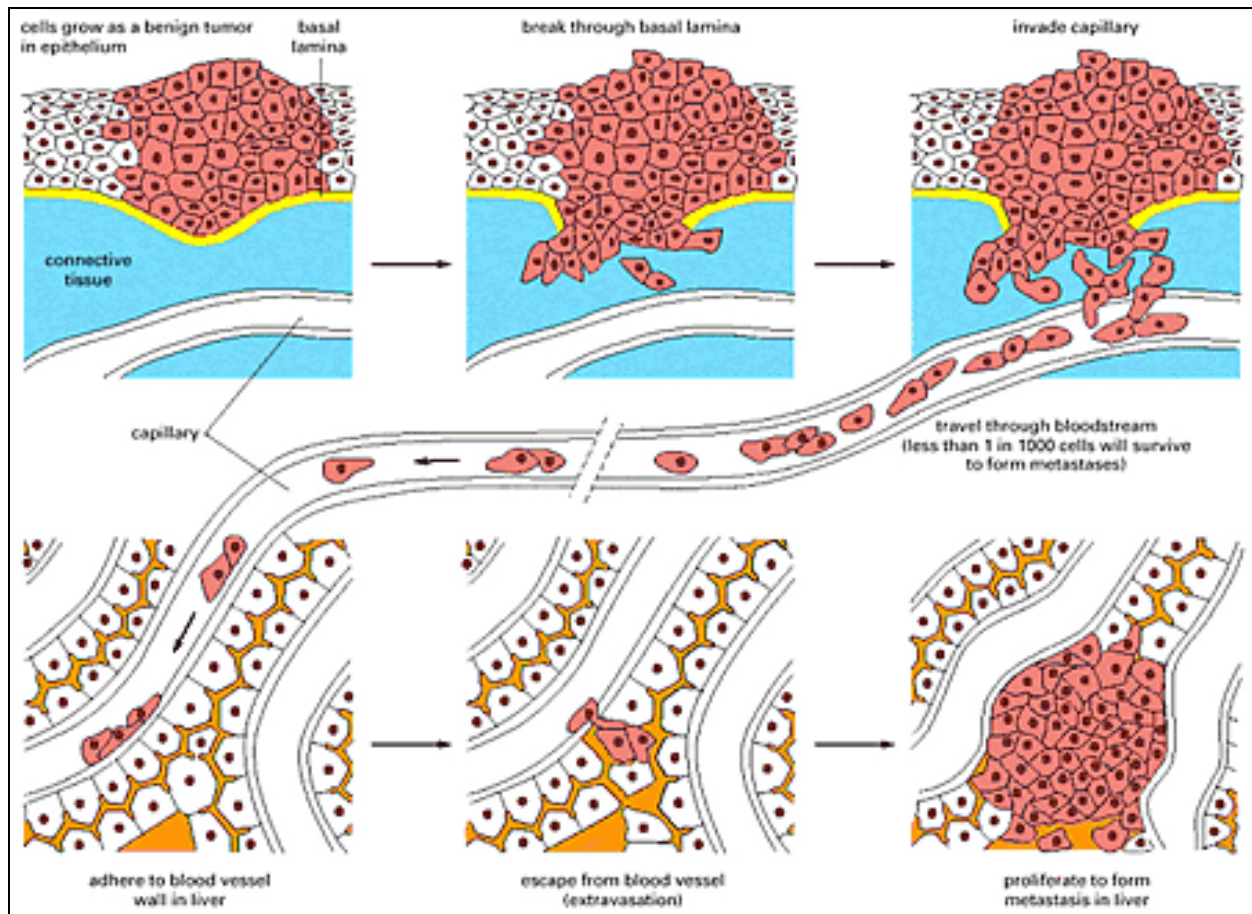


Figure 1: Metastasis cascade. (Alberts 2002) (with permission)

Physiological flow parameters include the pressures and stresses generated within the vascular system. These parameters strongly influence the physiology and function of vascular endothelial cells: the cells lining the inner wall of blood vessels (Levesque, Nerem et al. 1990; Ku 1997; Califano and Reinhart-King 2010). Variations in the shear stress experienced by endothelial cells affect many factors such as morphology, alignment with the flow, mechanical strength, rate of proliferation, and rate of gene expression (Reneman, Arts et al. 2006). Although it is known that these factors are dependent on the hemodynamics of the flow, the relationship has not been quantified. Accurate characterization and reproduction of vascular flow is necessary for controlled measurements of endothelial cell response under physiological conditions.

Drug delivery is an application of vascular fluid mechanics research with vast room for improvement. An extremely low percentage – 0.001% to 0.01% – of intravenous cancer antibodies actually reach their intended targets (Ferrari 2005). The cost to develop a new

medication is on the order of hundreds of millions of dollars (Langer 1990), and production of antibodies themselves is prohibitively expensive. Improving the efficacy of existing drugs is an attractive alternative to development of new drugs. Additionally, improving the efficacy of currently administered drugs would reduce dosage amounts, minimizing side effects and production costs (Langer 1998).

Targeted drug delivery is a field of research for the design of complete systems for the entry, transport, and delivery of drugs in the body. A basic method for drug entry is intravascular injection (Hajitou, Pasqualini et al. 2006). Mechanisms for efficient transport that are under investigation include encapsulation of drugs in polymers (Langer 1998) and filling hollow nanoparticles such as nanotubes with drugs (Ferrari 2005; Wickline, Neubauer et al. 2006). Ligands or antibodies can be attached to drug-laden particles, targeting them to specific receptors where the encased medicine is subsequently released (Murakami, Ajima et al. 2004; Neri and Bicknell 2005; Ajima, Murakami et al. 2008; Banquy, Leclair et al. 2008). Figure 2 is a schematic representation of possible processes in drug targeting.

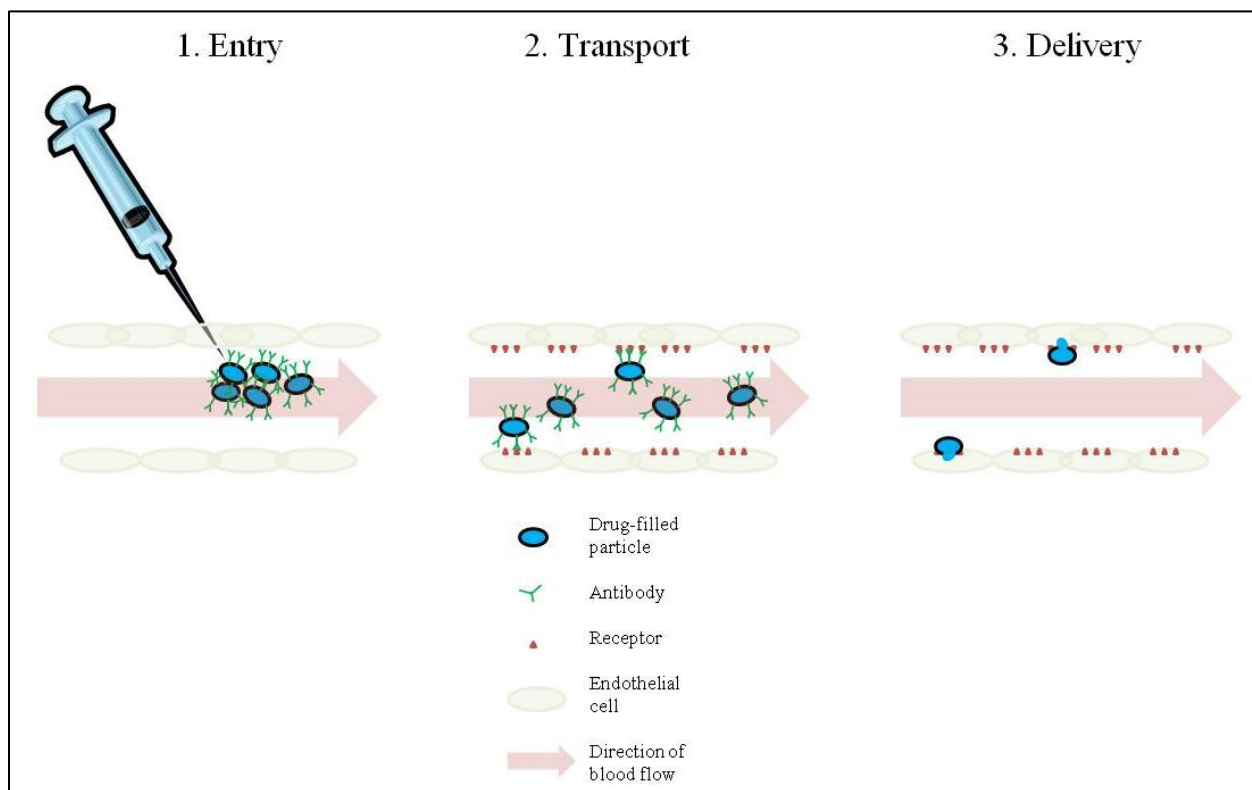


Figure 2: Drug targeting by antibody targeting of intravascularly injected drug-laden particles.

Because targeted delivery systems can be designed to treat a wide range of diseases, they are the focus of much current biomedical research. Design of the transport mechanism requires first a comprehensive knowledge of the vascular flows carrying the drug-loaded particles.

Additionally, it requires the ability to parametrically vary the delivery system and measure the effect on transport within physiological flow. For this to be possible, a well-controlled system for vascular flow must be available.

1.2 State of Research

There are generally three approaches to solve any engineering problem: theory, computational models, and experiments; this discussion focuses each of these approaches as it has been applied to the study of vascular flow. Although much theory has been developed for blood flow, it is generally only applicable to ideal or simplified flow situations. While standard laminar fluid theory is well understood, little is known about the influence of vascular biological interactions on the flow. The theory of vascular flow usually begins at the level of the most basic analytically solvable internal flow (Poiseuille flow), with various levels of complexity introduced until a sufficient level of detail is reached for meaningful results (Fung 1997). Poiseuille flow is the laminar flow of a Newtonian fluid in a straight rigid tube. Analytical solutions exist for both the velocity profile $u(r)$ and wall shear stresses $\tau_w(r)$ as functions of the radial position r . Other parameters in these solutions include the fluid viscosity η , the pressure gradient in the axial direction $\frac{\partial P}{\partial x}$, and the vessel radius R , (Equations (1) and (2)). The relationship for shear stress can also be expressed in terms of the volumetric flow rate q as seen in Equation (3).

$$u(r) = -\frac{1}{4\eta} \frac{\partial P}{\partial x} (R^2 - r^2) \quad (1)$$

$$\tau(r) = -\frac{r}{2} \frac{\partial P}{\partial x} \quad (2)$$

$$\tau(r) = \frac{4\eta \cdot q}{\pi \cdot r^3} \quad (3)$$

The assumption of Poiseuille flow is conventionally used to estimate the shear stresses experienced by vessel walls in vascular flow (Reneman, Arts et al. 2006; Poelma, Vennemann et al. 2008), but because blood vessels are neither rigid nor straight, and blood has non-Newtonian properties, many levels of complexity must be added to the Poiseuille solution before an accurate representation of vascular flow can be obtained (Fung 1997). The equations developed with the inclusion of these effects are adequate for estimates of flow properties and specific calculations, but still fail to fully describe the flow. This is because they do not represent the effects of biological phenomena both internal and external to the flow. One research group (Decuzzi, Lee et al. 2004; Decuzzi, Lee et al. 2005; Decuzzi and Ferrari 2006) has developed analytical solutions that include some effects due to biological interactions, but little or no experimental data exist to support their calculations.

Fluid models for vascular flow are generally developed at the level of lumped parameter models, which can be interpreted as electrical circuit models of fluid systems. Lumped parameter models replace vector fields with scalar values, assuming variability in only one dimension and permitting calculation of only average flow and resistance. These models are concerned with the distribution of flow within the vascular system, basing calculations on parameters such as elastance, resistance, viscoelastance, and inertance (Milisic and Quarteroni 2004; Cole, Lucas et al. 2005; Fernandez, Milisic et al. 2005; Liang and Liu 2005; Conlon, Russell et al. 2006; Khalil, Kerr et al. 2008). Although useful for global analysis of blood flow, lumped parameter models provide no insight into localized transport phenomena.

Experimental studies of vascular flow have, in some regards, clear benefits over theoretical and computational studies. All phenomena to be studied are present and need only be measured. Unfortunately, direct measurement of vascular flow *–in vivo* experimentation – is both expensive and time-consuming. The use of animal test subjects for experimentation is permitted only under strict procedural codes, and the costs of acquiring and caring for test subjects are high. Experimentation often requires sacrifice of the test subjects, which not only increases the cost per measurement but also requires large groups of subjects for statistically meaningful results (Liu, Davis et al. 2008; Yazdani and Berry 2009). The methods used for flow measurements *in vivo* are usually invasive, disturbing the flow to an unknown degree. Additionally, they are often technically difficult to put into practice and lack the desired level of detail.

Therefore, the need exists for a system that can make use of the advantages of each approach to the study of vascular flow while eliminating the disadvantages. The key advantage of experimental approaches is clear: phenomena can be quantified before the driving mechanisms are fully understood. Conversely, the primary benefit of theoretical approaches is the ease with which parameters can be controlled and varied. Experimental measurement using an *in vitro* model is a solution that combines the advantages of both approaches and retains few of their disadvantages. The *in vitro* model should reproduce as closely as possible the relevant physiological conditions while enabling a high level of parameter control and measurement accuracy.

1.3 Present Work

The goal of this masters' thesis is to design, build, and validate an *in vitro* model to enable measurement of physiological flows in a biological environment and correlation between the fluid dynamics and the physical response of the biological tissue. The system designed interfaces a bioreactor – a system that supports biological tissue – with fluid elements to create a bioreactor flow loop that can reproduce arterial flow conditions within the bioreactor. Chapter 2 of this work describes in detail the design of the system and the characterization of global flow parameters.

High-resolution time-resolved flow measurements within the bioreactor can be performed using a PIV (particle image velocimetry) system. PIV is nearly impossible to apply to *in vivo* experiments because it requires transparency and careful alignment of the measurement volume. However, it can be used with an *in vitro* system for robust and accurate velocity measurements because it is noninvasive and provides high spatial and temporal resolution. Chapter 3 describes the initial validation experiments performed in the bioreactor flow loop using PIV. In these experiments, PIV was used to measure the flow within the bioreactor for two cases: first, with a smooth artery section, and second, with a confluent layer of human microvascular endothelial cells (HMECs) grown on the inner surface of the bioreactor. The flow parameters with and without HMECs present were compared and the effect of the cellular layer on the flow was measured.

2 Design and Testing of an Arterial Flow Bioreactor

2.1 Introduction

A bioreactor is a device for *ex vivo* or *in vitro* tissue engineering. It provides a controlled environment that can support the growth of living tissues and can be used for biomedical experimentation. A Petri dish, for example, is a simple bioreactor. Functions of a bioreactor can include seeding of cells into the reactor, mass transport of nutrients to and waste from the cells, and mechanical conditioning of the tissue (Martin, Wendt et al. 2004). Many considerations go into the design of bioreactors, including chemical compatibility with the biological components, environmental control, ease of use, and sterilization.

Bioreactor flow loops are bioreactors connected to fluid-mechanical components that drive a fluid, usually cell growth media, through the bioreactor. These systems are already in use in a variety of forms in research groups around the world, and have been designed with a wide range of capabilities and intended applications. However, each of the existing bioreactor flow loops lacks features necessary for the flow characterization described here.

Most bioreactor flow loops are used in tissue engineering applications to generate approximately the flow environment necessary for support of cellular growth and mechanical conditioning of endothelial cells (ECs). One example is the flow loop developed by Conklin and Surowiec et al. (2000) which allows control of the physical environment in the bioreactor, pressure, and flow rate but does not allow measurement of flow conditions within the bioreactor. Other bioreactor flow loops are designed for the study of the effects of shear stress on the cell layer in the bioreactor. Many groups (Levesque, Nerem et al. 1990; Mironov, Kasyanov et al. 2003; Yazdani and Berry 2009; Yazdani, Tillman et al. 2010) report quantitative relationships between cell proliferation and morphology and applied flow conditions. However, these groups either use the conventional but inaccurate Poiseuille assumption to estimate the stress or do not attempt to report wall shear stresses and focus their analyses instead on the applied pressure.

Several groups have designed flow loops compatible with measurement systems such as PIV to allow direct visualization and measurement of flow profiles. However, these are generally not compatible with biological materials (Tanne, Bertrand et al. 2008; Burgmann, Grosse et al. 2009)

or do not accurately reproduce physiological conditions, using square microchannels instead of vessels with a circular profile (Rossi and Ekeberg 2006). A summary of the previous work in the areas of bioreactor flow loops and physiological flow measurements is found in Table 1.

The bioreactor flow loop developed here provides a compromise between accurate representation of physiological flow, compatibility with live tissue, ease of use, and cost. It has been designed using the laws of similitude to match the key features of arterial flow (Marassi, Castellini et al. 2004): the Reynolds number, the Womersley number, and the pressure profile. The Reynolds number Re is a dimensionless number that quantifies the relationship between inertial (velocity-based) and viscous (viscosity-based) forces in the flow (Equation (4)). It can be defined using either the peak or the average velocity. Here the Reynolds number based on the average flow velocity u_{avg} , vessel diameter D , and kinematic viscosity ν will be used.

$$Re = \frac{u_{avg} D}{\nu} \quad (4)$$

This bioreactor flow loop was designed with the scale of a medium-sized artery with a vessel diameter of 4.57 mm, a typical value for human coronary, mesenteric, or femoral arteries (Lin, Chen et al. 2000). Values for the Reynolds number in this type of artery are reported to range between 100 and 1000 (Ku 1997; Gray, Owen et al. 2007; Vennemann, Lindken et al. 2007). This range of Reynolds numbers is well within the laminar regime. Because red blood cells (RBCs) have a typical diameter of 10 μm , non-Newtonian effects of RBC margination and aggregation on blood viscosity can typically be neglected in an artery of this size (Lighthill 1975; Zamir 2000).

The Womersley number α is a dimensionless parameter that arises in the analysis of fully developed pulsatile flow (Womersley 1955). It quantifies the relationship between unsteady forces, measured by the angular frequency ω , and viscous forces, measured by the kinematic viscosity (Equation (5)) (Ku 1997).

$$\alpha = R \sqrt{\frac{\omega}{\nu}} \quad (5)$$

Table 1: Summary of bioreactor and physiological flow loop literature.

Work	Vessel geometry	Flow parameters	Biological Tissue	Velocity measurements	Focus
(Conklin, Surowiec et al. 2000)	Artery cannulated onto thin-walled stainless steel tubing	Canine artery waveforms ~170 mL/min	Excised arteries	None	Cell viability under simulated physiological perfusion
(Levesque, Nerem et al. 1990)	Cells on glass plate	5-90 dyn/cm ² reported shear stress	Endothelial cells	None	Cell proliferation under steady state vs. sinusoidal laminar flow
(Mironov, Kasyanov et al. 2003)	Artery cannulated onto stainless steel tubing	Not stated	Excised arteries	None	Cell proliferation under pulsatile perfusion with stretch
(Yazdani and Berry 2009)	Artery sutured onto custom fitting (see 2.2.1)	Not stated	Excised arteries	None	Cell proliferation within stents under pulsatile flow
(Yazdani, Tillman et al. 2010)	Artery sutured onto custom fitting (see 2.2.1)	1.7-13.2 dyn/cm ² reported shear stress	Endothelial cells on decellularized arterial segments	None	Cell response to varying levels of steady and pulsatile shear
(Tanne, Bertrand et al. 2008)	Model of left atrium and left ventricle	Not stated	None	2-component 3D time-resolved PIV	Flow dynamics measurements in left heart model
(Burgmann, Grosse et al. 2009)	Elastomer vessel connected smoothly to rigid pipe	Peak $Re \sim 1000-1750$ $\alpha \sim 5-7.5$	none	2-component 2D time-resolved PIV	Pulsatile flow measurements in elastic vessels
(Rossi and Ekeberg 2006)	Cells on glass plate in square microchannel	6 dyn/cm ²	Endothelial cells	2-component 2D μ PIV	Shear stress measurement over endothelial cells
Present work	Vessel connected to custom fitting	Average $Re \sim 150-300$ $\alpha \sim 6.4-9.0$	Endothelial cells	2-component 2D time-resolved PIV	Flow dynamics measurements in arterial model with endothelial cells

Typical values for the Womersley number in medium arteries are between 1 and 10 (McDonald 1974; Fung 1997). In this work, the flows studied were those typical for the resting and active state of a healthy human. For the resting state, $Re \sim 150$ and $\alpha \sim 6.4$ were used, and the active state was modeled using $Re \sim 300$ and $\alpha \sim 9.0$. These values are comparable to those used by Yazdani and Moore et al. (2004). Measurements were also performed for $Re \sim 150$ quasi-steady flows as a baseline flow for comparison with the pulsatile $Re \sim 150$ flow.

The target maximum and minimum pulse pressures were determined to be 120 mmHg and 80 mmHg, respectively. These values correspond to the systolic and diastolic blood pressures found in healthy humans and are those typically used for arterial flow modeling (Yazdani, Moore et al. 2004; Yazdani and Berry 2009). The other relevant parameter of the pressure wave is the mean arterial pressure (MAP), which characterizes the shape of the pressure waveform. For a human at rest, the MAP can be estimated as ~ 93 mmHg using Equation (6).

$$MAP = P_{dias} + \frac{1}{3}(P_{sys} - P_{dias}) \quad (6)$$

For higher activity levels and faster heart rates, the shape of the wave changes so that the MAP is more nearly the arithmetic mean of the systolic and diastolic pressure, and is approximately 100 mmHg.

The bioreactor designed in this work provides flow parameters with the ranges and values described above, and sustains the growth of human microvascular endothelial cells (HMECs) on the inner surface of the vessel section. It has been designed for ease of assembly and sterilization and a minimum number and cost of replacement components. The flow waveforms produced are not identical to physiological conditions; however, the purpose of this bioreactor flow loop is not to duplicate physiological conditions but to approximate them nearly enough within the bioreactor that significant correlations between flow parameters and physiological response can be measured. The following sections describe in detail the design of the bioreactor flow loop and the characterization of its flow capabilities.

2.2 System Design

The three main sections of the bioreactor flow loop are the bioreactor itself, the flow components, and the instrumentation. The primary considerations applied to the design, as discussed earlier, were accurate reproduction of physiological flow, compatibility with a standard PIV system, compatibility with a biological environment, and total cost of the system. Additionally, because of the sterility requirements of tissue engineering, ease of use within a laminar flow hood was also an important aspect of the design. Finally, the entire system had to be small enough to fit within a laboratory incubator. Each of the following sections describes the design of the components of the bioreactor flow loop and provides technical details.

2.2.1 Bioreactor

The bioreactor in the flow loop is designed closely after the bioreactor used for stent analyses by Yazdani and Berry et al. at Wake Forest University (2009), a group that generously provided a sample bioreactor for this work (Figure 3). Their bioreactor consists of a vessel section within an outer cover, both attached at the ends to customized fittings. These fittings are then connected via silicone tubing to three-way valves with medical luer valve ports for addition and removal of material using syringes. The entire system is seated on a pair of stainless steel rods for attachment to a mandrel. Several significant modifications were made to the Wake Forest design to create the new functionality required for the bioreactor flow loop.

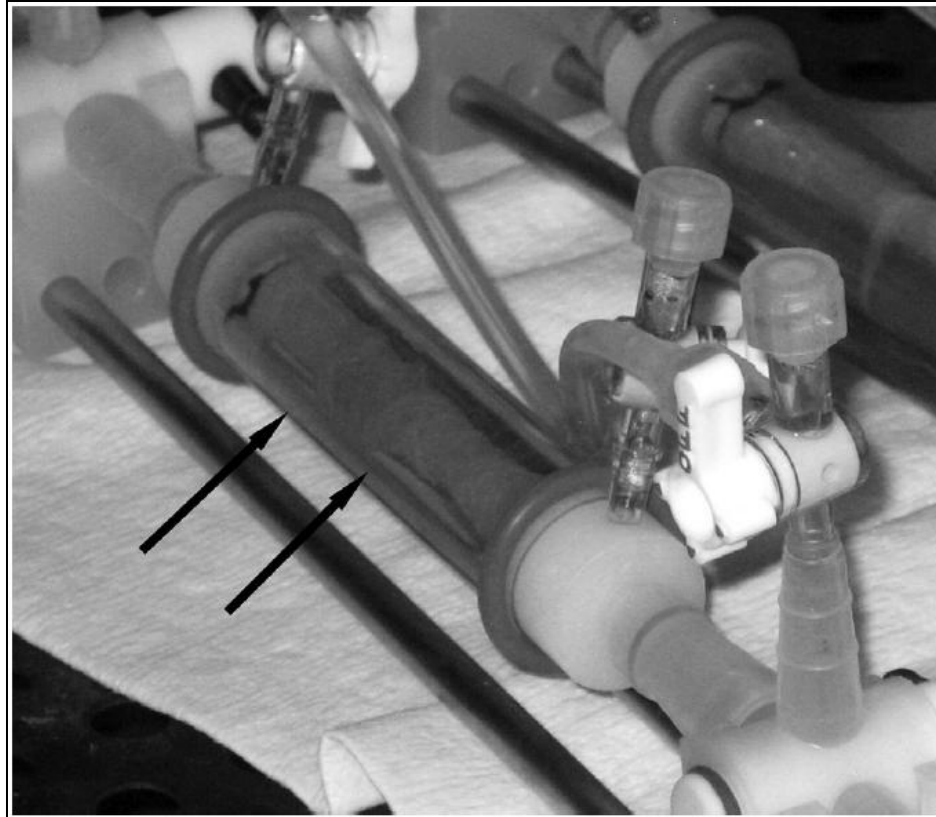


Figure 3: Wake Forest bioreactor. (Yazdani and Berry 2009) (with permission)
(Arrows indicate stent location within artery.)

First, because the bioreactor flow loop is used with PIV to measure flow profiles, transparency of the bioreactor is vital. PIV requires undistorted optical access to the area of interest for both an excitation laser and an imaging system (the PIV method will be discussed in more detail in Chapter 3). In this case, optical access requires a transparent vessel and matched refractive indices (RIs) across non-planar surfaces to eliminate distortion due to refraction. While the Wake Forest bioreactor was originally designed for use with *ex vivo* porcine arteries, the opacity of arteries precludes their use in a system with conventional PIV. To achieve transparency, the arteries were replaced with transparent artificial vessels with a cultured layer of endothelial cells on the inner surface.

Traditionally, matching the index of refraction of the test section (vessel) with the index of refraction of the fluid has been a challenge in PIV experimentation. Most PIV experiments to date have used elastomers and polymers with RI of the test section considerably higher than that of water (Yazdani, Moore et al. 2004; Gray, Owen et al. 2007; Tanne, Bertrand et al. 2008;

Burgmann, Grosse et al. 2009; Charonko, Karri et al. 2009). To match the RI of the fluid to that of the polymer, glycerine is typically mixed with water and used as the test fluid (Table 2). This increases the density of the fluid and the complexity of the system.

Table 2: Comparison of vessel materials and fluids used in PIV experiments.

Work	Vessel material	Vessel material RI	Fluid (percents by weight)	Fluid RI
Yazdani, Moore et al. (2004)	Sylgard 184 elastomer	1.42	50% glycerine, 50% water	1.4
Gray, Owen et al. (2007)	Borosilicate glass	1.473	Pure glycerine	1.473
Tanne, Bertrand et al. (2008)	Silopren LSR 2050 elastomer	1.42	40% glycerine + 60% water	1.38
Charonko, Karri et al. (2009)	Sylgard 184 elastomer	1.42	40% glycerine + 60% water	1.39
Burgmann, Grosse et al. (2009)	PDMS elastomer	1.406	60.7% glycerine + 39.3% water	1.406
			40% glycerine + 60% water + NaI	1.4
Present work	FEP copolymer	1.34	Pure water	1.33

In this thesis, the copolymer FEP (fluorinated ethylene propylene) was used, which has an RI nearly matching that of water. In the PIV literature, no previous work could be found that used FEP or any other material with an RI similar to that of water. FEP is typically used as a heat-shrink material for electrical applications and seems to be unknown in the PIV community. Although it seems to be only a minor feature of this design, the identification of FEP as a material with favorable optical properties for PIV and compatibility with a cellular layer is a large step towards simplification of PIV experiments for a wide range of biological applications. Table 3 lists properties of FEP that are relevant to PIV and bioreactor applications.

Table 3: Properties of FEP.

Property	Value
Refractive Index	1.34
Density	2.15 g/cm ³
Elastic Modulus	0.34 GPa
UV resistance	good
EtO resistance	good

To eliminate refraction between the vessel and its surroundings, the bioreactor was placed into a water bath in a refraction box made of transparent acrylic sheets. This eliminates RI variation at the surfaces of the vessel. Because the walls of the box are planar, no distortion occurs at the RI interface between the water bath and the acrylic walls or between the walls and the PIV optics. Furthermore, the water bath provides thermal stability of the bioreactor, an important feature for tissue culturing. The bioreactor flow loop passes directly through the walls of the refraction box, using a press fit of the silicone tubing through holes in the sides of the box to maintain isolation of the flow from its surroundings yet allow the water bath to cover the bioreactor.

Another functional modification that was made to the bioreactor was the addition of location and magnification measuring capability. Because the Wake Forest bioreactor was modified to use nonporous FEP vessels instead of porous porcine arteries, the exterior tubing around the vessel became unnecessary. This allowed slots to be added to the vessel fittings so that a ruler with 0.5 mm resolution fits alongside the vessel. The ruler is used with the PIV imaging system to identify the longitudinal location of the measurements and to calculate the magnification of the system. Figure 4 is a photograph of the redesigned bioreactor with FEP vessel (without localization/magnification scale present) in the acrylic box. In the figure, cell growth media present in the bioreactor produces the light pink color visible in the FEP vessel. The blue disks in the luer valves are air filters for the cell incubation stage of the experiment.

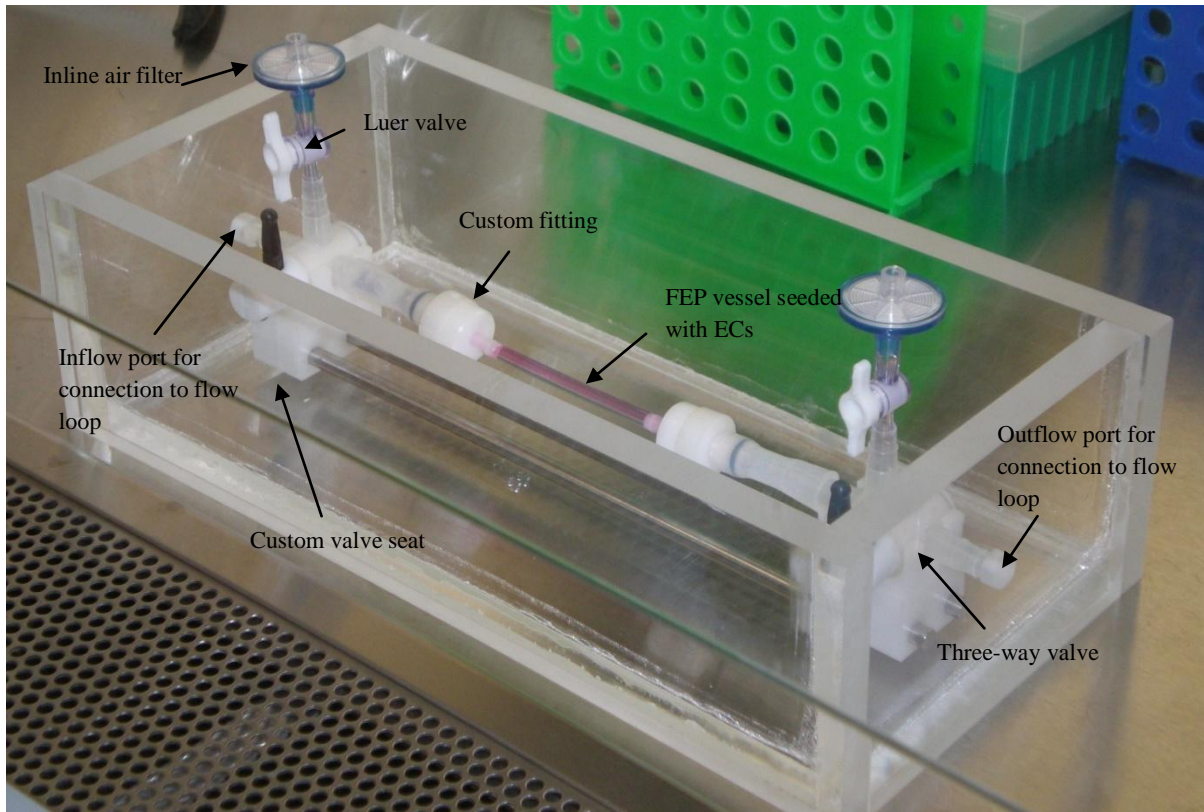


Figure 4: Bioreactor in refraction box.

2.2.2 Flow Components

The flow loop was designed as a hybrid of existing PIV-compatible non-biological flow loops and non-PIV compatible bioreactor flow loops (Conklin, Surowiec et al. 2000; Mironov, Kasyanov et al. 2003; Charonko, Karri et al. 2009; Yazdani and Berry 2009; Yazdani, Tillman et al. 2010). The key components of the flow loop are a peristaltic pump, pressurized reservoir, pulse dampener, pinch valve, and connecting tubing. A wye with luer connection is also included in the loop to allow easy, sterile injection of fluids and/or particles to the loop using a syringe. The connecting tubing has 3/16" inside diameter (ID) (Tygon 3350 Silicone, Cole-Parmer). All components in contact with the working fluid are sterilized with ethylene oxide (EtO).

The flow loop was designed using a 10-600 RPM peristaltic pump (MasterFlex L/S 7550-30 Pump Drive, Cole-Parmer) because of the sterility requirement. A standard gear pump, such as that used by (Charonko, Karri et al. 2009), permits more control over the flow profile but requires contact between the pump and the working fluid. The peristaltic pump allows complete

isolation of the fluid within the pump tubing from the pump head (MasterFlex L/S Easy-Load II Pump Head, Cole-Parmer). Because of the slow response of the pump to an external signal, it is run at a constant voltage and the pulsation in the flow is generated by the intermittent action of the four rollers within the pump head. This restricts the pressure and flow waveforms that can be generated; however, the shape of each cycle is a good approximation to the physiological cardiac cycle. The pump head accepts tubing with ID from 1/16” to 3/8” (1.6 mm to 9.5 mm). For each tubing diameter, a linear relationship exists between the Reynolds number and Womersley number of the flow within the vessel, as the pump frequency and flow rate are linearly dependent. The range of Reynolds and Womersley numbers that can be obtained with the pump tubing available is listed in Table 4. The L/S 15 tubing was selected because the correlation between Reynolds and Womersley number allows a close approximation to physiological flow to be generated.

Table 4: Range of Reynolds and Womersley numbers attainable with available equipment.

Vessel diameter: 4.57 mm. Fluid: water ($\nu = 1 \times 10^{-6} \text{ m}^2/\text{s}$)

Tubing Size	Tubing ID (in)	Range of flow rates (mL/min)	Range of Re	Range of α
L/S 13	1/16	0.6-36	3-170	3.7-29
L/S 14	1/16	2.1-130	10-600	3.7-29
L/S 16	1/8	8.0-480	40-2200	3.7-29
L/S 15 & L/S 25	3/16	17-1000	80-4600	3.7-29
L/S 17	1/4	28-1700	130-7900	3.7-29
L/S 18 & L/S 36	3/8	38-2300	180-11000	3.7-29

The pressure reservoir is primarily used to achieve physiological pressure levels and was custom-designed for the bioreactor flow loop. It is composed of a transparent cylindrical chamber, sealed at the ends with rubber gaskets to flat plates, with flow inlet and outlet fittings on the bottom plate and an air inlet port in the top plate. The air inlet fitting is equipped with a pressure gauge, a back-pressure relief valve to allow manual control of the static pressure in the chamber and a 0.3 μm in-line filter (Whatman HEPA-Vent, Fisher Scientific) to prevent contamination of the flow loop from the air supply. Figure 5 is a photograph of the pressure reservoir assembly with the air inlet and flow fittings. The pressure reservoir serves not only to maintain the static pressure of the flow loop, but also as a reservoir for cell growth media for

extended use of the flow loop with a cell layer in the bioreactor. It was designed for complete disassembly for cleaning and sterilization with EtO.

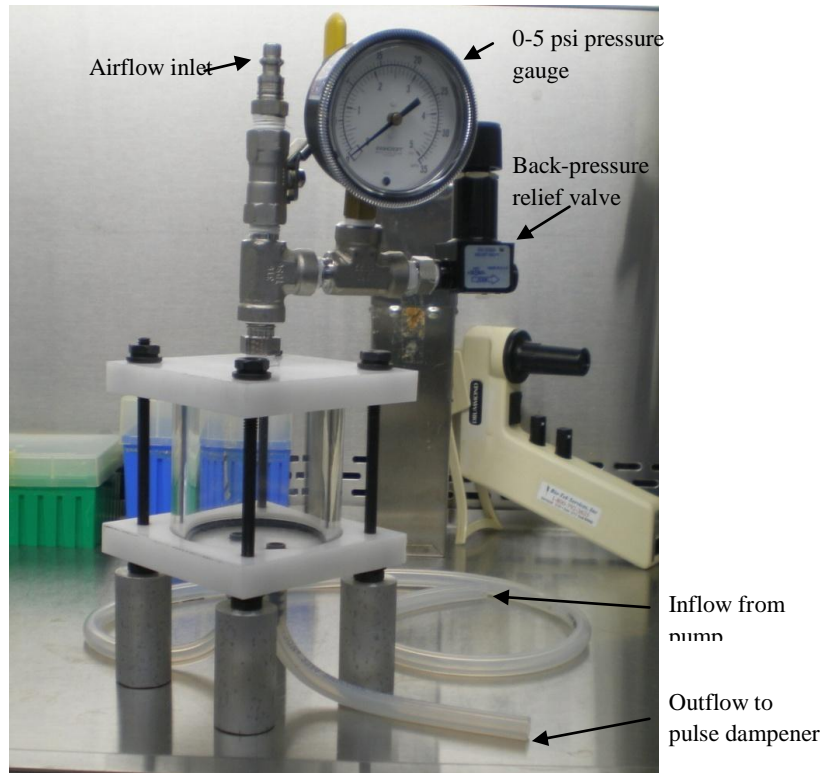


Figure 5: Pressure reservoir.

The pulse dampener (MasterFlex L/S Pulse Dampener, Cole-Parmer) is a hemispherical chamber used to eliminate high frequency pressure waves in the system (Figure 6). The dampening effect is controlled by the fill level of the hemisphere. The optimum fill level to reduce noise in the bioreactor flow loop was determined empirically to be within a few milliliters of the total 170 mL volume, with the remaining volume filled with air.



Figure 6: Pulse dampener.

The pinch valve (Delrin Flow Control Pinch Valve, SmallParts) is used to control the amplitude of the pressure wave, or pulse pressure, of the system. It is analogous to a potentiometer in an electrical circuit, varying the total resistance of the loop. The pulse pressure is manually changed by adjusting the position of the valve. A vernier scale printed on the valve allows the position and resulting resistance to be recorded and reproduced.

The bioreactor flow loop is small enough for all components including the pump to fit within a standard laboratory incubator for experiments requiring constantly monitored flow through the bioreactor. Two people can easily transport the assembled flow loop. Any components not sterilized with EtO (such as the pump and the wiring) can be cleaned with ethanol spray. Figure 7 is a photograph of the bioreactor flow loop (under the laminar flow hood), showing the layout of the components when fully assembled.

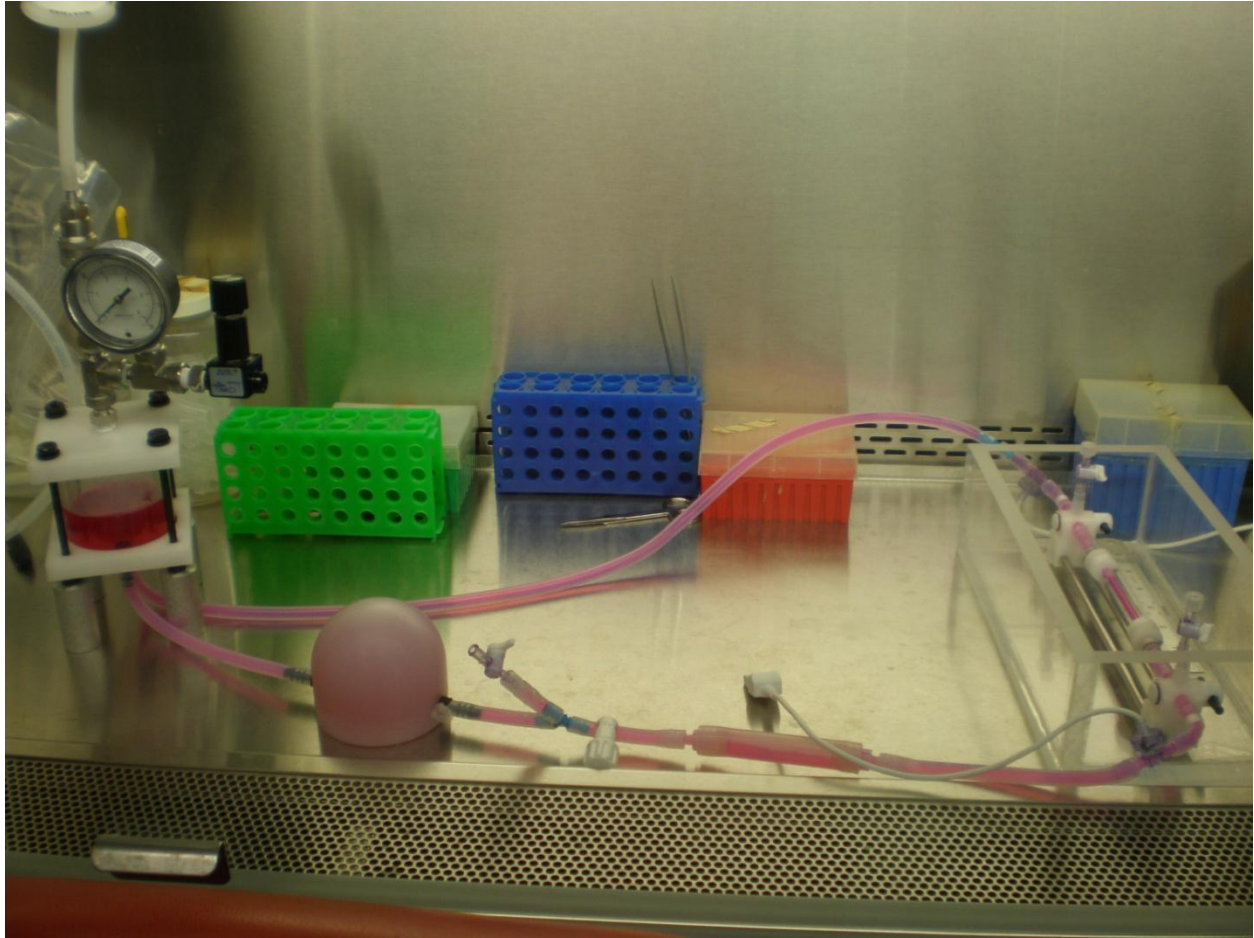


Figure 7: Bioreactor flow loop.

2.2.3 Instrumentation

The instrumentation for the bioreactor flow loop comprises the physical pressure and flow sensors and the control panel. The in-line pressure sensors located before and after the bioreactor (Single Use Pressure Sensors, PendoTECH) have accuracy within 2% in the physiological pressure range, are autoclavable, and can alternatively be sterilized with EtO. The volumetric flow rate was measured with an ultrasonic flowmeter (HQ11XL, Transonic Systems) with 10% accuracy. The flowmeter exhibits significant drift when measurements are taken over a period of more than several minutes, which, combined with the high measurement uncertainty, makes flowmeter data usable only for verification of the pump set speed.

The bioreactor flow loop is controlled with a 16 bit, 250 kHz data acquisition (DAQ) board (USB-6229 BNC, National Instruments) and a customized LabVIEW virtual instrumentation

panel (VI) (Figure 8). The VI controls the pump through the DAQ, which is connected to the pump by a custom-wired DB-15 connector. A user-defined set flow rate is converted in the VI to the corresponding voltage for the selected tubing size. The pressure sensors are powered by the DAQ board and the output signals amplified with a gain of 1000 by custom wiring to a battery-powered PCB amplifier. The amplified signals are read by the DAQ and converted within the VI to pressure units. Similarly, the average and instantaneous flow rates measured by the flowmeter are read as voltage signals by the DAQ and converted to volumetric flow units within the VI. Both the pressure and the flow readings exhibit intrinsic linear offsets. The VI subtracts these offsets from each signal for more accurate measurements. When other parameters of the flow loop such as vessel diameter and fluid properties are entered in the VI front panel, parameters such as Reynolds and Womersley number are calculated in real-time. The VI also performs analyses of the linear average of the signals from the two pressure sensors to report the systolic and diastolic pressures as well as the MAP, making it simple to tune the system to achieve the appropriate pressure waveform. The VI also graphs the sensor data in real-time. Finally, the current data set can be saved to an Excel file.

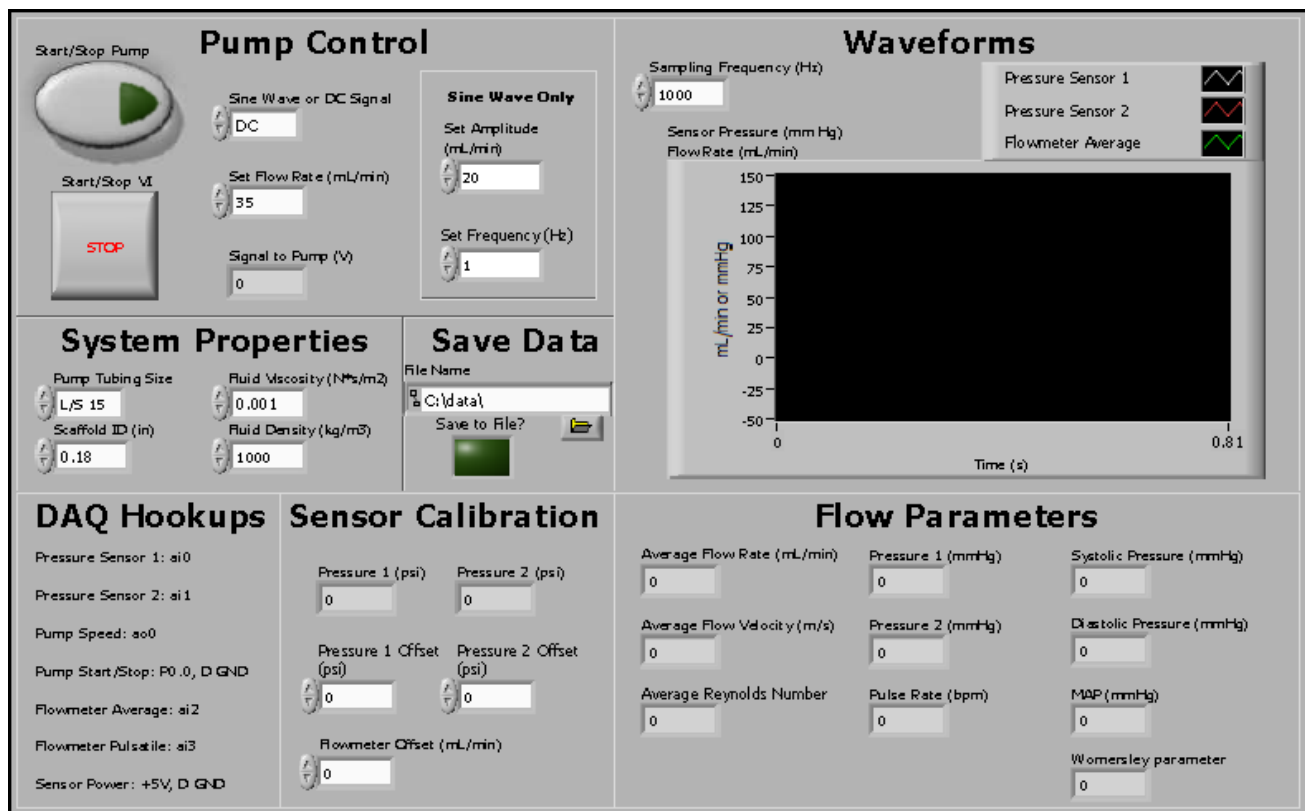


Figure 8: LabVIEW VI front panel.

2.3 Global Flow Parameters

To characterize the bioreactor flow loop control system, the sensor data monitored by the LabVIEW VI was recorded. Sample pressure and flow waveforms (flow nondimensionalized to Reynolds number) are shown in Figure 9 for the middle of the cell-free vessel for each of the three flows of interest, with the corresponding experimental parameters listed in Table 5. The pressure waveforms for all PIV measurements (described in Chapter 3), along with detailed experimental parameters, can be found in Appendix A: Additional Pressure .

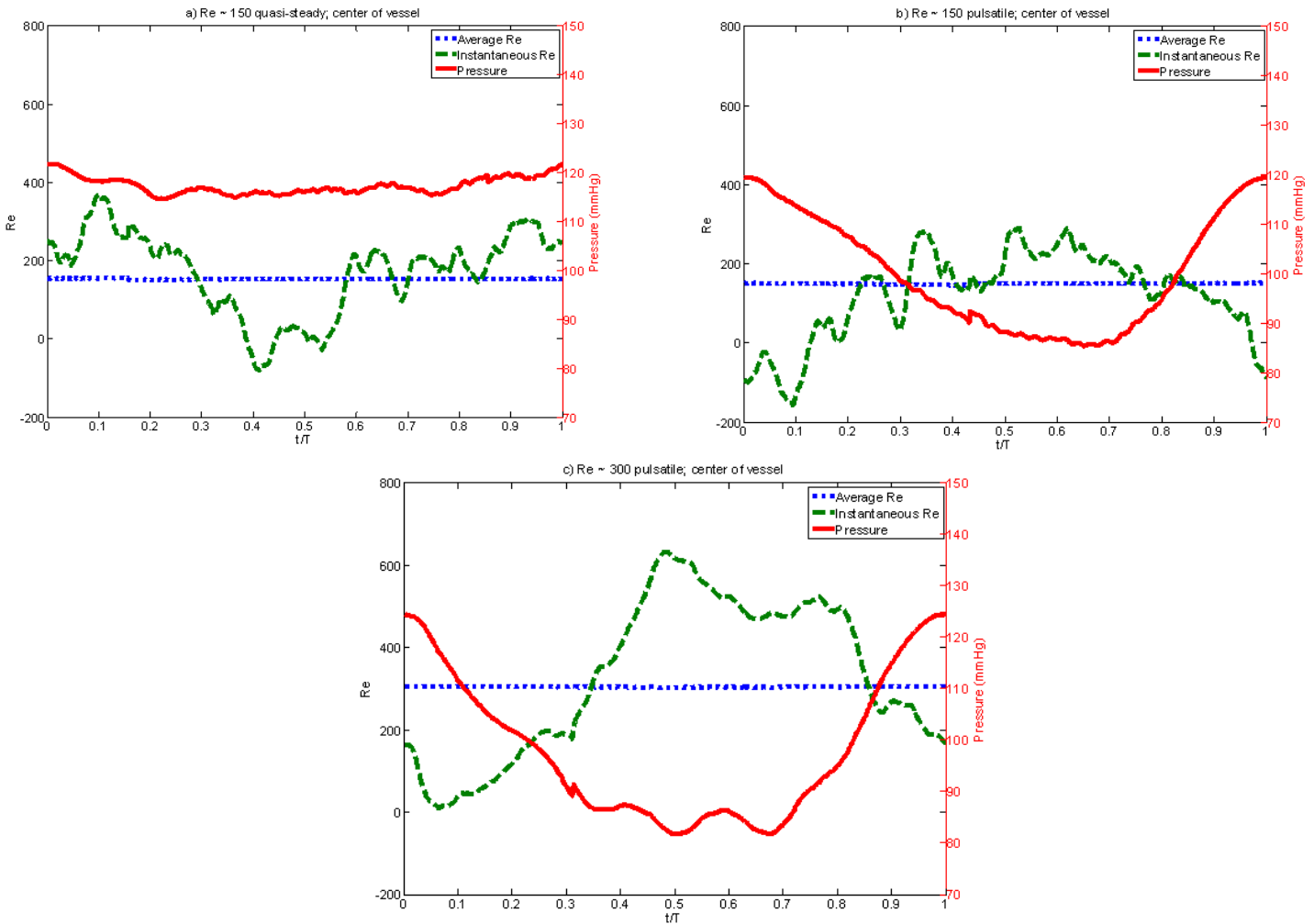


Figure 9: Pressure and flow for center of vessel with no cells present.

a) $Re \sim 150$ quasi-steady. b) $Re \sim 150$ pulsatile. c) $Re \sim 300$ pulsatile. Time nondimensionalized with cycle period T_w . The period of b) $Re \sim 150$ pulsatile is used to nondimensionalize a) $Re \sim 150$ quasi-steady.

Table 5: Experimental parameters for waveforms in Figure 9.

Figure	Test Description	Set flow rate (mL/min)	Resistor position	Re	α	Diastolic Pressure (mmHg)	Systolic Pressure (mmHg)	MAP (mmHg)
a	quasi-steady, vessel center	35	Open	150	-	(114)	(122)	117
b	pulsatile, vessel center	35	3.85	150	6.4	86	119	100
c	pulsatile, vessel center	70	4.0	304	9.0	81	124	98

Although the average flow rate is constant (dependent only on the voltage signal to the pump), the ultrasonic flowmeter exhibits drift during the duration of a PIV measurement. This makes the flowmeter reading unreliable for more than approximate estimation of the Reynolds number. The pressure waveform is constant over time and can be easily reproduced using the same control parameters.

2.4 Summary

The bioreactor flow loop described in this chapter can be used for novel PIV measurements of flows within a controlled biological environment. Improvements on the design of existing bioreactor flow loops include a digital interface for flow and pressure control and monitoring, as well as compatibility with a standard PIV system. This bioreactor flow loop is capable of generating the physiological flows found in a medium-sized human artery for a subject at rest and exercising. This system can be used in the study of vascular transport for a broad range of experiments.

3 Particle Image Velocimetry of an Arterial Flow Bioreactor

3.1 Introduction

PIV is a technique for non-invasively measuring velocity flow fields used for a diverse range of experimental fluid mechanics applications because of its high resolution and accuracy. In a typical PIV measurement, a pulsed laser sheet illuminates a plane in the flow of interest. This illuminates tracer particles seeded throughout the flow which are imaged by a high-speed camera. The camera records one image for each laser pulse and a cross-correlation algorithm is used to calculate the statistical particle displacement between images. Because the time between pulses is known, the velocity field can be computed from the particle displacements. Further background on basic PIV techniques and applications can be found in (Adrian 1991; Westerweel 1997; Adrian 2005; Raffel 2007).

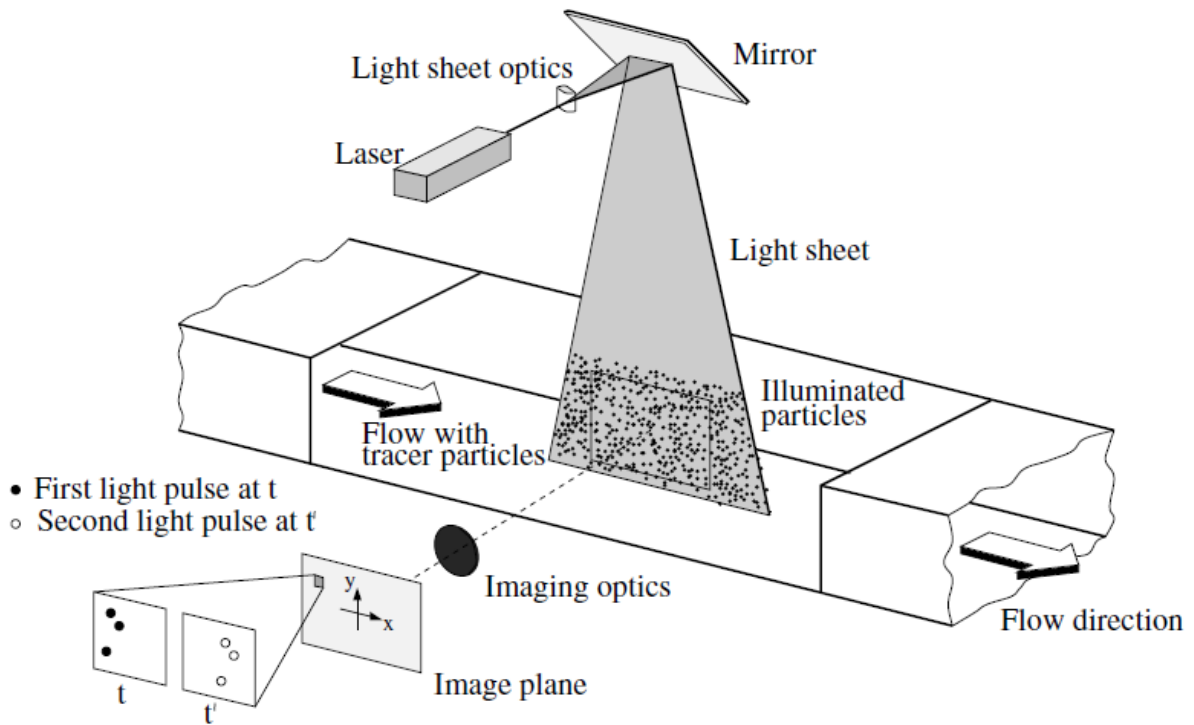


Figure 10: Diagram of basic PIV experiment. (Raffel 2007)
With kind permission of Springer Science + Business Media.

PIV offers several advantages over other experimental fluid measurement techniques. The primary advantage is that the velocity distribution across an entire cross-section of a flow field

can be measured simultaneously and with high spatial and temporal resolution. Additionally, it is a non-invasive technique, making it particularly attractive for biological applications. However, to implement this technique, special considerations must be made. As mentioned in Chapter 2, PIV is an optical measurement technique and requires transparency of the flow and vessel. Additionally, the high level of alignment necessary for accurate measurements requires a stationary imaging area.

Because of these challenges, there has not yet been great success in the application of PIV techniques to biological flows. PIV has been performed for simulated physiological flows but in non-biological environments. Examples include measurements of shear stresses near stents (Yazdani, Moore et al. 2004; Charonko, Karri et al. 2009), velocity field measurements in cardiac and pulmonary valve models (Marassi, Castellini et al. 2004; Pierrakos, Vlachos et al. 2004; Tanne, Bertrand et al. 2008), and low-resolution velocity field measurements in compliant vessel models (Burgmann, Grosse et al. 2009). Although important towards understanding the flow fundamentals, none of these experiments have incorporated biological tissue in the model and consequently do not incorporate effects caused by the interaction of tissue with the flow.

PIV experiments have also been carried out for *in vitro* and *in vivo* flows. Most *in vitro* experiments have been studies of blood flow in a laboratory setting (Bitsch and Olesen 2003; Park, Kim et al. 2004; Bitsch, Olesen et al. 2005; Rossi and Ekeberg 2006; Hirono, Arimoto et al. 2008). Only with sample thicknesses on the order of a millimeter or less is blood transparent enough for PIV measurements. Because of this, these experiments were performed in square glass microchannels using microscopic PIV (μ PIV), a variant of standard PIV. Although high resolution can be achieved for such experiments, the unrealistic geometry limits the applicability of the results. Additionally, because of the short working distance of microscope objectives used in μ PIV, only studies of capillary flow can be performed using such techniques.

Some groups (Lee and Kim 2005; Fouras, Dusting et al. 2007) have performed PIV of blood flow in opaque vessels using x-ray PIV, which uses a synchrotron radiation source instead of a laser sheet. Because using x-rays eliminates optical issues, these groups have been able to perform measurements in cylindrical vessels. Due to the restrictions of synchrotron sources, however, these measurements are only for microscopic flows at low Reynolds numbers.

PIV measurement of *in vivo* flow has the same optical restrictions as *in vitro* flow, with the added challenge of imaging through tissue. *In vivo* PIV measurements have been performed in chick embryos (Poelma, Vennemann et al. 2008) and rat mesentery arterioles (Sugii, Nishio et al. 2002), both locations in which the layer of tissue covering the vessel and the vessel wall itself are thin enough to allow optical access. Such techniques cannot be applied to thicker, larger vessels.

The PIV experiments described here were performed in the bioreactor flow loop system described in detail Chapter 2. For the first time, the whole cross-sectional velocity field has been directly measured in an *in vitro* system that combines a biological environment with arterial flow and geometry. These experiments compare the velocity and wall shear stress in a vessel with and without the presence of an endothelial cell layer. The measurements were performed for the three flow cases described in Chapter 2 and at three locations along the length of the vessel, obtaining velocity fields for 55% of the total length.

3.2 Experimental Methods

3.2.1 Endothelial Layer

This section describes the methods used to obtain and sustain the endothelial layer on the FEP vessel for the PIV measurements with human microvascular endothelial cells (HMEC). The first step was to confirm the viability of endothelial cells on FEP. Endothelial cells (ECs), like most eukaryotic cells, die in suspension and proliferate only if adhered to a surface. *In vivo*, they grow in a monolayer on an extracellular matrix that exhibits high porosity and an irregular surface. The FEP tubing used for these experiments is a nonporous hydrophobic polymer. To enhance the binding of ECs to the FEP surface, the FEP was first soaked in fibronectin, a glycoprotein found in the extracellular matrix that reduces the hydrophobicity of the FEP, promoting cellular adhesion and growth.

To test FEP for cell viability, tests were first performed using flat sheets (1/32" thick) of FEP. Two (2 cm x 2 cm) square sheets were sterilized by EtO (12 hour cycle with >24 hour diffusion time) before beginning the trial. The sheets were placed in a tissue-culture treated polystyrene 6-well plate (Fisher) and were treated with 33% fibronectin (fibronectin from bovine plasma, Sigma-Aldrich) in HMEC growth media (MCDB131, MediaTech, supplemented with 10% Fetal

Bovine Serum (FBS), Sigma-Aldrich; 1% antibiotic/antimycotic, MediaTech; 10 mM L-glutamine, Fischer; 1 µg/mL hydrocortisone, Sigma-Aldrich; 10 ng/mL epidermal growth factor, Sigma-Aldrich) for 90 minutes. The fibronectin was aspirated and each sheet was seeded with 40,000 cells (HMEC-1, CDC Atlanta) suspended in 0.2 mL HMEC growth media. The plate was placed in an incubator at 37C and removed after four days for viability staining.

DAPI and phalloidin immunocytochemical stains were used for all staining in this thesis. DAPI is a blue fluorescent stain that binds to nucleic acid, allowing imaging of cell nuclei. The phalloidin stain binds a green fluorescent phalloidin to F-actin, a filamentous protein found in cell membranes. These stains, when combined, allow the location and structure of the cells to be imaged with a standard fluorescence microscope. The staining protocol involves first fixing the cells with paraformaldehyde and permeabilizing the membrane with Triton X-100 (a surfactant). Non-specific binding is prevented by treatment with bovine serum albumin (BSA). The cells are treated with the phalloidin (Oregon Green, Invitrogen) and DAPI (VectaShield with DAPI, Vector Laboratories) stains and imaged with the fluorescence microscope.

Figure 11 is a microscope image that overlays the two fluorescent stains on one of the FEP sheets. The DAPI nucleus stain is shown in blue and the phalloidin membrane stain in green. From this image, it can be seen that a fully confluent layer of ECs can be grown on FEP.

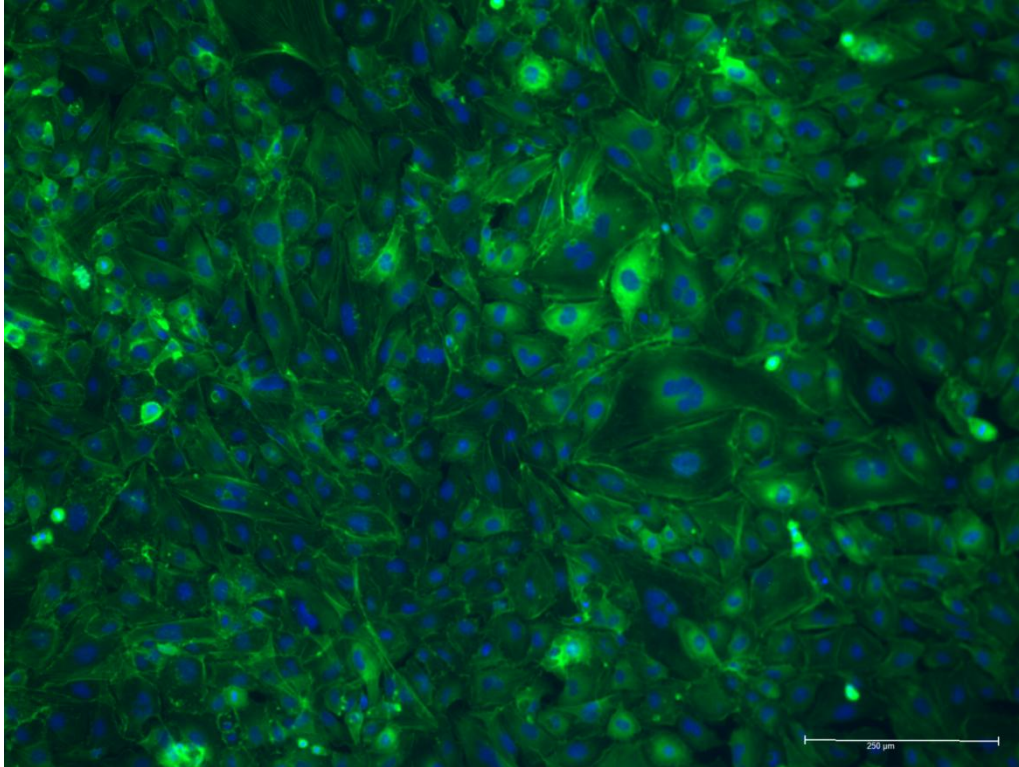


Figure 11: HMEC-1 on FEP sheet.

DAPI stain in blue; phalloidin stain in green; 10x microscope objective.

After verification that FEP supports the growth of ECs, cell layers were grown in bioreactors. Although the area for gas exchange is much lower in the FEP vessel than for the FEP sheets, sufficient oxygen and carbon dioxide were able to reach the cells. A challenge inherent to seeding the inner surface of a cylinder is even distribution of cells on the surface. To achieve well-distributed seeding, one to two bioreactors can be attached longitudinally to the shaft of a low-speed motor, with the vessel parallel to the motor shaft. An aluminum cylinder, machined with flat surfaces to facilitate binding to the shaft, is added to balance the load. Running the motor rotates the bioreactor, allowing the cells to settle out of solution evenly onto the surface of the vessel.

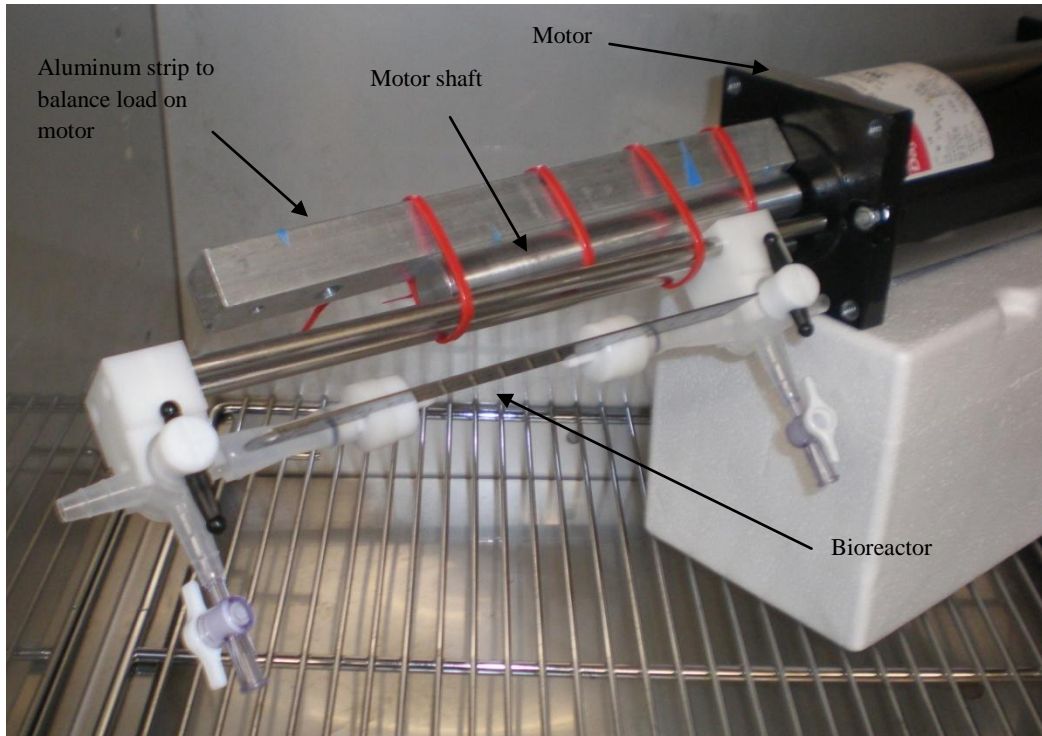


Figure 12: Bioreactor on motor shaft.

To develop the EC layer for the PIV measurements, the following protocol was followed. Components for two bioreactors and the bioreactor flow loop were sterilized using EtO (12 hour cycle with >24 hour diffusion time). The two bioreactors were assembled under a laminar flow hood with 8 cm FEP vessels (6 cm flow length with 1 cm fitting overlap on each side). For steady-state Poiseuille flow, the development length for a vessel of this diameter is 4.1 cm, so it was expected that this length would allow fully developed flow to be reached. The vessels were treated with 33% fibronectin in HMEC growth media for 30 minutes. The fibronectin was aspirated and each vessel was seeded with 400,000 HMECs suspended in 2 mL HMEC growth media. Sterilizing air filters (0.22 μ m pore size syringe filters, Fisherbrand) were attached to the luer valves of each bioreactor. The two bioreactors were fixed to the motor shaft and rotated at approximately 0.5 Hz for 6 hours at 37C, after which they were removed from the motor and placed into an incubator. At the same time, two new FEP sheets were seeded and incubated using the protocol described previously.

An alamarBlue assay was performed twice during the cell incubation period to determine cell proliferation. This assay consists of an oxidation-reduction (REDOX) indicator that yields a

colorimetric change and a fluorescent signal in response to metabolic activity. Therefore, metabolic activity of cells, corresponding to proliferation and viability, can be determined by measuring a colorimetric change in the alamarBlue reagent. Spectrophotometry can be used to compute the percent reduction and, qualitatively, the proliferation of cells. A 10% solution of alamarBlue reagent in HMEC growth media (alamarBlue, Invitrogen) was placed into each vessel and onto the FEP sheets and incubated for 2 hours. The alamarBlue was removed for spectrophotometry and fresh HMEC added to each vessel for further incubation. Table 6 provides the percent reduction of alamarBlue of each case with respect to a cell-free control. The assay was performed after two and three days of incubation (on day 3 and day 4), and three fluid samples were measured in the spectrophotometer for each case.

Table 6: alamarBlue assay results.

Test Sample	Assay 1: Day 3		Assay 2: Day 4	
	alamarBlue reduction (%)	Standard deviation (N=3)	alamarBlue reduction (%)	Standard deviation (N=3)
Bioreactor I	28.3	1.2	25.9	0.5
Bioreactor II	27.5	1.7	27.0	0.5
FEP sheets	20.5	1.9	17.3	1.5

Because of the different seeding density and surface area of the bioreactors and the sheets, a quantitative comparison of the alamarBlue reduction is not feasible. However, the data show that both the bioreactors and the sheets had proliferating cells. The decrease in alamarBlue reduction from day 3 to day 4 corresponds to a decrease in proliferation rate, indicating that the cell layer was nearing confluence.

After three days of incubation (following the second alamarBlue stain), one bioreactor (I) was stained for imaging of the cell layer using the DAPI and phalloidin staining protocol described previously. It had a healthy, nearly confluent layer of cells on the FEP (Figure 13). These results, combined with the alamarBlue results, indicated that the cell layer in the second bioreactor (II) was similarly viable and could be used for meaningful measurements. Bioreactor II was connected to the remaining flow loop components and refraction box for PIV measurements. 14 drops of microspheres for PIV (described in section 3.2.2) were added to 400

mL of cell media (MCDB131, MediaTech) and the solution was autoclaved to sterilize. The solution was sonicated for 5 minutes to disperse the particles, warmed to 37C, and added to the bioreactor flow loop. The bioreactor flow loop remained at room temperature (20C) for PIV measurements. The refractive box was filled with sterile water initially at 37C that cooled to ambient temperature over the duration of the measurements. After the PIV measurements, the bioreactor flow loop was returned to the laminar flow hood for removal and staining of bioreactor II. The total time that bioreactor II spent outside the incubator between filling of the flow loop and staining was 2.5 hours.

Figure 13 shows the cell layer on each of the bioreactors. Because of the curvature of the vessels, only part of each image is in focus. It can be clearly seen that the cell layer in both bioreactors was viable and nearly confluent at the time of staining. The microspheres used for PIV imaging adhered to the endothelial layer and can be clearly seen in the second image, as they fluoresce at nearly the same wavelength as the phalloidin stain. Because of the relative brightness of the microspheres, the microscope settings were not identical for both images, causing the cell membranes in the bottom image to be dimmer than in the top image. This figure shows that the cell structure was not affected by the PIV measurements.

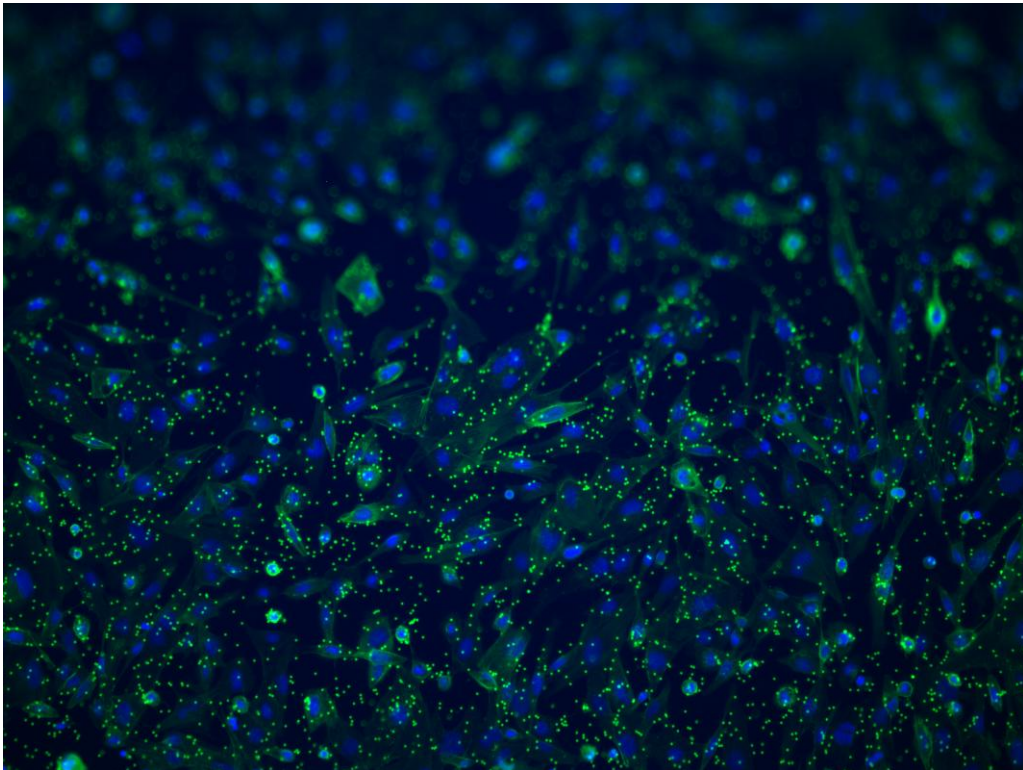
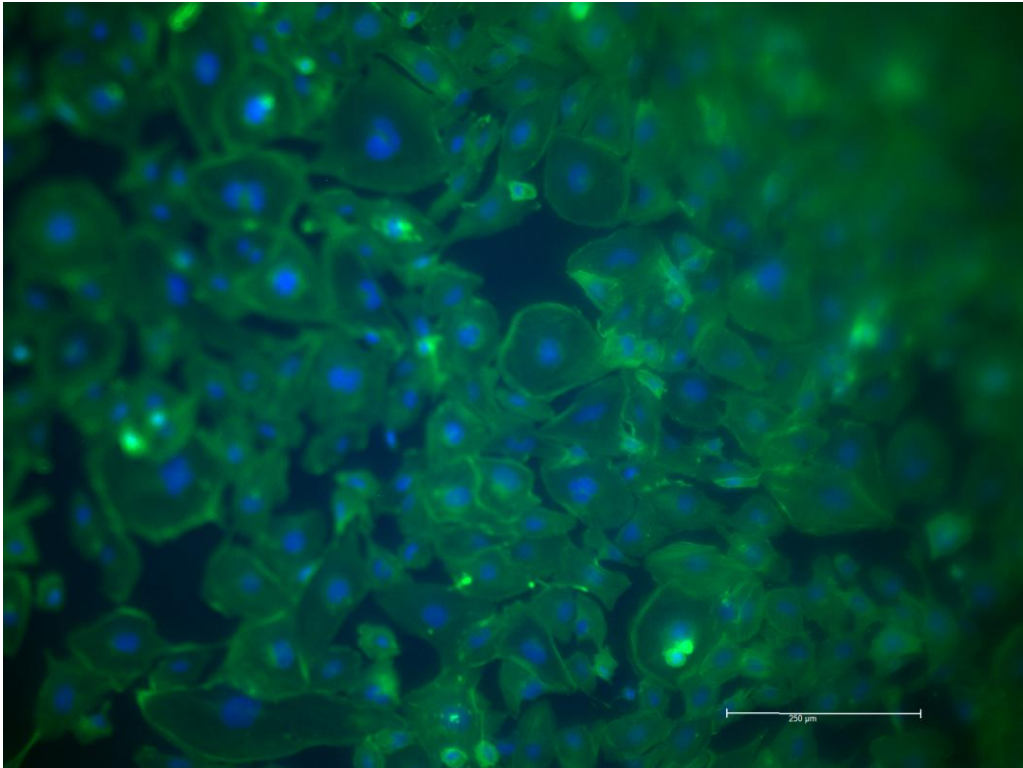


Figure 13: HMEC-1 on FEP tubing.

Top: Bioreactor I. Bottom: Bioreactor II.

DAPI stain in blue; phalloidin stain in green; 10x microscope objective.

3.2.2 PIV System

The PIV system used for these experiments was a standard high-resolution macroscopic setup. The laser beam was generated by a Nd:YAG double-pulsed laser emitting at 532 nm (LDP-100MQG, Lee Laser). The laser plane was formed using a 150 mm cylindrical lens and a 150 mm spherical lens, and was approximately 11 mm wide and 0.5 mm thick in the measurement region – a horizontal cross-section through the center of the vessel (Figure 14).

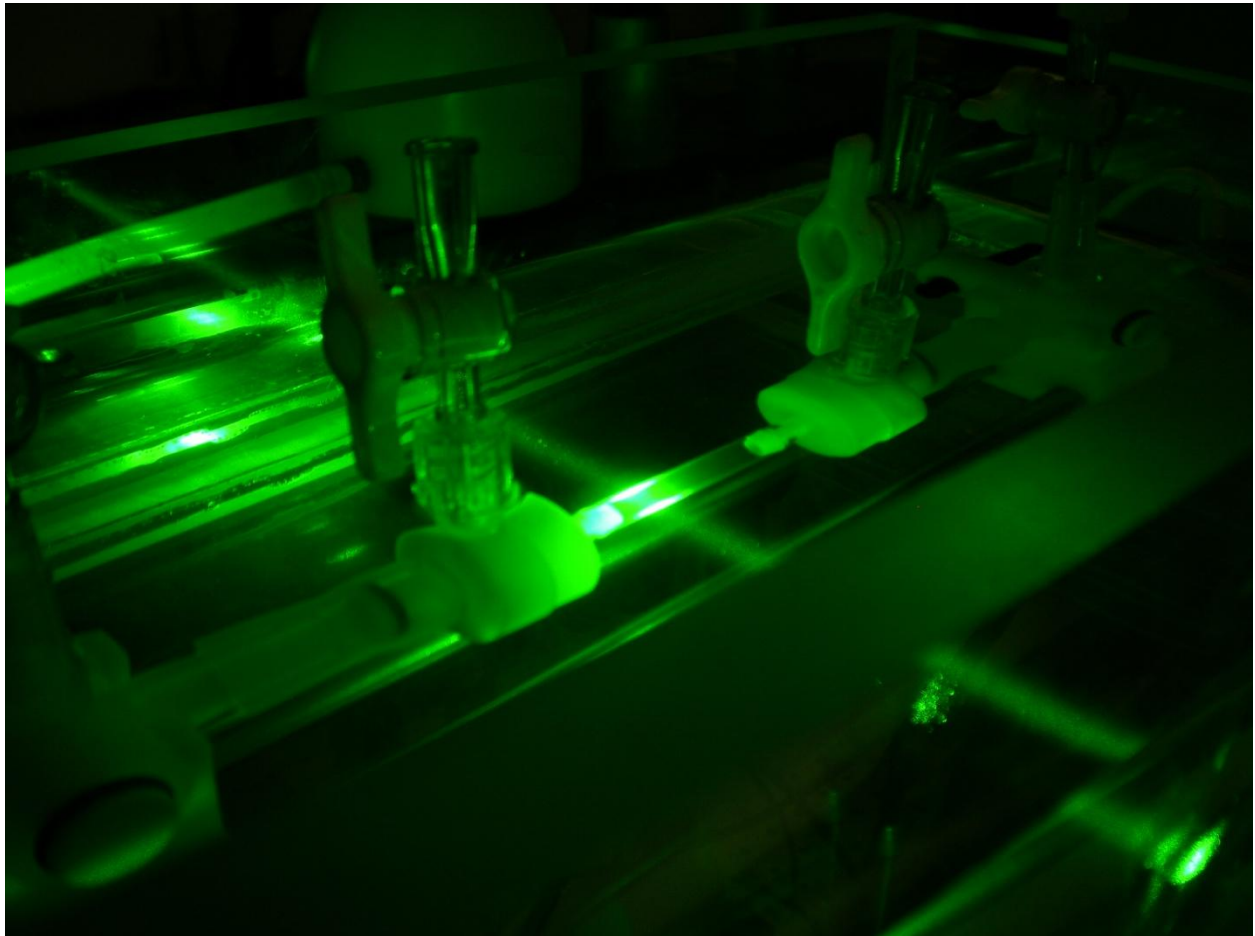


Figure 14: Laser plane passing through vessel cross-section.

Images were acquired with a 1.3 megapixel black and white CCD camera capable of imaging at up to 600 Hz (X-Stream XS-3, IDT) fitted with a standard lens (AF Nikkor 50 mm f/1.8D, Nikon). 25 mm of magnification tubing was inserted between the lens and the camera chip to obtain a field of view with a resolution of approximately $8.6 \mu\text{m}/\text{pixel}$. The camera was also

fitted with a 550 nm longpass filter (FEL0550, Thorlabs) to enhance the particle image quality by filtering out scattered laser light.

The laser pulses and camera shutter were synchronized using a pulse generator as an external trigger (Model 565 Pulse/Delay Generator, Berkeley Nucleonics). Figure 15 is a diagram of the triggering scheme used to obtain image pairs with the desired interframe time. The camera shutter is triggered to close and reopen almost instantly each time the signal value changes, while the laser is triggered by very short duration pulses.

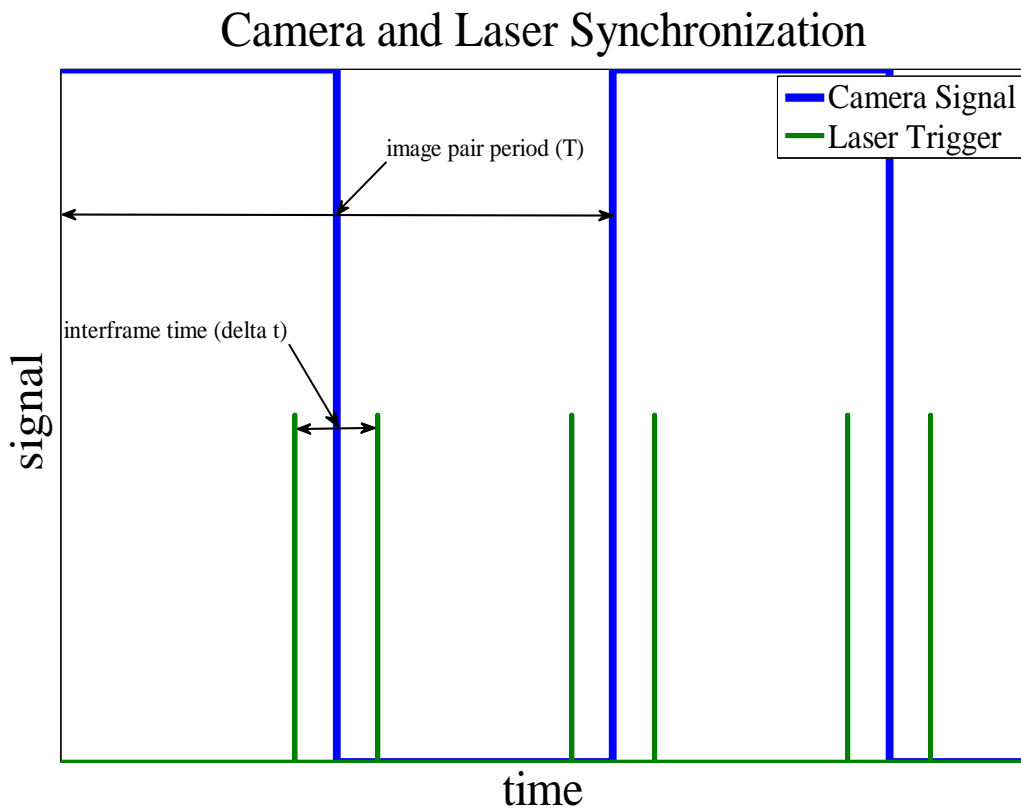


Figure 15: Diagram of PIV synchronization.

Image pairs for all flows were acquired at 250 Hz (the reciprocal, 4 ms, is the image pair period T). The interframe time (Δt) was determined so that the average particle displacement between images was on the order of 8 pixels, allowing most particles to remain in a 32x32 pixel correlation region (discussed later) while maintaining displacements large enough to overcome error due to pixel locking. For the $Re \sim 150$ cases, an interframe time of 1.2 ms was used, and for the $Re \sim 300$ cases an interframe time of 0.6 ms was used.

As described in Section 2.2.1, the bioreactor was IR matched with water and FEP to eliminate distortion of both the laser plane and the imaging system. This was successful, as the only distortion noticeable in the images was in the vessel walls. Three regions along the 60 mm vessel were imaged. The dimensions and location of each imaging section are shown in Figure 16, a cross-section of the vessel viewed from above. The laser plane entered the vessel through the wall depicted on the upper side of the diagram, called the top wall throughout this thesis. The laser plane exited through the wall on the lower side of the diagram, called the bottom wall. It should be noted that “top” and “bottom” refer only to the location of the wall in the images, and that the walls are in a horizontal plane in the physical system.

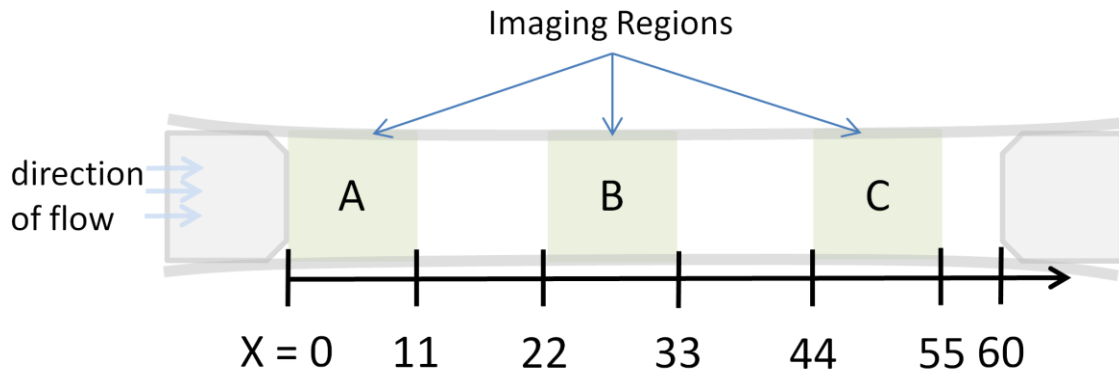


Figure 16: Imaging locations in vessel (mm).

Velocity field measurements were performed in vessel regions shaded green.

For the measurements without a cell layer in the vessel, distilled water was used as the working fluid in the bioreactor flow loop. Cell culture media (described in the next section) was used for the measurements with a cell layer. The dynamic viscosity and index of refraction of the media and of water were measured and compared to confirm that changing the fluid would not influence the PIV measurements. Dynamic viscosity was measured at 25C with a cone-plate viscometer (LVDV-II+ Pro Cone-Plate Viscometer, Brookfield) and RI was measured with a digital refractometer (Palm Abbe, Misco). The dynamic viscosity of the media was found to be between 0.8 and 1.0 mPa*s, while the dynamic viscosity of water was measured as approximately 0.9 mPa*s. A value of 1 mPa*s was used for estimation of Reynolds numbers. The index of refraction of the media, with a value of 1.336, is comparable to that of water, 1.33.

The flow was seeded with a solution of 3 μm diameter fluorescent microspheres (Aqueous Fluorescent Red Polymer Microspheres, Thermo-Fisher). These particles emit at 612 nm with peak excitation at 542, nearly the wavelength of the laser light. The density of the particles in solution, at 1.05 g/cm^3 , is close enough to that of water that inertial effects can be neglected and the particles can be assumed to faithfully follow the flow. The particles settle out of suspension over a period of several days. To maintain the suspension, the seeded fluid is sonicated for 5 minutes in a water bath shortly before PIV measurements are taken.

3.2.3 PIV Processing

MATLAB was used for processing of the PIV images and data analysis. An in-house PIV analysis program was used for image correlation and computation of pixel displacements. All computations were done in pixel coordinates, and scaling to physical dimensions was not performed until post-processing. The PIV code applies a robust phase correlation (RPC) technique, as described in (Eckstein and Vlachos 2009), in conjunction with a two-pass multigrid method with discrete window offset (DWO) (Westerweel, Dabiri et al. 1997). The first pass uses a window size of 64x64 pixels, filtered down from an original size of 128x128 pixels by the RPC filter. This window size allows the FFT (fast Fourier transform) of the RPC method to resolve the maximum particle displacement between images in a pair, which is on the order of 20 pixels. The second pass refines the correlation with a window size of 32x32 pixels reduced from 64x64 before RPC filtering. Both passes use a grid resolution of 8x8 pixels and an 8 pixel buffer at the image boundaries. A median universal outlier detection scheme (Westerweel and Scarano 2005) is implemented twice for each pass to eliminate invalid vectors. The parameters used for the PIV processing are summarized in Table 7.

Table 7: PIV processing parameters.

Grid	Multigrid (DWO)	
Number of Passes	2	
Validation Method	Median UOD	
Validation Neighborhood Radius (x,y) (vectors)	7,7	
Validation Threshold (x,y)	3,2	
Scaling	None	
Grid Resolution (x,y) (pixels)	8,8	
Grid Buffer (x,y) (pixels)	8,8	
	Pass 1	Pass 2
RPC Pre-filter Window Size (x,y) (pixels)	128,128	64,64
Window Size (x,y) (pixels)	64,64	32,32

Several steps were required for calculation of the wall shear stresses (WSS) within the vessel. First, the vessel wall position was manually located based on a bright field image of the vessel and a corresponding mask was created. These images were recorded with the PIV images at each location (A, B, C) and each set of data. Figure 17 is a sample image with corresponding mask. The mask was compared with particle images of the corresponding data set to confirm the size and location. The mask was used to determine the location at which shear stresses would be computed. This method assumes that the walls are linear and do not vary position over the period of a measurement, both reasonable assumptions for because of the inelasticity of the FEP vessel.

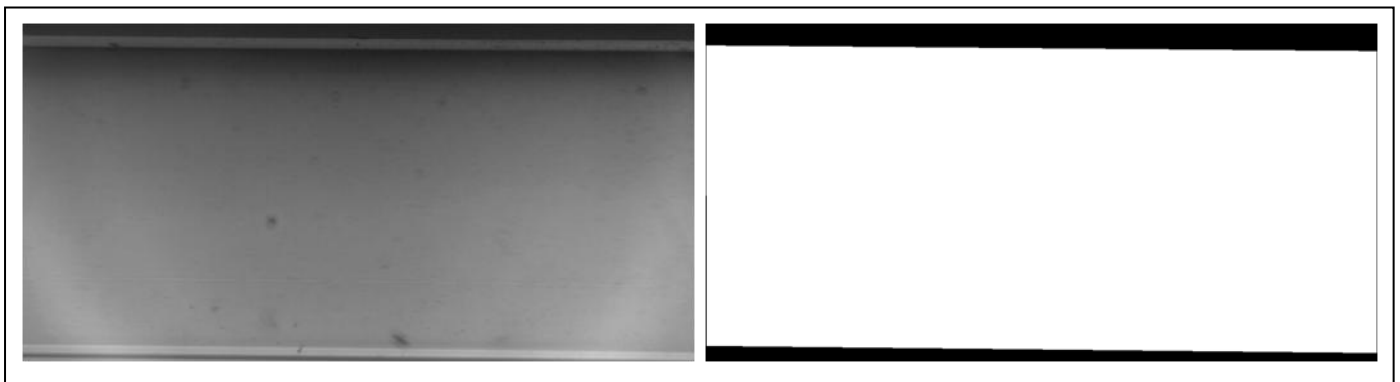


Figure 17: Bright field image (left) and corresponding mask (right).

Vessel location C; no cells.

Prior to calculation of WSS, further processing of the PIV data was required. For later comparison of data sets, it was necessary for all sets to be synchronized with respect to the flow pulsation. To achieve this, code was developed to locate the frame with maximum total longitudinal velocity and set that to be the initial frame. This was necessary because the pump and the PIV/imaging system were not synchronized during the measurements, and so each data set began at a random time within the flow cycle.

Next, the ensemble average of each data set over several flow cycles was computed. This was possible because of the periodicity of the flow and greatly increased the statistical significance of the resulting vector fields. 2000 images (the maximum with the available onboard camera memory) were recorded for each flow, corresponding to 4 cycles for the flows with $Re \sim 150$ (392 images/196 PIV correlations per cycle) and 9 cycles for the $Re \sim 300$ flows (198 images/99 PIV correlations per cycle). To compute the ensemble average, the linear average of the vectors at each coordinate for corresponding frames of each cycle was computed.

The method described in (Charonko, Karri et al. 2009) for computation of wall shear stress in stented arteries was used for this work. The primary modification made to the original method was implementation of the linear static mask for wall position. The key features of the original method – use of proper orthogonal decomposition and radial basis functions as discussed in (Karri, Charonko et al. 2009) – were retained.

Tecplot 360 was used for data visualization. The vessel locations were combined to form a single data set for each flow and the data was nondimensionalized. The axes were nondimensionalized (x^*, y^*) based on the nominal vessel diameter (Equations (7) and (8)) and the origin placed longitudinally at the inlet (as in Figure 16) and laterally at the vessel center.

$$x^* = \frac{x}{D} \tag{7}$$

$$y^* = \frac{y - \frac{H}{2}}{D} \tag{8}$$

The particle displacement vectors were nondimensionalized using the Reynolds number based on the vessel diameter (Equation 4).

Both the magnitude and oscillatory character of the wall shear stress are of interest. In addition to the wall shear stress computed at each axial location for each instant within the cycle, $\tau_w(x,t)$, the axially-varying time-averaged wall shear stress $\overline{\tau_w}(x)$ was computed (Equation 9).

$$\overline{\tau_w}(x) = \frac{1}{N_t} \sum_{i=1}^{N_t} \tau_w(x, t_i) \quad (9)$$

Additionally, the oscillatory shear index, or OSI, is a scalar parameter that quantifies the degree of oscillation of wall shear stress during the flow cycle (Takizawa, Moorman et al. 2010). The OSI is defined in Equation (10):

$$OSI(x) = \frac{1}{2} \left(1 - \frac{\frac{1}{T} \left| \int_0^T \tau_w(x, t_i) dt \right|}{\frac{1}{T} \int_0^T |\tau_w(x, t_i)| dt} \right) = \frac{1}{2} \left(1 - \frac{\left| \sum_{i=1}^{N_t} \tau_w(x, t_i) \right|}{\sum_{i=1}^{N_t} |\tau_w(x, t_i)|} \right) \quad (10)$$

The OSI measures the temporal variation of the wall shear stress, and varies between 0 and 0.5. A value of 0 indicates a region with no reversal of flow, while a value of 0.5 arises from pure oscillatory flow. These two parameters, OSI and time-averaged WSS, are often used in arterial flow analysis to capture the oscillatory nature of the wall shear stress (Kleinstreuer, Hyun et al. 2001).

3.3 Results and Discussion

Qualitatively, the flow in all cases behaves as an internal jet. Because the internal diameter of the inlet fitting is 3.3 mm, the cross-sectional area at the entrance is just over half the cross-sectional area beyond the inlet ($A_{entrance}/A_{vessel} = 0.52$). This leads to strong jet effects such as reverse flow and circulation in the near-wall regions just beyond the inlet. These can be seen in the A location of each flow. Further downstream from the inlet, the jet effects are reduced and

the flow develops a flatter profile. By the time the C location is reached, a smooth, nearly symmetric profile is achieved. Figure 19 is an example that clearly shows these effects in the $Re \sim 150$ pulsatile flow case with no cells. In this figure, each location (A, B, C) is shown to scale. The top shows the nondimensionalized velocity fields (for clarity, not all vectors are shown). At each wall, the instantaneous wall shear stress is indicated with a color contour. The bottom shows the instantaneous wall shear profile, with the top wall shown in red and the bottom wall in blue.

For both cases – with and without cells – the “quasi-steady” case exhibits too much oscillation to be useful for comparison with the pulsatile case. Although the flow loop was adjusted to reduce oscillation in the vessel and the pressure wave for these cases was flatter than for the pulsatile cases, strong oscillation was generated in the flow. This can be seen in the $\overline{\tau_w}(x)$ and OSI values for e.g. the $Re \sim 150$ quasi-steady case (Figure 18). The OSI ranges between 0 and 0.5 for all three locations (A, B, and C), indicating high levels of oscillation.

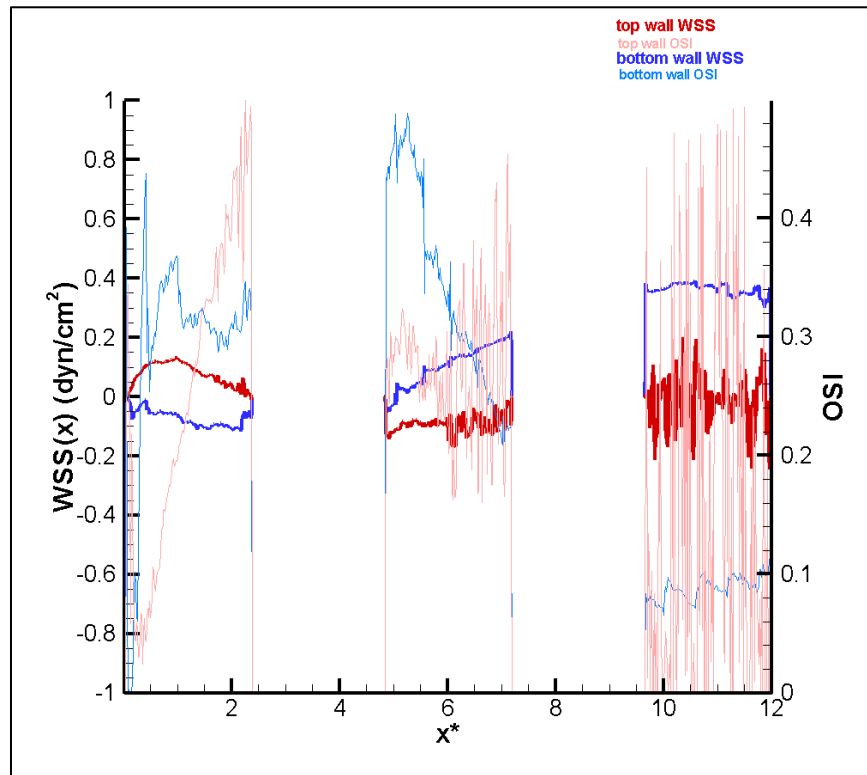


Figure 18: Time-averaged WSS and OSI for quasi-steady case.

Top wall WSS shown in red; bottom wall WSS in blue. Top wall OSI shown in pink; bottom wall OSI in light blue.

$Re \sim 150$; no cells.

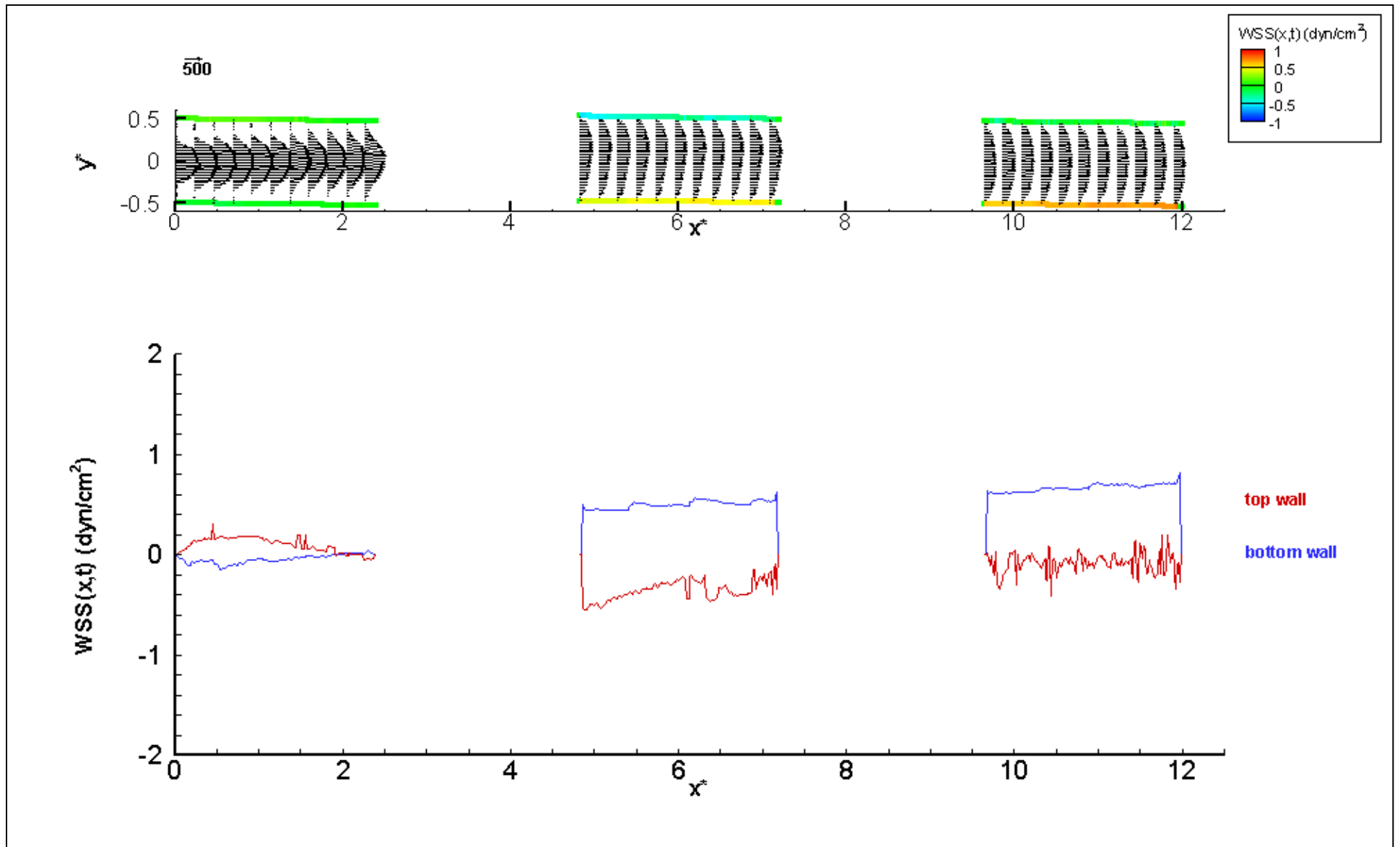


Figure 19: $Re \sim 150$ pulsatile flow; no cells; peak flow ($t = 0$).

3.3.1 Case without cell layer

In the case without the cell layer, the flow is relatively symmetric throughout the cycle, a feature reflected in the wall shear stress profiles. Figure 19 and Figure 20-Figure 22 show the $Re \sim 150$ pulsatile flow at four equal intervals throughout the cycle, from peak flow with $t = 0$, to $t = T/4$, $t = T/2$, and $t = 3T/4$. Similar figures for the other cases, both with and without cells, can be found in Appendix B: Additional Figures.

For the $Re \sim 150$ pulsatile case, the shear stress fluctuates between a minimum of -0.55 dyn/cm^2 and a maximum of 0.82 dyn/cm^2 . Although the $Re \sim 300$ case is qualitatively very similar to the $Re \sim 150$ case, the instantaneous wall shear stresses in the $Re \sim 300$ case are approximately twice those in the $Re \sim 150$ case, ranging from -1.2 dyn/cm^2 to 2.0 dyn/cm^2 . The OSI for both cases rises throughout the A region and drops further downstream from the inlet as the flow becomes developed (Figure 23 and Figure 24). In these figures, it can also be seen that the magnitude of the time-averaged wall shear stress decreases to zero near the end of the A section, where the sign changes and the magnitude begins to increase further downstream.

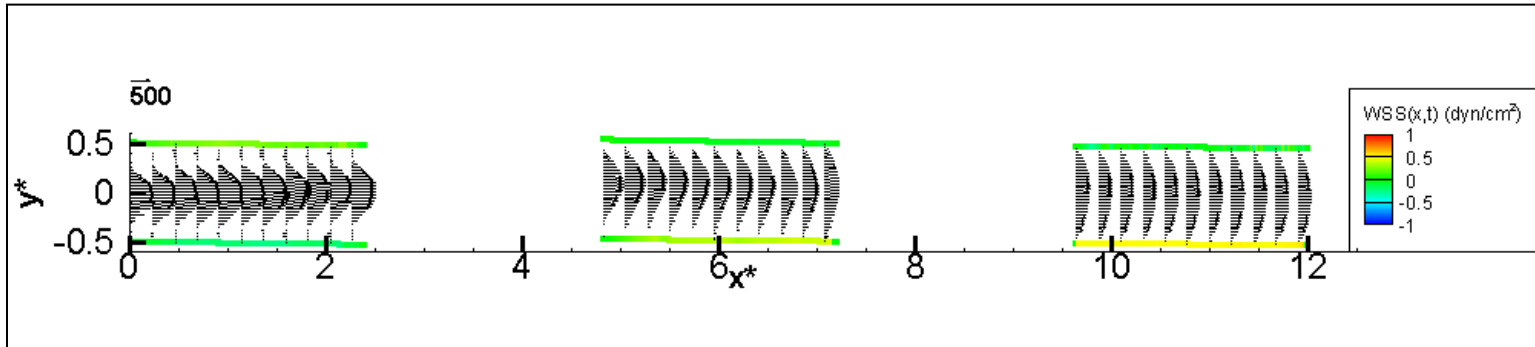


Figure 20: $Re \sim 150$ pulsatile flow; no cells; $t = T/4$.

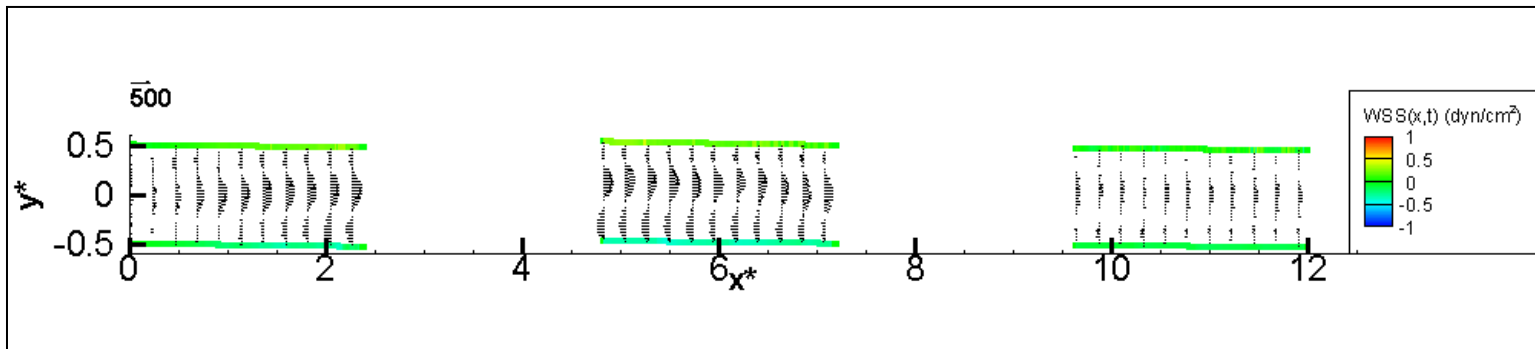


Figure 21: $Re \sim 150$ pulsatile flow; no cells; $t = T/2$.

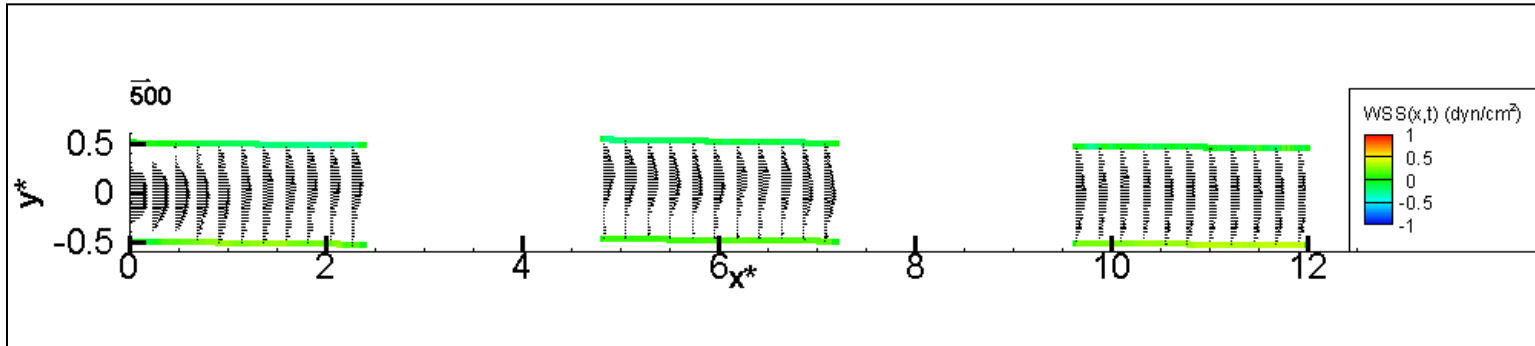


Figure 22: $Re \sim 150$ pulsatile flow; no cells; $t = 3T/4$.

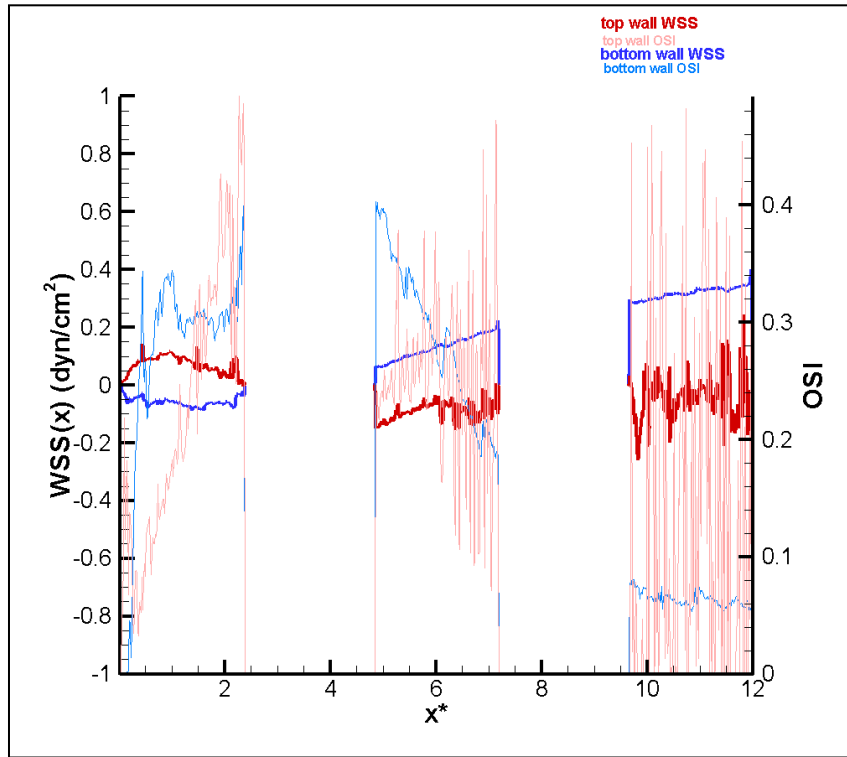


Figure 23: Time-averaged WSS and OSI for $Re \sim 150$ pulsatile flow; no cells.

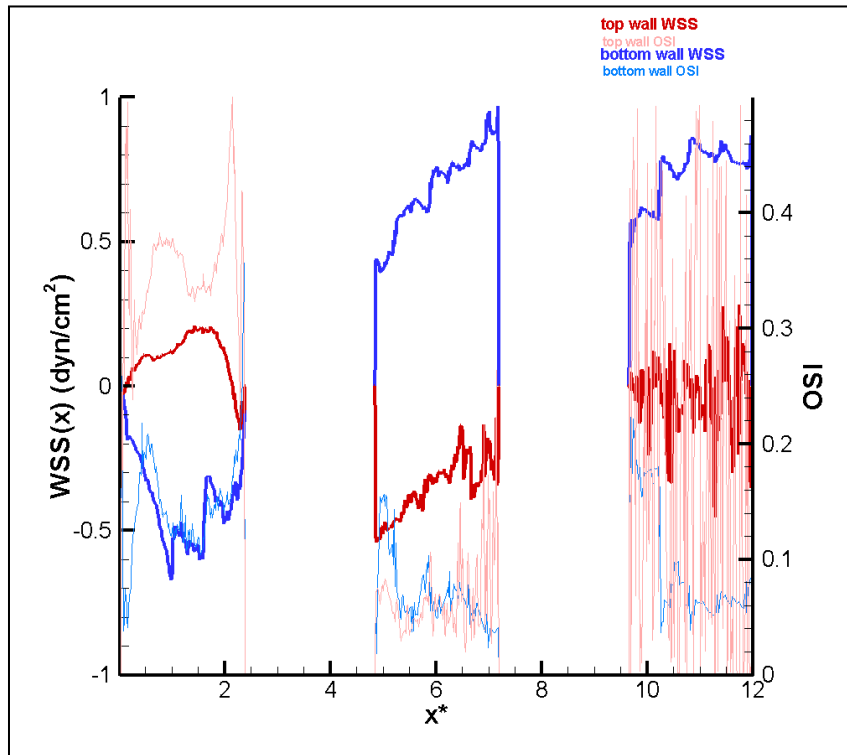


Figure 24: Time-averaged WSS and OSI for $Re \sim 300$ pulsatile flow; no cells.

3.3.2 Case with cell layer

Before particle images were recorded, the presence of an HMEC layer on the vessel for the cases with cells was confirmed in the bright field images. Bright field images for the vessel in the cases with and without cells are compared in Figure 25. For the case with cells, the layer can clearly be seen just inside the vessel boundary, becoming more distorted towards the center of the vessel where the vessel wall recedes from the camera image plane. Because ECs are composed of thin transparent membranes enclosing a water-based fluid, the EC layer on the



vessel did not create distortion in the PIV measurements.

Figure 25: Bright field images of vessel without cells (top) and with cells (bottom).

Vessel location B.

In the particle images, a marked increase in the number of particles at the vessel walls indicates particle aggregation within the endothelial layer (Figure 26). The level of particle aggregation decreases with increasing distance from the inlet, suggesting that particle adhesion is dependent on flow conditions. The particles remained adhered to the cell layer even after flushing of the vessel with particle-free fluid, as can be seen in the post-PIV fluorescence images (Figure 13).

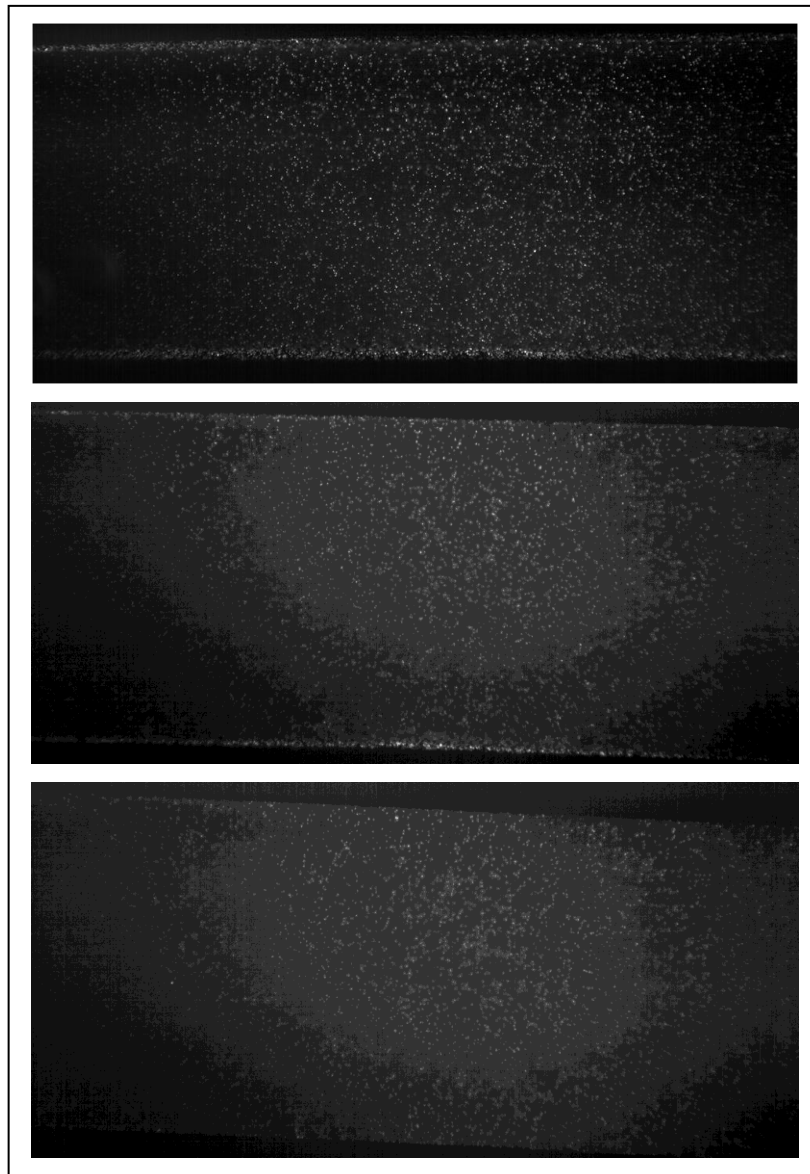


Figure 26: Particle images of vessel with cells.

Top: Vessel location A. Middle: Vessel location B. Bottom: Vessel location C.

Because the vessel with the cell layer exhibits curvature along its length, the flow profiles for the cases with cells exhibit a high degree of asymmetry, which can be seen in Figure 28. When compared with the corresponding cell-free case (Figure 19), the level of asymmetry becomes apparent. It should be noted that the illumination of the lower left section of all images of the vessel with cells was poor due to asymmetry of the laser plane and that the correlations in that region are invalid.

High-frequency fluctuations are present in the wall shear stress and OSI computed for the cases with cells. Although these fluctuations are also present in the case without cells, their presence is far more marked in the cases with cells than in the cases without cells. This can be seen by comparing Figure 27 and Figure 29 with Figure 23 and Figure 24.

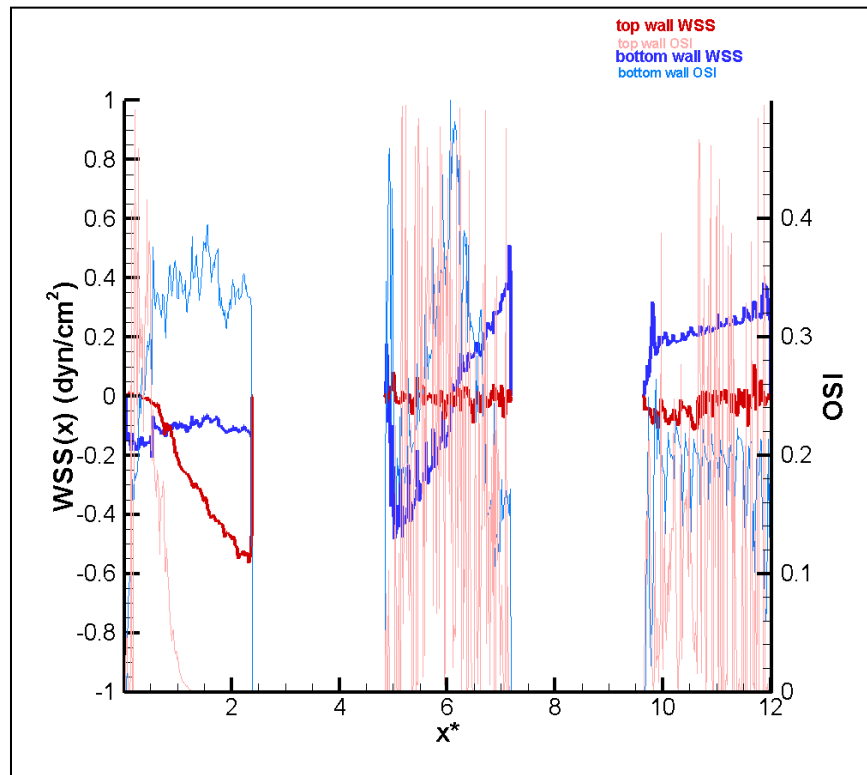


Figure 27: Time-averaged WSS and OSI for $Re \sim 150$ pulsatile flow; with cells

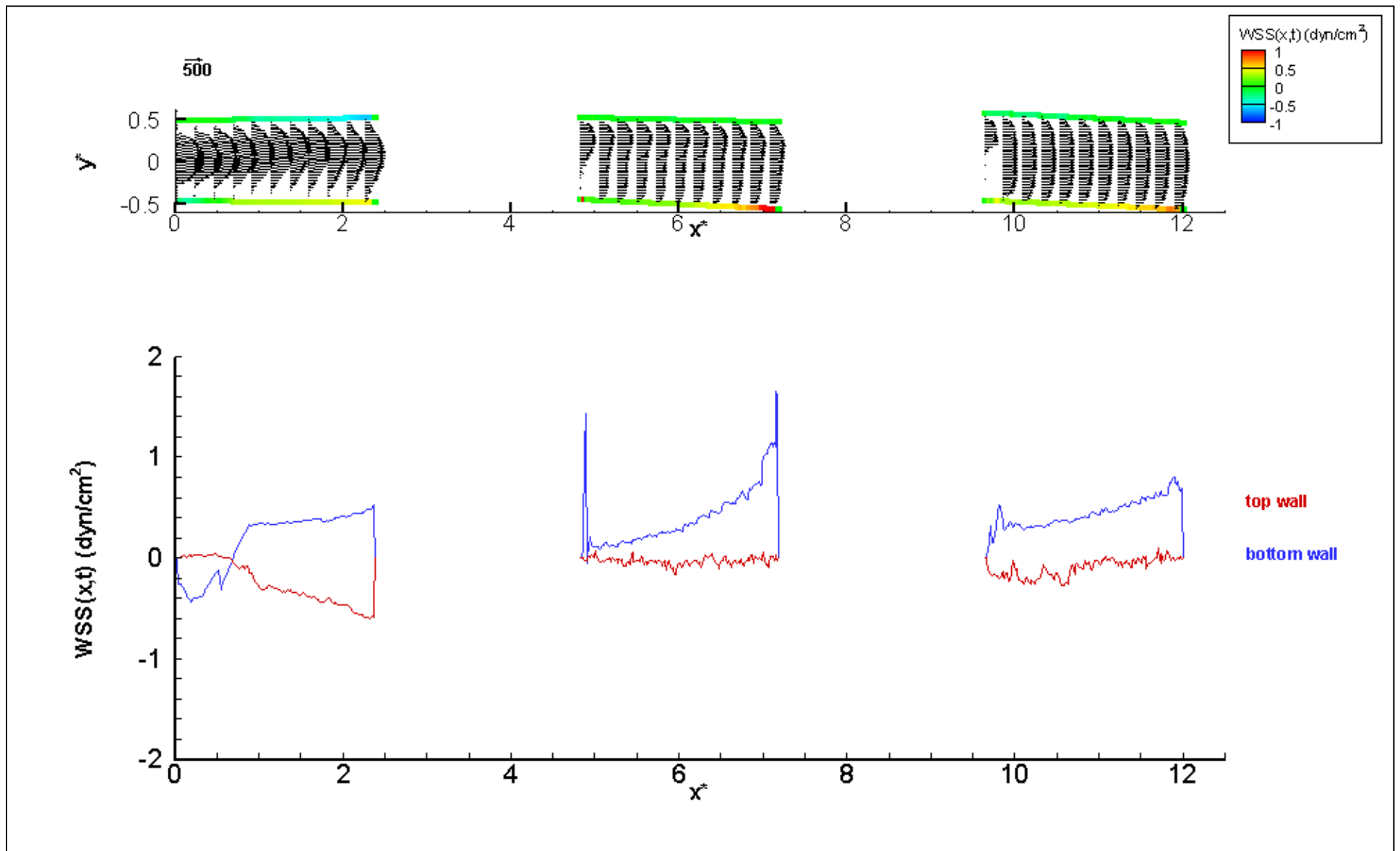


Figure 28: $Re \sim 150$ pulsatile flow; with cells; peak flow ($t=0$).

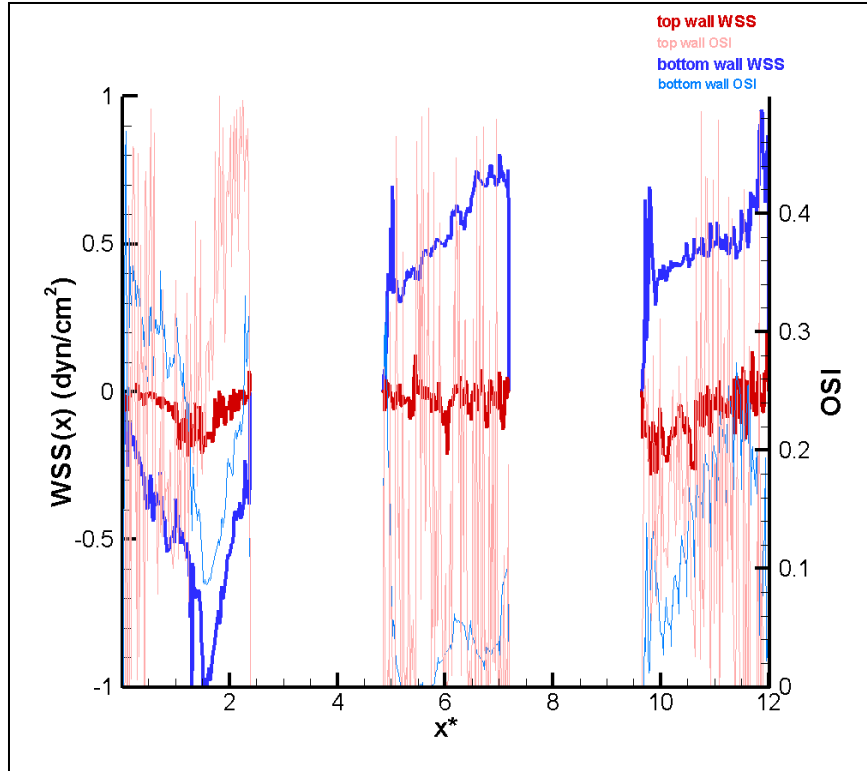


Figure 29: Time-averaged WSS and OSI for $Re \sim 300$ pulsatile flow; with cells.

It is notable that the position at which the sign of the wall shear changes (at location A) is considerably further upstream (over one diameter) for the case with cells than for the case without cells. This can clearly be seen in Figure 28 and is also reflected in Figure 30 and Figure 31. These figures and the following compare the variation in WSS and OSI in the cases with and without cells with basic statistical parameters. The mean, standard deviation, maximum and minimum of the time-averaged WSS and OSI were calculated along the length of each measurement section for both the top and the bottom wall and are represented in these figures.

The cases without cells all have positive mean time-averaged WSS along the top wall and the cases without cells have negative mean time-averaged WSS. Along the bottom wall, although the mean time-averaged WSS is negative for all cases, the magnitude is greater for the case with cells than for the case without cells. Also apparent in this figure is the much larger standard deviation for almost all cases with cells. As the flow progresses to location B and finally to location C, the cases with cells tend to have time-averaged WSS lower than the cases without cells.

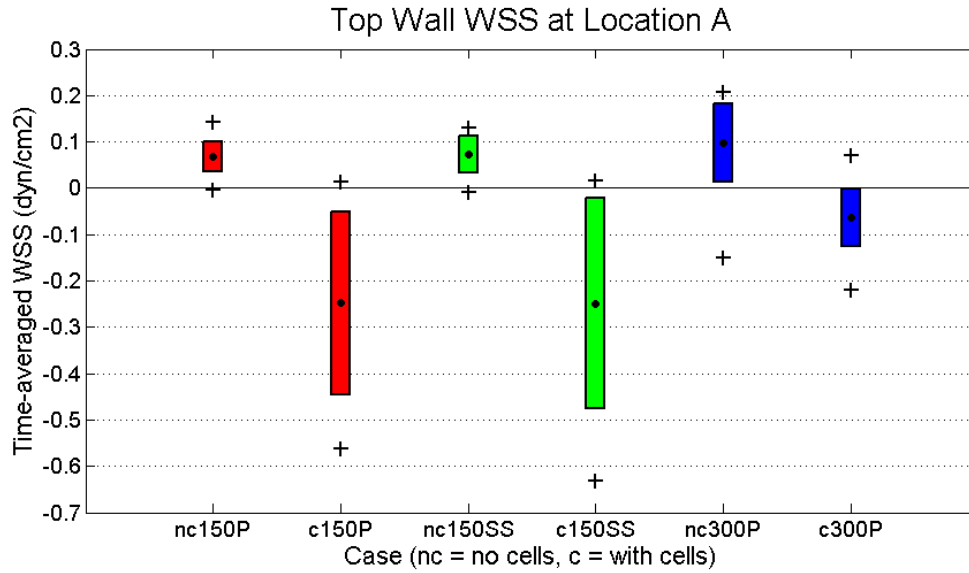


Figure 30: Statistical distribution of top wall time-averaged WSS at location A.

• represent mean values. + represent maxima and minima.

Each bar extends one standard deviation above and below the mean.

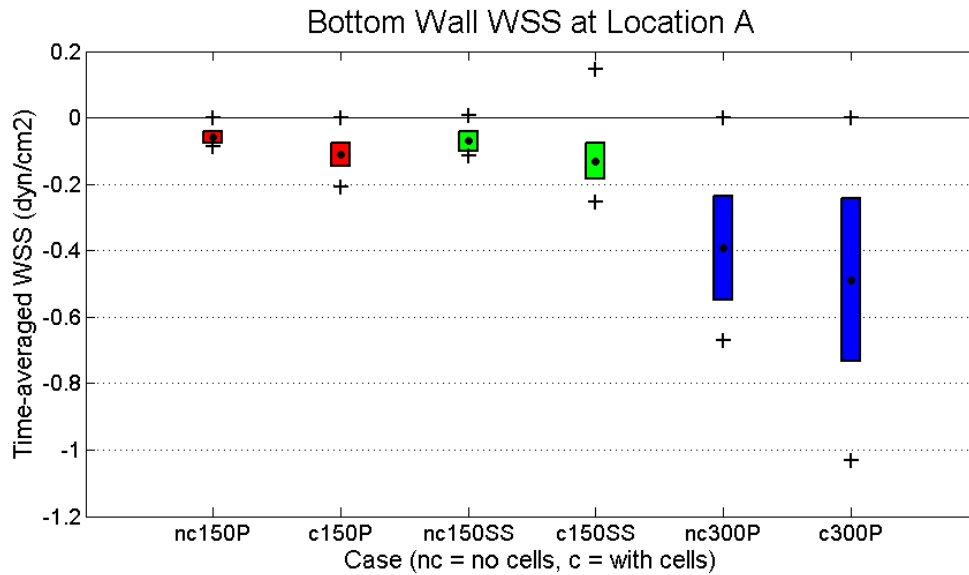


Figure 31: Statistical distribution of bottom wall time-averaged WSS at location A.

The mean OSI at location A is between 0.05 and 0.35 for the cases with and without cells, indicating a medium level of oscillation in that region (Figure 32 and Figure 33). Further downstream the mean OSI drops to 0.05-0.2 at location C (Figure 34 and Figure 35). Throughout the vessel, the standard deviation of cases with cells tends to be larger than that of the cases without cells.

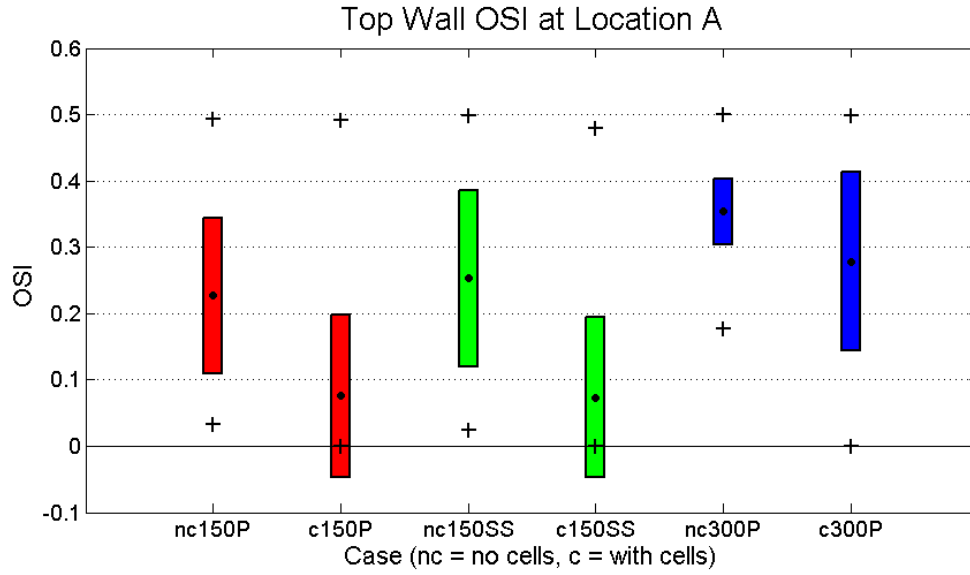


Figure 32: Statistical distribution of top wall OSI at location A.

Note that although the standard deviation of OSI extends to negative values, only values between 0 and 0.5 are possible.

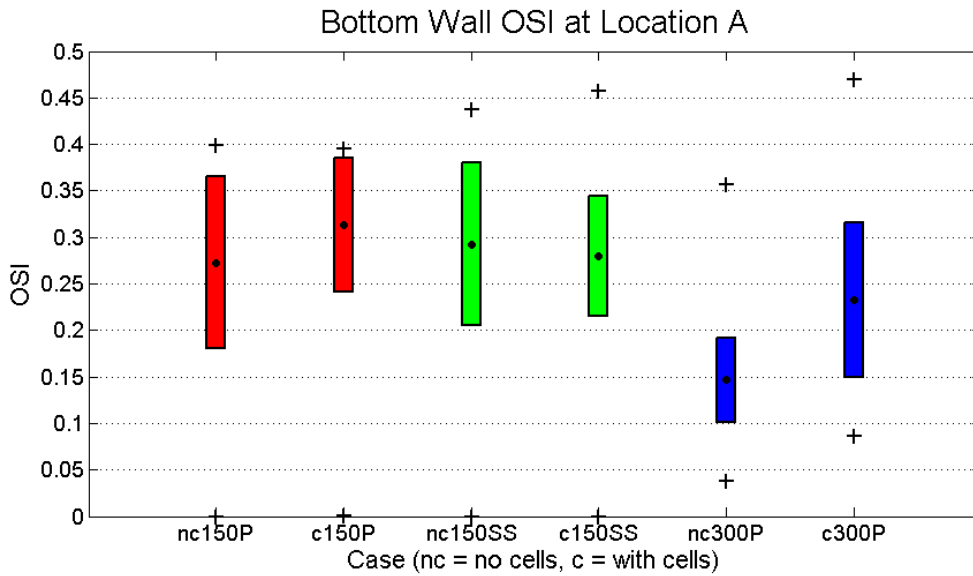


Figure 33: Statistical distribution of bottom wall OSI at location A.

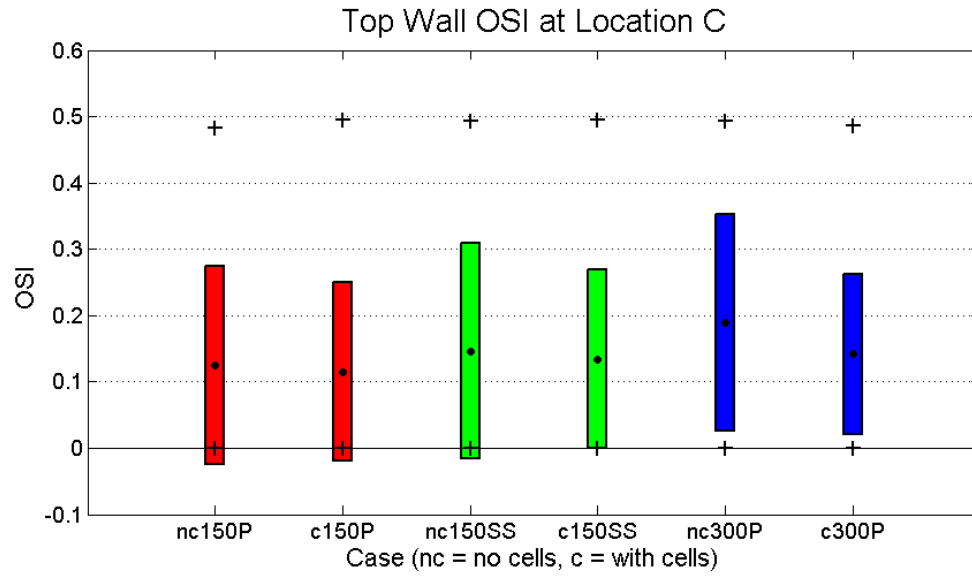


Figure 34: Statistical distribution of top wall OSI at location C.

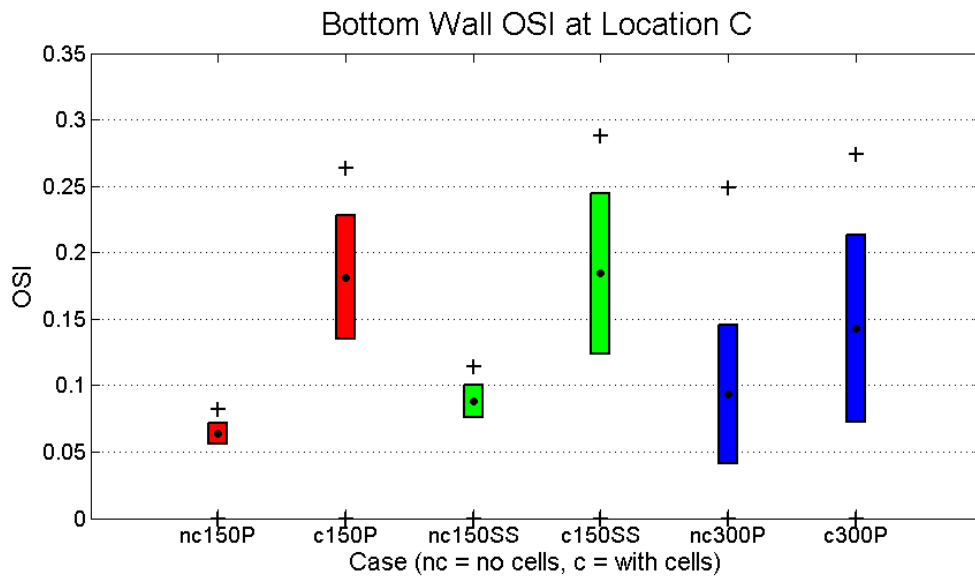


Figure 35: Statistical distribution of bottom wall OSI at location C.

3.3.3 Error Analysis

The results presented here establish a new capability for PIV measurements within a cylindrical bioreactor under pulsatile flow conditions. They are, however, subject to several sources of error. Measurement uncertainty and difficulty in reproducibility are present within all components of the system and all phases of measurement. Some potential sources of error and experimental variation are discussed briefly here, and are categorized by component of the system: the bioreactor, the flow control and generation, the PIV measurement system, and the PIV analysis. Accurate quantification of the errors in all but the PIV analysis is not possible without further knowledge of the system, so these errors are only discussed qualitatively here.

The method used to develop the layer of endothelial cells on the artificial vessel in the bioreactor can be easily repeated; however, due to variation in the culture conditions, biological agents, and the natural variation in living organisms, significant variability is to be expected in future measurements. Under the same nominal conditions, different cellular morphology and viability are expected for each trial. These variations likely influence the cellular response to flow and levels of gene expression, and depending on the extent of these variations, the flow within the vessel could be altered. Fortunately, these random variations can be overcome by repeating experiments with multiple artificial vessels seeded under the same conditions in order to obtain statistical information about the variation due to the cell layer.

Variations in the physical flow loop are expected to create further random error in the results. Because several components of the flow loop must be replaced because of sterilization requirements, absolute reproducibility of the system is not possible. Differences in lengths of replacement tubing sections and the fill level of the pulse dampener are certain to cause variation in total resistance and capacitance of the flow loop. The diameter and curvature of the artificial vessel exhibit variance due to the manufacturing process. As was seen in these results, even the slight curvature in the vessel with cells caused different flow profiles within the entrance region of the flow. Even adjusting the physical location of flow loop components relative to one another can lead to variation in the flow profile across the vessel, changing the wall shear stresses. However, for fully developed flow, these variations are expected to be minimal.

Although the pressure and flow of the system were calibrated with known values, systematic error may also be present in those measurements.

The complexity of the PIV measurements leads to several sources of error. Although the size, shape, and intensity of the laser plane are easily duplicated between measurements, the exact alignment of the vessel with respect to the laser plane can vary with each experiment. The orientation of the camera with respect to the laser plane also varies slightly between measurements. Additionally, because of the extremely low volumes of particle solution added to a large volume of water or cell culture media, the particle seeding density exhibits variation between measurements. If the variance in seeding density is low, however, it is not expected to be propagated through the PIV analysis. Other sources of experimental error in the PIV system include distortion in the imaging optics,

The errors present in the PIV processing and post-processing have been studied previously and are relatively well-characterized. Standard PIV has associated random and bias errors, and although the bias errors are not magnified by the postprocessing computations, even small random errors can lead to large inconsistencies in the wall shear stress measurements. These errors come from many sources, such as discretization of pixel intensity and location (the latter leading to peak-locking in displacement estimations), out-of-plane motion of particles, and particle overlap, as some examples. The post-processing is not expected to introduce new error to the system, but it magnifies the error present in the PIV correlations. The following section presents a discussion of these errors, primarily the random errors, and a quantitative analysis of the propagation of error through the PIV measurements.

3.3.4 Estimation of PIV Error

To quantify the reliability of the WSS and OSI measurements presented here, a brief analysis of the propagation of random error through the PIV analysis and wall shear stress computations was performed. Because of the implementation of the discrete window offset (DWO) in the PIV correlation scheme (described in detail in (Westerweel, Dabiri et al. 1997)), the accuracy of the particle displacement measurements is estimated to be better than 0.1 pixels/frame. The average displacement between frames for each flow case can be computed from the average flow rate and the imaging parameters, and is estimated to be 5 pixels. This indicates that the average

uncertainty (ϵ) of the velocity field measurements is 2%. Because the near-wall velocity is lower than the average flow velocity, those measurements have a higher uncertainty, estimated to be near 5%.

The propagation of the velocity field error through the estimation of wall shear stress is addressed in detail in (Karri, Charonko et al. 2009). The total uncertainty in wall shear stress calculations for pipe flow varies depending on the original error in PIV measurements, the gradient estimation scheme applied, the ratio of pipe radius to grid spacing, and the size of the grid used for gradient interpolation. Plots of these relationships are graphed for both Poiseuille flow and pulsatile flow. For this work, the estimated PIV measurement uncertainty is 5%, and the interpolation grid size of 5x5 vectors was used for gradient estimation with a thin plate spline. The ratio of pipe radius to grid spacing is 0.03. Using these values, the random error in instantaneous wall shear stress measurements $\epsilon_{\tau_w(x,t)}$ for pulsatile flow is estimated from the figures in (Karri, Charonko et al. 2009) to be near 40%. It is assumed that bias error contributes little to this value, as bias and random error contribute to total error by a sum-of-squares method (Equation 11).

$$\epsilon_{tot} = \sqrt{\epsilon_{rand}^2 + \epsilon_{bias}^2} \quad (11)$$

Even a bias error as large as 20%, when added to a random error of 40%, results in a total error of only 44%, an increase of 10%. Bias errors in PIV velocity measurements are typically much less than 20% and, unlike random errors, are not augmented by the shear stress calculations, so they can safely be neglected without influencing the magnitude of the estimated uncertainty.

This high level of error in the instantaneous wall shear stress measurements $\tau_w(x,t)$ – on the order of 40% – explains the high level of noise seen in Figure 28 and similar figures. Fortunately, the magnitude of this error as it is propagated through the computation of time-averaged WSS $\overline{\tau_w(x)}$ and OSI is greatly reduced. Following the method described by (Charonko 2009), standard error propagation formulae to compute the error in time-averaged WSS and in OSI from the error in instantaneous WSS (Equations 11 & 12) were used.

$$\varepsilon_{\tau_w}^2 = \sum_{i=1}^{N_t} \left(\frac{\partial \overline{\tau_w}(x)}{\partial \tau_w(x, t_i)} \right)^2 \cdot \varepsilon_{\tau_w(x, t_i)}^2 \quad (12)$$

$$\varepsilon_{OSI}^2 = \sum_{i=1}^{N_t} \left(\frac{\partial OSI(x)}{\partial \tau_w(x, t_i)} \right)^2 \cdot \varepsilon_{\tau_w(x, t_i)}^2 \quad (13)$$

Referring to the definitions of instantaneous WSS and OSI from Equations 9 and 10 and using Equations 11 and 12, the following expressions for the error in instantaneous WSS and OSI can be derived:

$$\varepsilon_{\tau_w}^2 = \frac{\sum_{i=1}^{N_t} \varepsilon_{\tau_w(x, t_i)}^2}{N_t^2} \quad (14)$$

$$\varepsilon_{OSI}^2 = OSI \cdot \frac{\sum_{i=1}^{N_t} \varepsilon_{\tau_w(x, t_i)}^2}{\left(\sum_{i=1}^{N_t} |\tau_w(x, t_i)| \right)^2} \quad (15)$$

These expressions can be analytically solved if an assumption about the shape of the WSS profile throughout the flow cycle is made. Here, the profile was assumed to be sinusoidal. The error in both time-averaged WSS and OSI were calculated for each flow case from Equations 14 and 15 using experimental parameters and the assumed sinusoidal profile as defined in Table 8.

Table 8: Error estimation parameters.

Flow	Assumed average WSS (dyn/cm ²)	Assumed amplitude of WSS profile (dyn/cm ²)	N _t (data samples)	Relative error in instantaneous WSS (%)
Re ~ 150	0.3	1.0	196	40
Re ~ 300	0.5	2.0	98	40

The estimated measurement error computed for the time-averaged WSS, normalized by the amplitude of the sine wave, was found to be 2.2% for the case with $Re \sim 150$ and 3.1% for the case with $Re \sim 300$. The estimated OSI measurement error was normalized by the OSI of the sine wave, 0.5, and was calculated to be 4.7% for $Re \sim 150$ and 6.7% for $Re \sim 300$. The estimated error is higher for the higher Reynolds number because the number of data samples for averaging is lower. Clearly, the computation of both time-averaged WSS and OSI is expected to average out most of the random error, reducing error levels from 40% to near 5%. This shows that, although the measurement error in each individual measurement may be high, the error in the reported values for time-averaged WSS and for OSI can be expected to be considerably lower. The values estimated here compare with those estimated in (Charonko 2009) using a similar method but lower initial error estimates.

4 Conclusions and Recommendations

This thesis describes the first use of PIV within a cylindrical vessel lined with live cells. From the figures in the previous section, it is clear that little quantitative comparison of the flows is possible unless modifications are made. Too much fluctuation and variation is present in both cases for meaningful quantitative comparisons to be made. However, a conclusion that can be made is that the flow present in this type of system is far more complex than it seems, containing rotational structures and highly irregular oscillations. The assumption used in previous investigations into the correlation between vessel wall shear stress and cellular response is that the flow being generated by such systems exhibits a smoothly oscillating WSS. The results presented here show that this is **not** a valid assumption, and that such systems must be better characterized before assumptions about the WSS in the vessel can be made.

Improvements to the data analysis and validation must be made. The high levels of noise present in the WSS and OSI measurements are most likely due to error in the PIV correlation and subsequent stress analysis, and are not likely present in the physical system. It is, of course, also possible that the fluctuations are caused by interaction of the cell layer with the flow, a possibility that should be further investigated. However, measurement error must be addressed before such effects can be quantified.

The first step will be to further improve the PIV processing and WSS computation parameters. Because the exact location of the vessel wall is unknown and strong gradients exist in shear near the wall, considerable error can be introduced in the WSS computations. The addition of a pre-processing stage to the analysis to remove static particles at the walls from the images is likely to improve the accuracy of the PIV correlations near the vessel walls. An algorithm should be developed to more accurately find the location of the wall, especially for the case with a cell layer present. Another improvement that can be made to the measurement technique is implementation of synchronization between the laser and the pressure wave so that the instantaneous pressure drop across the vessel can be used in conjunction with results of the PIV analysis to check the physical consistency of the measurements.

Before further experiments can be conducted using this system, it should be improved to exhibit flow more similar to true physiological flow. Although the longest straight section of artery available is on the order of 8 cm, it may be necessary to use a longer section in the system to obtain the fully developed flow expected in blood vessels. Other modifications may be made to further improve the flow profile within the vessel.

The next step should be to use the pulsatile flow system during development of an HMEC layer to obtain more typical cell morphology. Protein expression assays can be used in conjunction with PIV for different flow rates to directly quantify cell response to shear stress and OSI. Another future experiment is the co-culturing of cancer and endothelial cells to characterize the influence of shear stress on crosstalk (gene and protein expression) between the two types of cells to develop a better understanding of cancer metastasis.

To summarize, this thesis describes the design, construction, and validation of an *in vitro* model for physiological flow in a biological environment. PIV measurements were taken within the vessel section with high spatial (8.6 microns) and temporal resolution (4 ms). Although the initial data taken with this system were inconclusive, it was proven that the system developed here provides a new capability to obtain flow measurements with high temporal and spatial resolution in a biological environment.

References

- Adrian, R. J. (1991). "Particle-Imaging Techniques for Experimental Fluid-Mechanics." Annual Review of Fluid Mechanics **23**: 261-304.
- Adrian, R. J. (2005). "Twenty years of particle image velocimetry." Experiments in Fluids **39**(2): 159-169.
- Ajima, K., T. Murakami, et al. (2008). "Enhancement of In Vivo Anticancer Effects of Cisplatin by Incorporation Inside Single-Wall Carbon Nanohorns." Acs Nano **2**(10): 2057-2064.
- Alberts, B. (2002). Molecular biology of the cell. New York, Garland Science.
- Banquy, X., G. Leclair, et al. (2008). "Selectins Ligand Decorated Drug Carriers for Activated Endothelial Cell Targeting." Bioconjugate Chemistry **19**(10): 2030-2039.
- Bitsch, L. and L. H. Olesen (2003). Micro PIV on blood flow in a microchannel. 7th International Conference on Miniaturized Chemical and Biochemical Analysis Systems.
- Bitsch, L., L. H. Olesen, et al. (2005). "Micro particle-image velocimetry of bead suspensions and blood flows." Experiments in Fluids **39**(3): 505-511.
- Burgmann, S., S. Grosse, et al. (2009). "A refractive index-matched facility for fluid-structure interaction studies of pulsatile and oscillating flow in elastic vessels of adjustable compliance." Experiments in Fluids **47**(4-5): 865-881.
- Califano, J. P. and C. A. Reinhart-King (2010). "Exogenous and endogenous force regulation of endothelial cell behavior." Journal of Biomechanics **43**(1): 79-86.
- CDC (2010). Mortality by underlying and multiple cause, ages 18+: US, 1981-2007. Health Data Interactive, Centers for Disease Control and Prevention - National Center for Health Statistics.
- Charonko, J. (2009). Studies of Stented Arteries and Left Ventricular Diastolic Dysfunction Using Experimental and Clinical Analysis with Data Augmentation. Biomedical Engineering. Blacksburg, Virginia Polytechnic Institute and State University. **Doctor of Philosophy**: 241.
- Charonko, J., S. Karri, et al. (2009). "In Vitro, Time-Resolved PIV Comparison of the Effect of Stent Design on Wall Shear Stress." Annals of Biomedical Engineering **37**(7): 1310-1321.

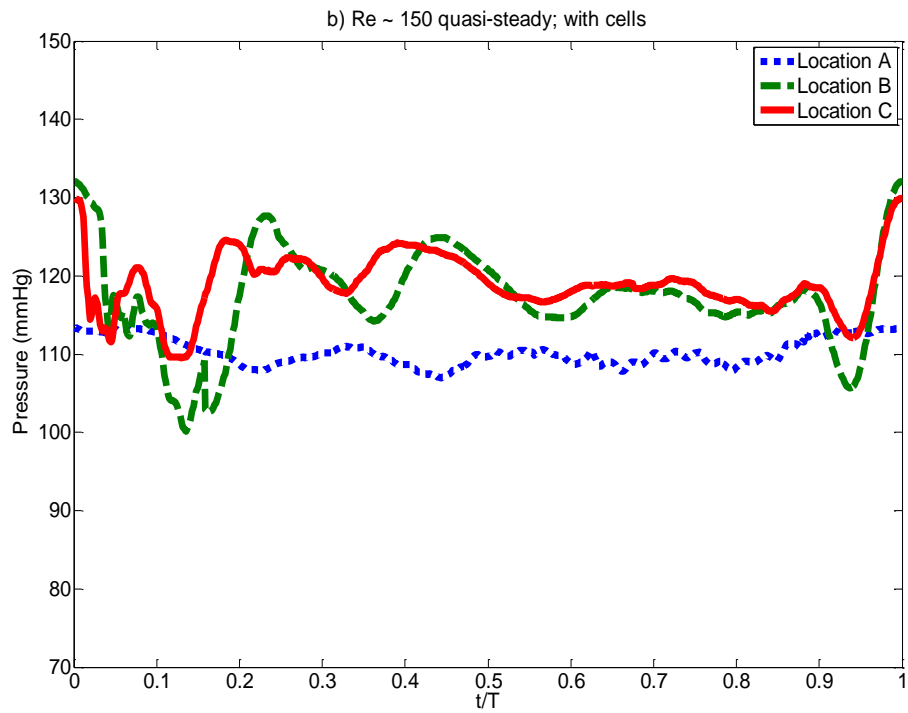
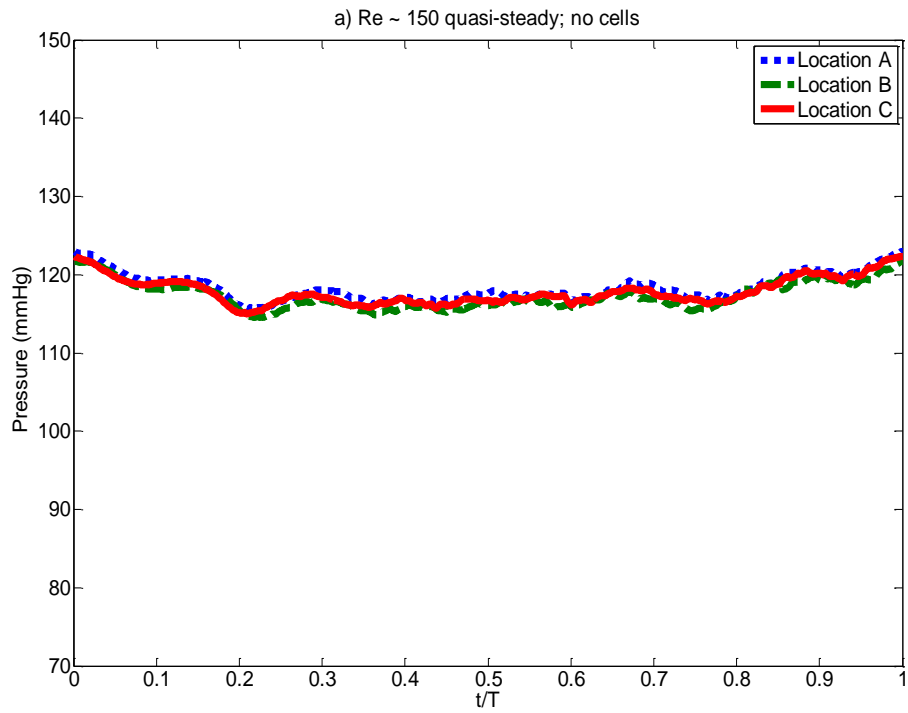
- Cole, R. T., C. L. Lucas, et al. (2005). "A LabVIEW (TM) model incorporating an open-loop arterial impedance and a closed-loop circulatory system." Annals of Biomedical Engineering **33**(11): 1555-1573.
- Conklin, B. S., S. M. Surowiec, et al. (2000). "A simple physiologic pulsatile perfusion system for the study of intact vascular tissue." Medical Engineering & Physics **22**(6): 441-449.
- Conlon, M. J., D. L. Russell, et al. (2006). "Development of a mathematical model of the human circulatory system." Annals of Biomedical Engineering **34**(9): 1400-1413.
- Decuzzi, P. and M. Ferrari (2006). "The adhesive strength of non-spherical particles mediated by specific interactions." Biomaterials **27**(30): 5307-5314.
- Decuzzi, P., S. Lee, et al. (2005). "A theoretical model for the margination of particles within blood vessels." Annals of Biomedical Engineering **33**(2): 179-190.
- Decuzzi, P., S. Lee, et al. (2004). "Adhesion of microfabricated particles on vascular endothelium: A parametric analysis." Annals of Biomedical Engineering **32**(6): 793-802.
- Eckstein, A. and P. P. Vlachos (2009). "Digital particle image velocimetry (DPIV) robust phase correlation." Measurement Science & Technology **20**(5): -.
- Fernandez, M. A., V. Milisic, et al. (2005). "Analysis of a geometrical multiscale blood flow model based on the coupling of ODEs and hyperbolic PDEs." Multiscale Modeling & Simulation **4**(1): 215-236.
- Ferrari, M. (2005). "Cancer nanotechnology: Opportunities and challenges." Nature Reviews Cancer **5**(3): 161-171.
- Fouras, A., J. Dusting, et al. (2007). "Three-dimensional synchrotron x-ray particle image velocimetry." Journal of Applied Physics **102**(6): -.
- Fung, Y. C. (1997). Biomechanics : circulation. New York, Springer.
- Gray, J. D., I. Owen, et al. (2007). "Dynamic scaling of unsteady shear-thinning non-Newtonian fluid flows in a large-scale model of a distal anastomosis." Experiments in Fluids **43**(4): 535-546.
- Hajitou, A., R. Pasqualini, et al. (2006). "Vascular targeting: Recent advances and therapeutic perspectives." Trends in Cardiovascular Medicine **16**(3): 80-88.
- Hirono, T., H. Arimoto, et al. (2008). "Microfluidic image cytometry for measuring number and sizes of biological cells flowing through a microchannel using the micro-PIV technique." Measurement Science & Technology **19**(2): -.

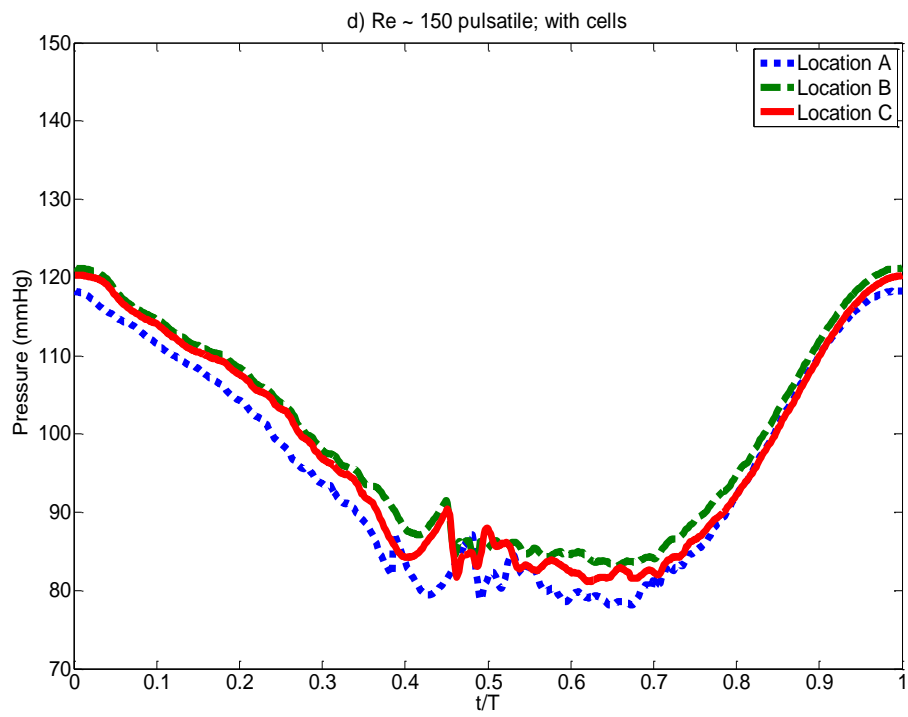
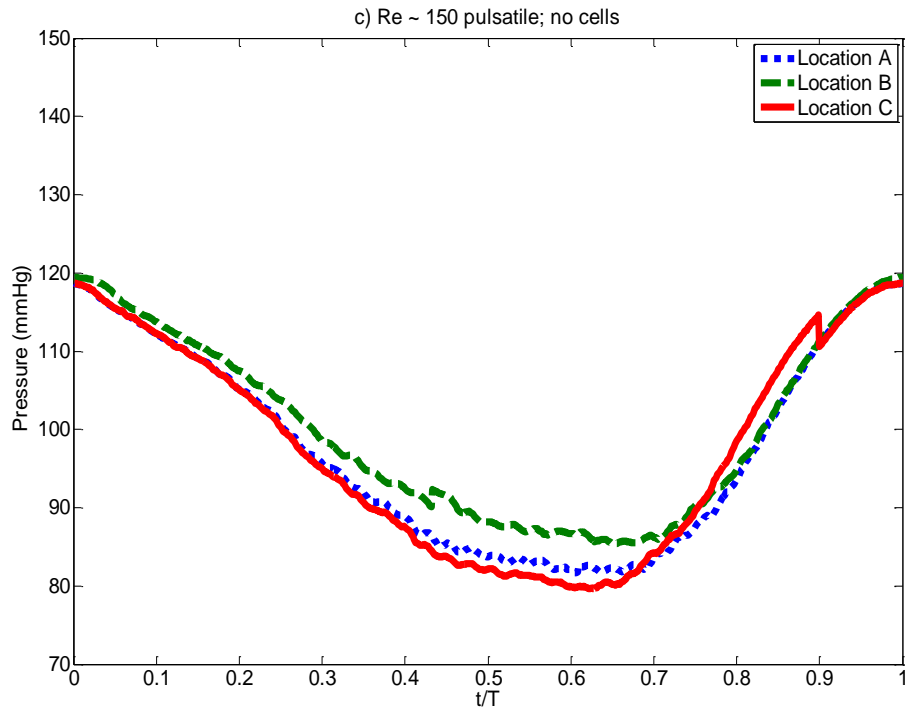
- Karri, S., J. Charonko, et al. (2009). "Robust wall gradient estimation using radial basis functions and proper orthogonal decomposition (POD) for particle image velocimetry (PIV) measured fields." Measurement Science & Technology **20**(4): -.
- Khalil, H. A., D. T. Kerr, et al. (2008). "Continuous flow total artificial heart: Modeling and feedback control in a mock circulatory system." Asaio Journal **54**(3): 249-255.
- Kleinstreuer, C., S. Hyun, et al. (2001). "Hemodynamic parameters and early intimal thickening in branching blood vessels." Critical Reviews in Biomedical Engineering **29**(1): 1-64.
- Ku, D. N. (1997). "Blood flow in arteries." Annual Review of Fluid Mechanics **29**: 399-434.
- Langer, R. (1990). "New Methods of Drug Delivery." Science **249**(4976): 1527-1533.
- Langer, R. (1998). "Drug delivery and targeting." Nature **392**(6679): 5-10.
- Lee, S. J. and G. B. Kim (2005). "Synchrotron microimaging technique for measuring the velocity fields of real blood flows." Journal of Applied Physics **97**(6): -.
- Levesque, M. J., R. M. Nerem, et al. (1990). "Vascular Endothelial-Cell Proliferation in Culture and the Influence of Flow." Biomaterials **11**(9): 702-707.
- Liang, F. Y. and H. Liu (2005). "A closed-loop lumped parameter computational model for human cardiovascular system." Jsm International Journal Series C-Mechanical Systems Machine Elements and Manufacturing **48**(4): 484-493.
- Lighthill, M. J. (1975). Mathematical biofluidynamics. Philadelphia, Society for Industrial and Applied Mathematics.
- Lin, P. H., C. Y. Chen, et al. (2000). "A porcine model of carotid artery thrombosis for thrombolytic therapy and angioplasty: Application of PTFE graft-induced stenosis." Journal of Endovascular Therapy **7**(3): 227-235.
- Liu, Z., C. Davis, et al. (2008). "Circulation and long-term fate of functionalized, biocompatible single-walled carbon nanotubes in mice probed by Raman spectroscopy." Proceedings of the National Academy of Sciences of the United States of America **105**(5): 1410-1415.
- Marassi, M., P. Castellini, et al. (2004). "Cardiac valve prosthesis flow performances measured by 2D and 3D-stereo particle image velocimetry." Experiments in Fluids **36**(1): 176-186.
- Martin, I., D. Wendt, et al. (2004). "The role of bioreactors in tissue engineering." Trends in Biotechnology **22**(2): 80-86.
- McDonald, D. A. (1974). Blood flow in arteries. Baltimore, Williams & Wilkins.

- Milisic, V. and A. Quarteroni (2004). "Analysis of lumped parameter models for blood flow simulations and their relation with 1D models." Esaim-Mathematical Modelling and Numerical Analysis-Modelisation Mathematique Et Analyse Numerique **38**(4): 613-632.
- Mironov, V., V. Kasyanov, et al. (2003). "Perfusion bioreactor for vascular tissue engineering with capacities for longitudinal stretch." Journal of Craniofacial Surgery **14**(3): 340-347.
- Murakami, T., K. Ajima, et al. (2004). "Drug-loaded carbon nanohorns: adsorption and release of dexamethasone in vitro." Mol Pharm **1**(6): 399-405.
- Neri, D. and R. Bicknell (2005). "Tumor vascular targeting." Nat. Cancer **570**: 436-446.
- Oppenheimer, S. B. (2006). "Cellular basis of cancer metastasis: A review of fundamentals and new advances." Acta Histochemica **108**(5): 327-334.
- Park, C. W., G. B. Kim, et al. (2004). "Micro-PIV measurements of blood flow in a microchannel." Optical Diagnostics and Sensing Iv **5325**: 70-77; 188.
- Pierrakos, O., P. P. Vlachos, et al. (2004). "Time-resolved DPIV analysis of vortex dynamics in a left ventricular model through bileaflet mechanical and porcine heart valve prostheses." Journal of Biomechanical Engineering-Transactions of the Asme **126**(6): 714-726.
- Poelma, C., P. Vennemann, et al. (2008). "In vivo blood flow and wall shear stress measurements in the vitelline network." Experiments in Fluids **45**(4): 703-713.
- Raffel, M. (2007). Particle image velocimetry : a practical guide. Heidelberg ; New York, Springer.
- Reneman, R. S., T. Arts, et al. (2006). "Wall shear stress - an important determinant of endothelial cell function and structure - in the arterial system in vivo." Journal of Vascular Research **43**(3): 251-269.
- Rossi, M. and I. Ekeberg (2006). In vitro study of shear stress over endothelial cells by Micro Particle Image Velocimetry (uPIV). 13th International Symposium on Applied Laser Techniques to Fluid Mechanics, Lisbon, Portugal.
- Sugii, Y., S. Nishio, et al. (2002). "In vivo PIV measurement of red blood cell velocity field in microvessels considering mesentery motion." Physiological Measurement **23**(2): 403-416.
- Takizawa, K., C. Moorman, et al. (2010). "Wall shear stress calculations in space-time finite element computation of arterial fluid-structure interactions." Computational Mechanics **46**(1): 31-41.

- Tanne, D., E. Bertrand, et al. (2008). "Asymmetric flows in an anatomical-shaped left atrium by 2C-3D+T PIV measurements." Computer Methods in Biomechanics and Biomedical Engineering **11**: 209-211.
- Vennemann, P., R. Lindken, et al. (2007). "In vivo whole-field blood velocity measurement techniques." Experiments in Fluids **42**(4): 495-511.
- Westerweel, J. (1997). "Fundamentals of digital particle image velocimetry." Measurement Science & Technology **8**(12): 1379-1392.
- Westerweel, J., D. Dabiri, et al. (1997). "The effect of a discrete window offset on the accuracy of cross-correlation analysis of digital PIV recordings." Experiments in Fluids **23**(1): 20-28.
- Westerweel, J. and F. Scarano (2005). "Universal outlier detection for PIV data." Experiments in Fluids **39**(6): 1096-1100.
- Wickline, S. A., A. M. Neubauer, et al. (2006). "Applications of nanotechnology to atherosclerosis, thrombosis, and vascular biology." Arteriosclerosis Thrombosis and Vascular Biology **26**(3): 435-441.
- Womersley, J. R. (1955). "Method for the calculation of velocity, rate of flow and viscous drag in arteries when the pressure gradient is known." J Physiol **127**(3): 553-563.
- Yazdani, S. and J. Berry (2009). "Development of an In Vitro System to Assess Stent-induced Smooth Muscle Cell Proliferation: A Feasibility Study." J Vasc Interv Radiol **20**: 101-106.
- Yazdani, S. K., J. E. Moore, et al. (2004). "DPIV measurements of flow disturbances in stented artery models: Adverse affects of compliance mismatch." Journal of Biomechanical Engineering-Transactions of the Asme **126**(5): 559-566.
- Yazdani, S. K., B. W. Tillman, et al. (2010). "The fate of an endothelium layer after preconditioning." Journal of Vascular Surgery **51**(1): 174-183.
- Zamir, M. (2000). The physics of pulsatile flow. New York, AIP Press ; Springer.

Appendix A: Additional Pressure Data





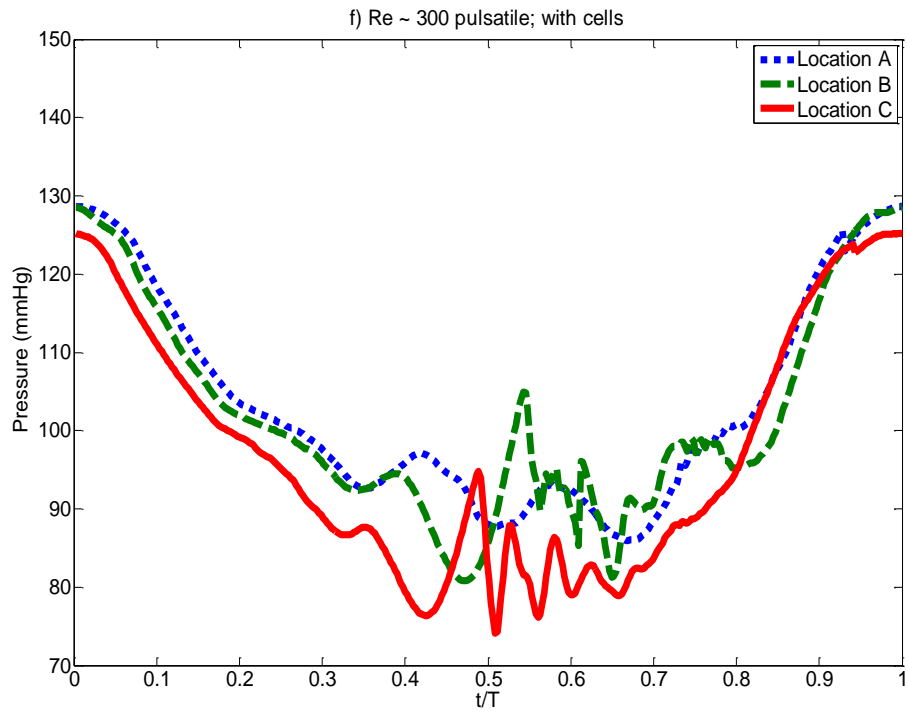
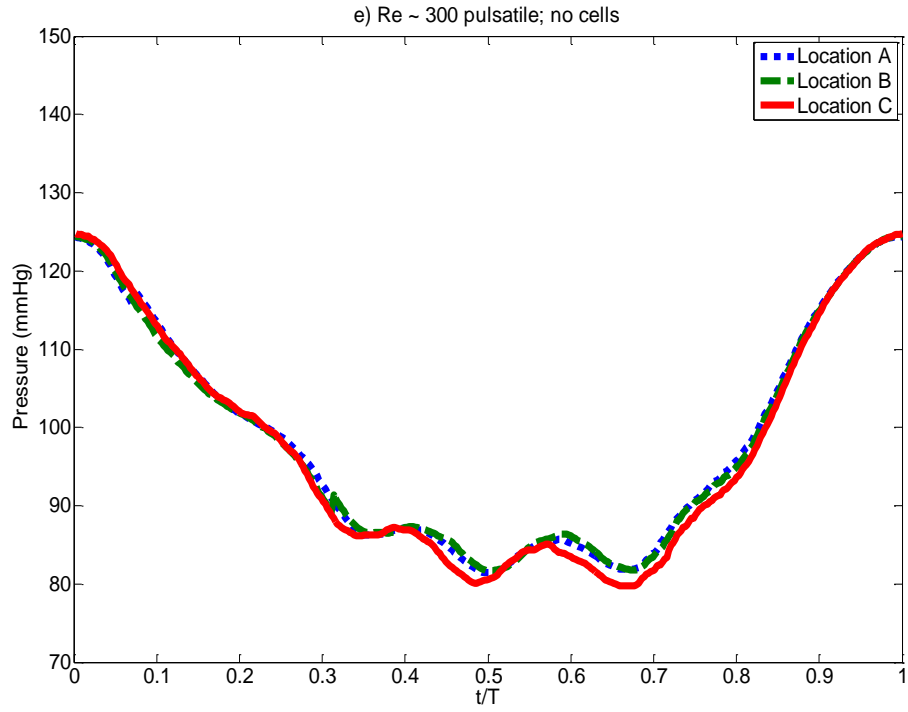
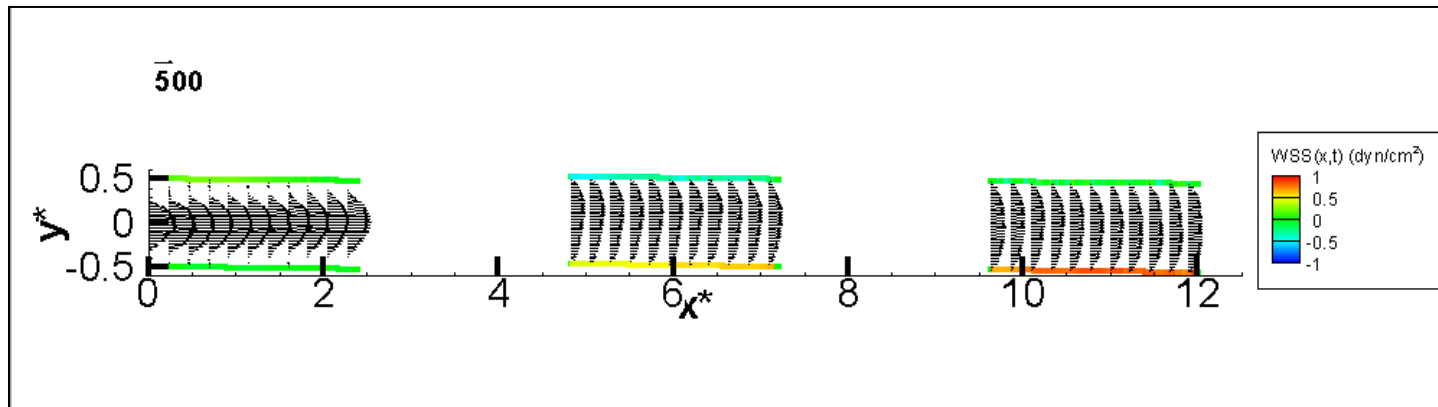


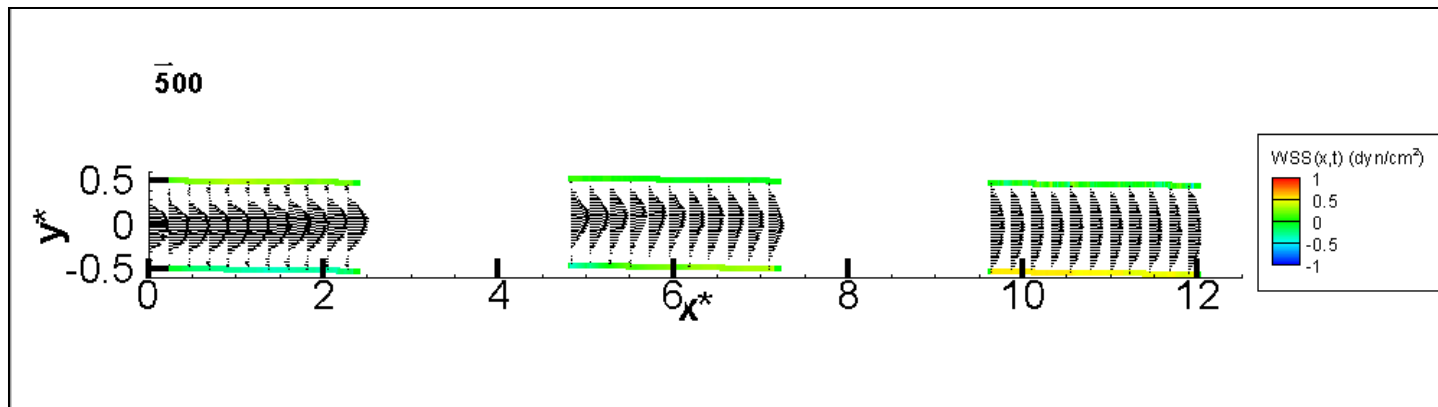
Figure	Test Description	Set flow rate (mL/min)	Resistor position	Re A/B/C	α	Diastolic Pressure (mmHg) A/B/C	Systolic Pressure (mmHg) A/B/C	MAP (mmHg) A/B/C
a	quasi-steady, no cells	35	Open	152	-	116	123	118
				150		114	122	117
				148		115	123	118
b	quasi-steady, with cells	35	Open	175	-	107	113	110
				158		103	132	118
				152		113	126	119
c	pulsatile, no cells	35	3.85	132	6.4	82	119	98
				150		86	119	100
				158		80	119	97
d	pulsatile, with cells	35	3.8	164	6.4	78	118	96
				155		83	121	99
				158		81	120	98
e	pulsatile, no cells	70	4.0	312	9.0	81	124	98
				304		81	124	98
				310		79	125	98
f	pulsatile, with cells	70	4.0	325	9.0	86	129	103
				315		74	128	102
				326		75	125	97

Appendix B: Additional Figures

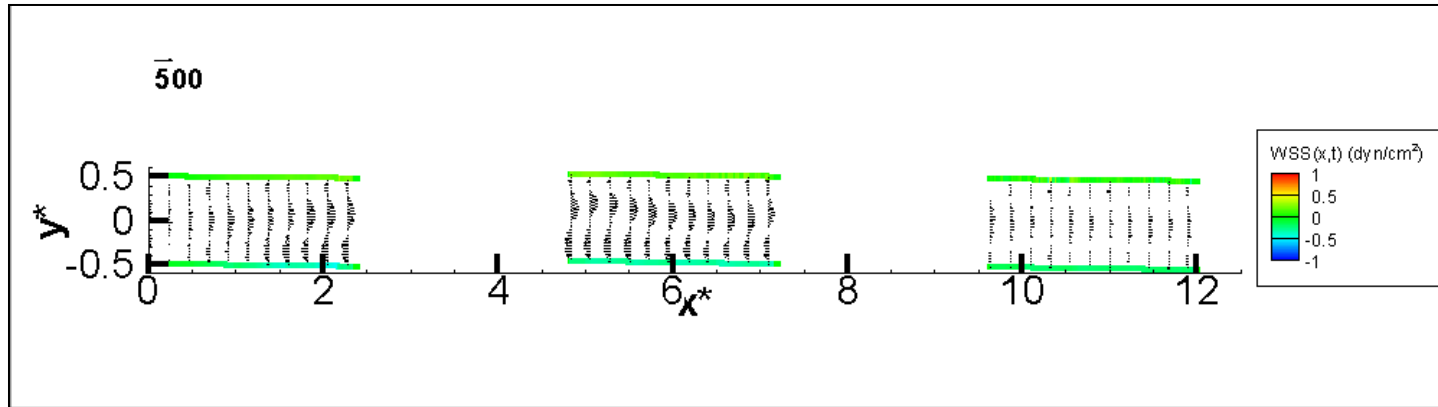
B.1 Time Variation of Velocity and Instantaneous WSS



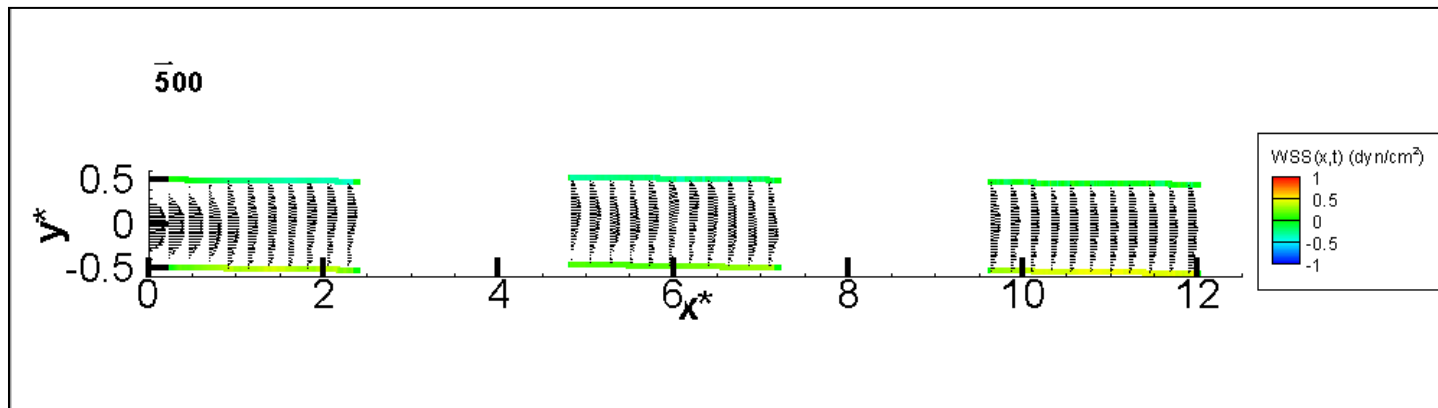
$Re \sim 150$ quasi-steady; no cells; $t = 0$.



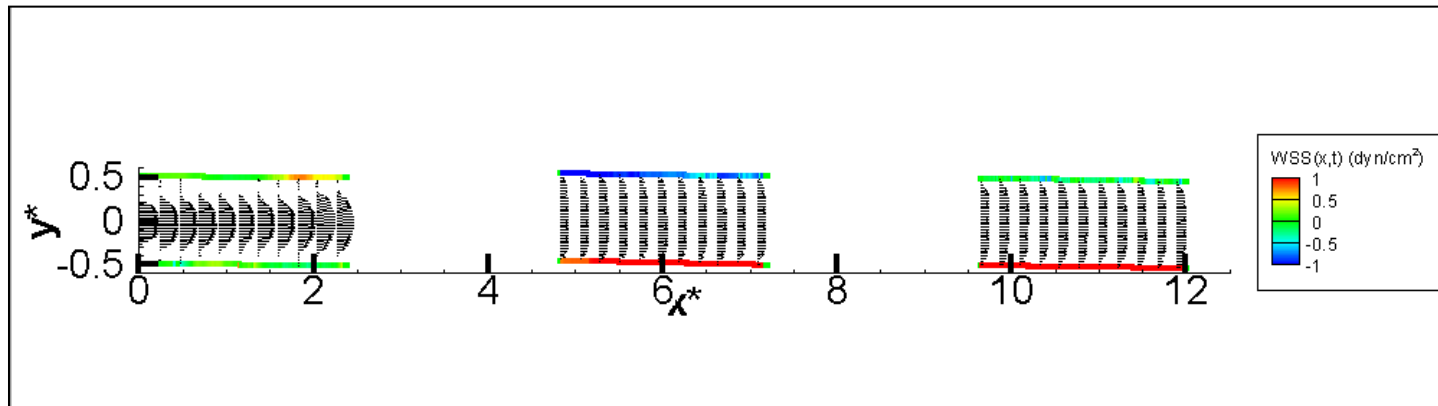
$Re \sim 150$ quasi-steady; no cells; $t = T/4$.



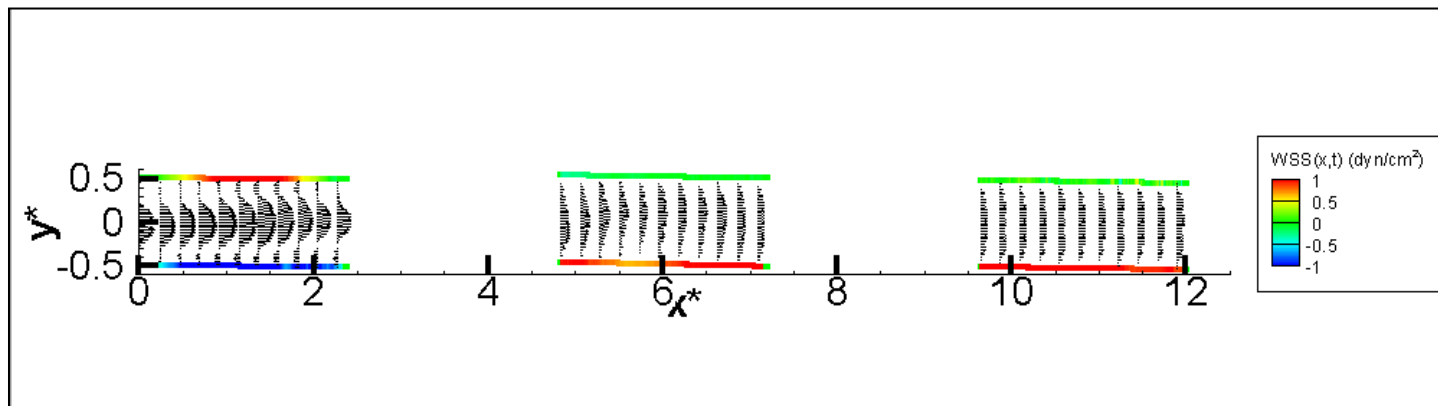
$Re \sim 150$ quasi-steady; no cells; $t = T/2$.



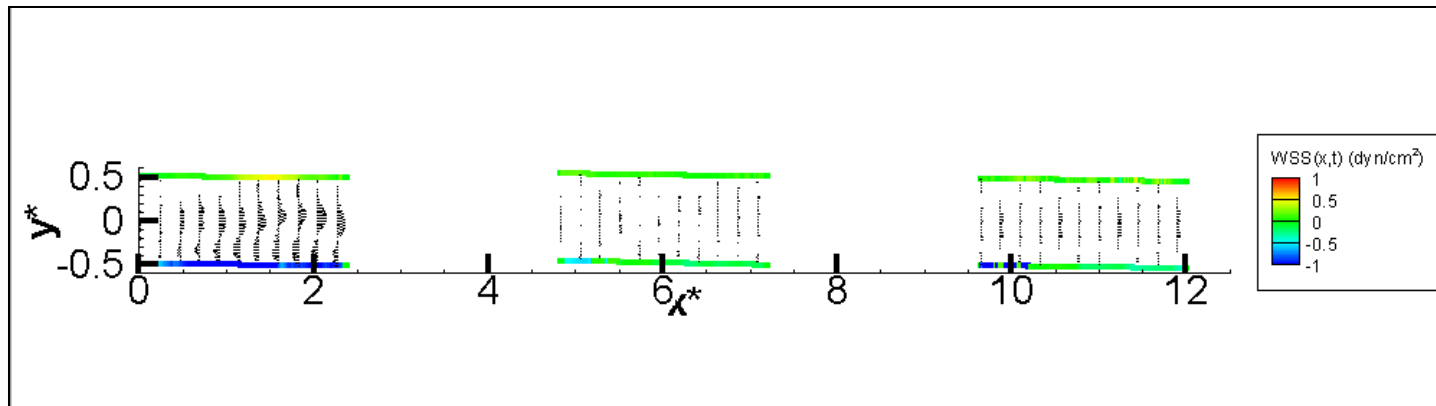
$Re \sim 150$ quasi-steady; no cells; $t = 3T/4$.



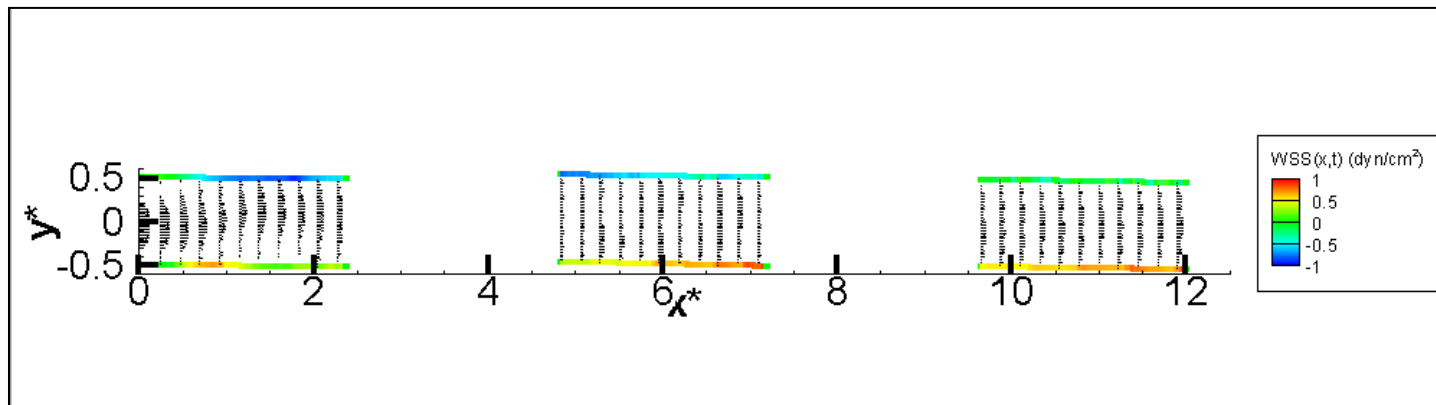
Re ~ 300 pulsatile; no cells; $t = 0$.



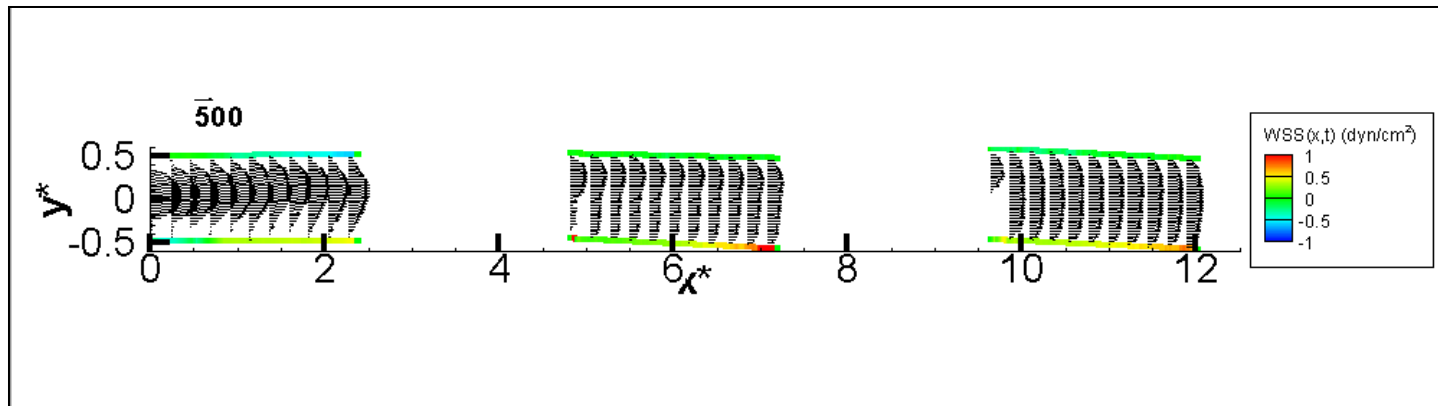
Re ~ 300 pulsatile; no cells; $t = T/4$.



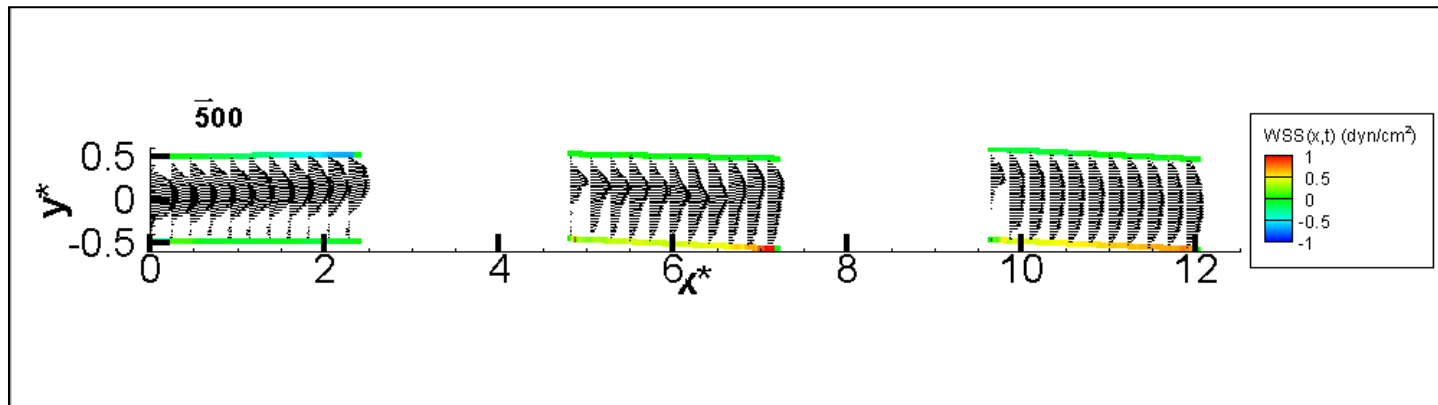
Re ~ 300 pulsatile; no cells; $t = T/2$.



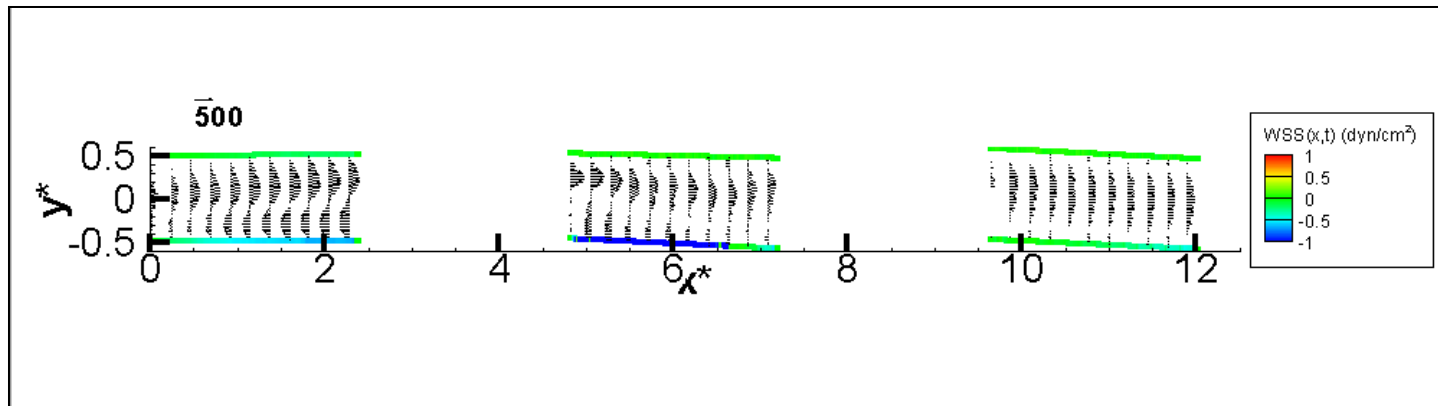
Re ~ 300 pulsatile; no cells; $t = 3T/4$.



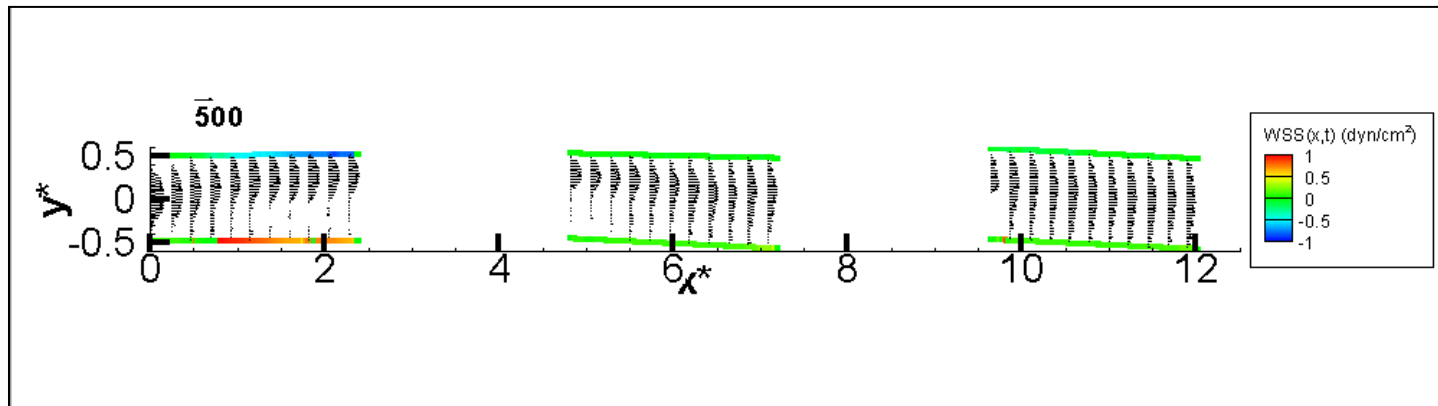
Re ~ 150 pulsatile; with cells; $t = 0$.



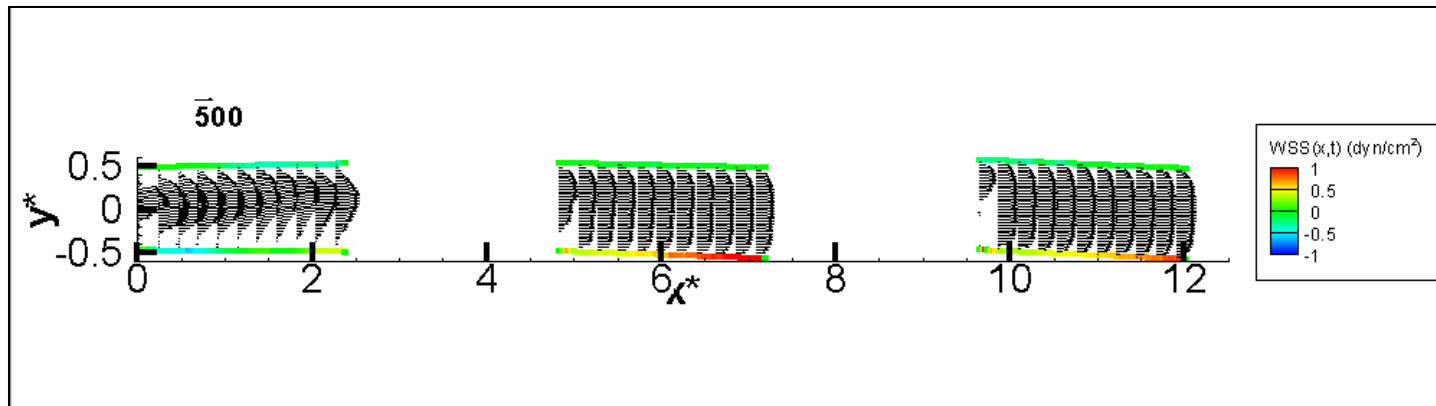
Re ~ 150 pulsatile; with cells; $t = T/4$.



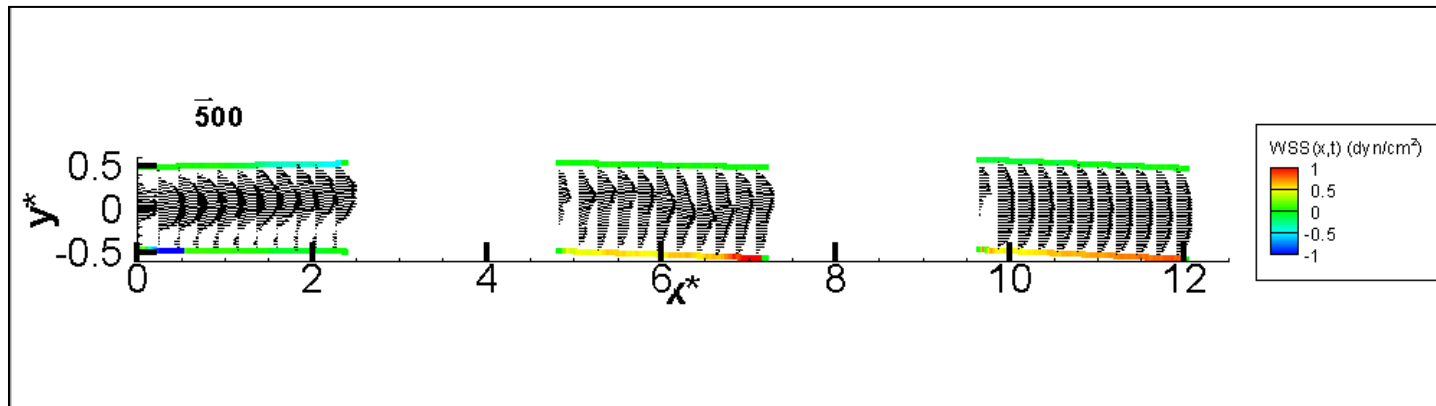
Re ~ 150 pulsatile; with cells; $t = T/2$.



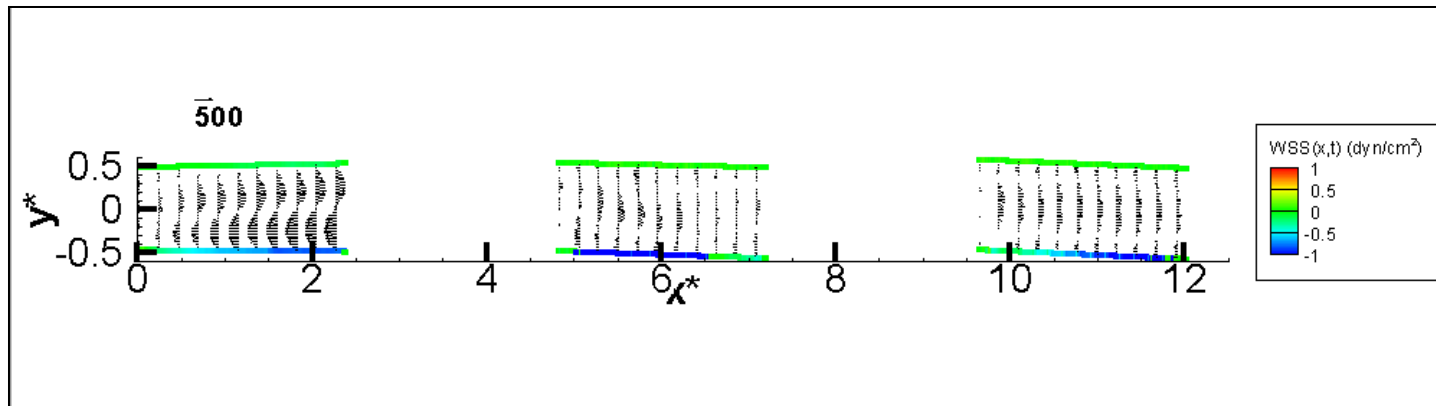
Re ~ 150 pulsatile; with cells; $t = 3T/4$.



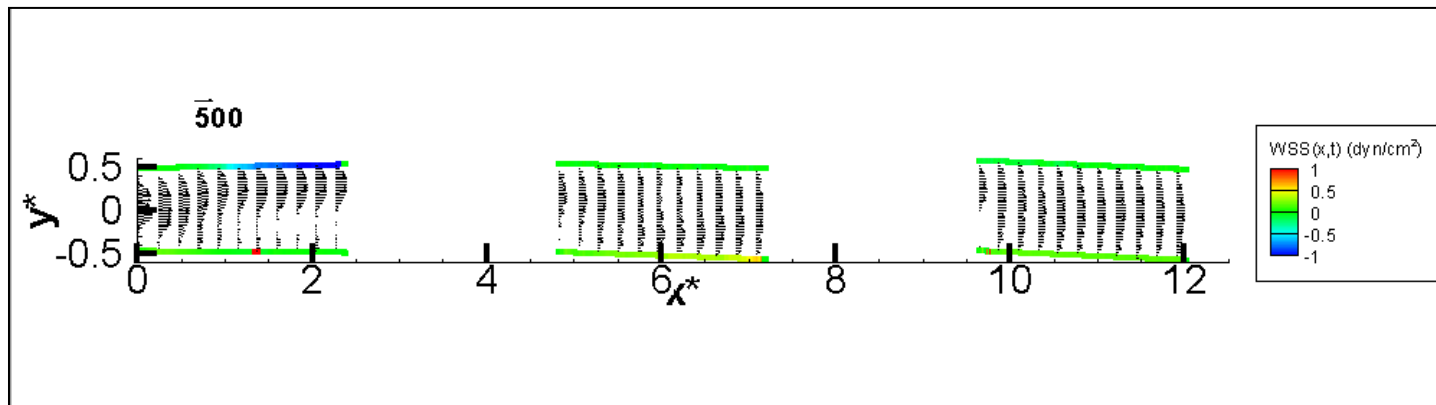
Re ~ 150 quasi-steady; with cells; t = 0.



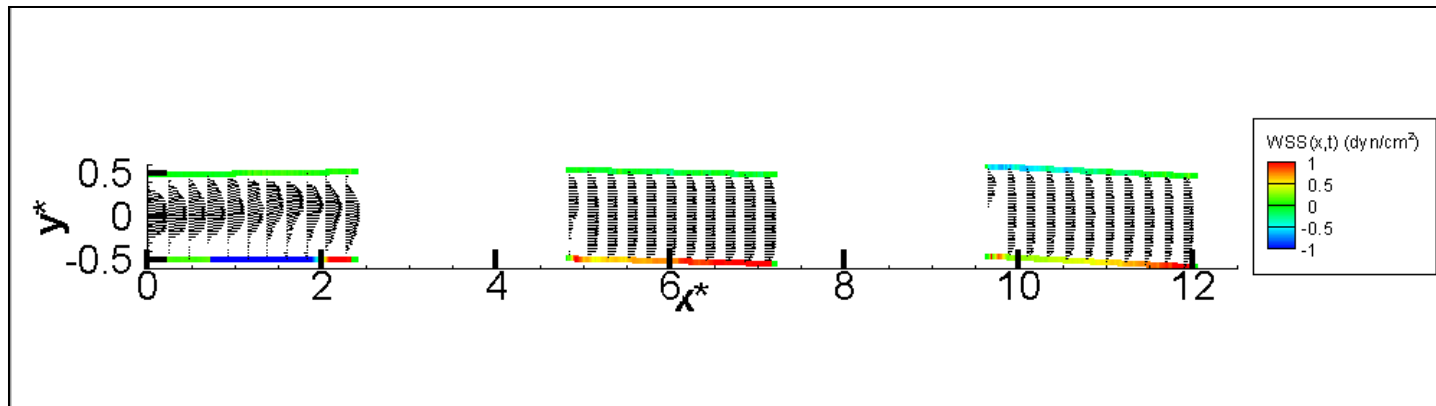
Re ~ 150 quasi-steady; with cells; t = T/4.



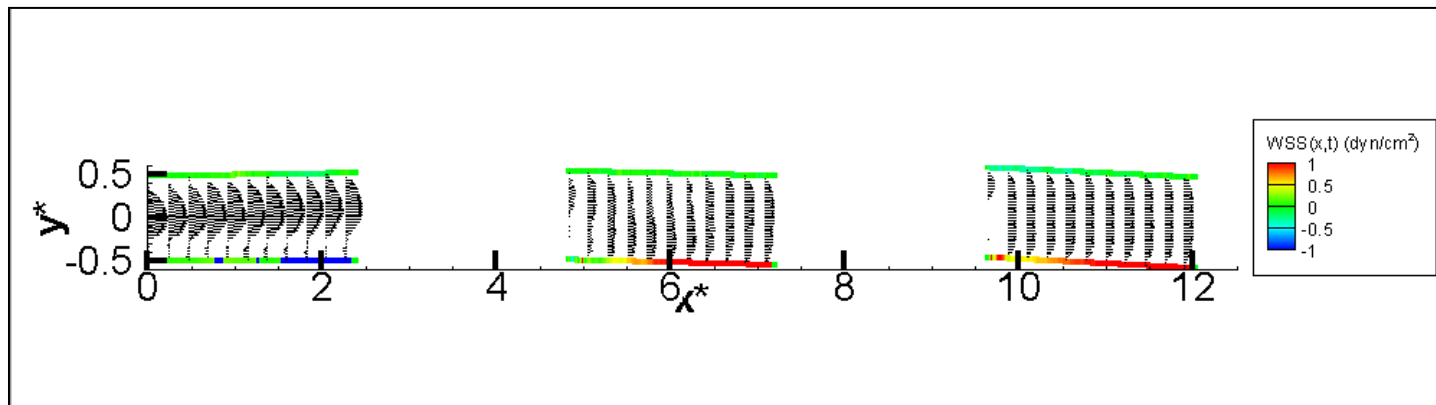
Re ~ 150 quasi-steady; with cells; $t = T/2$.



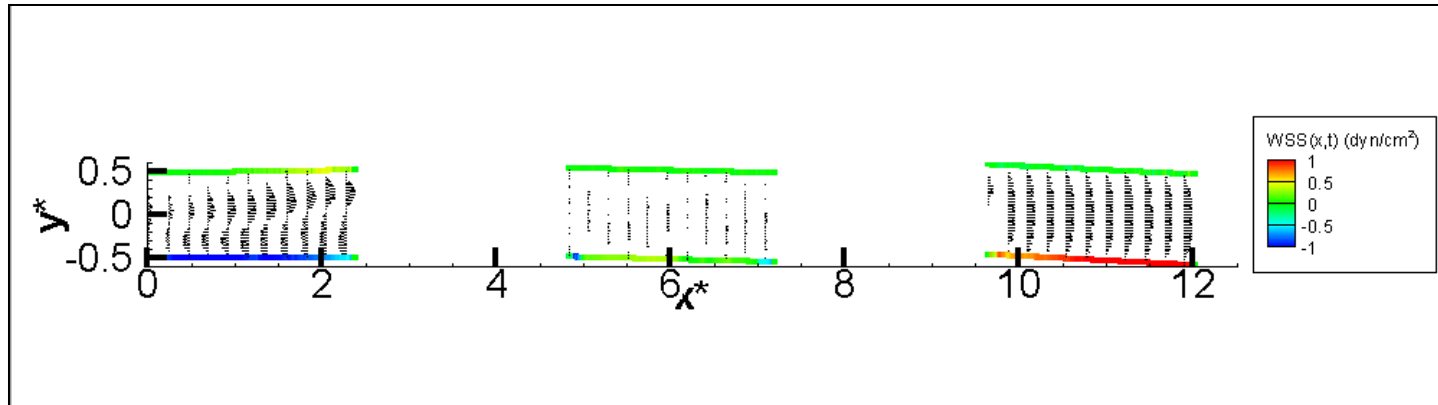
Re ~ 150 quasi-steady; with cells; $t = 3T/4$.



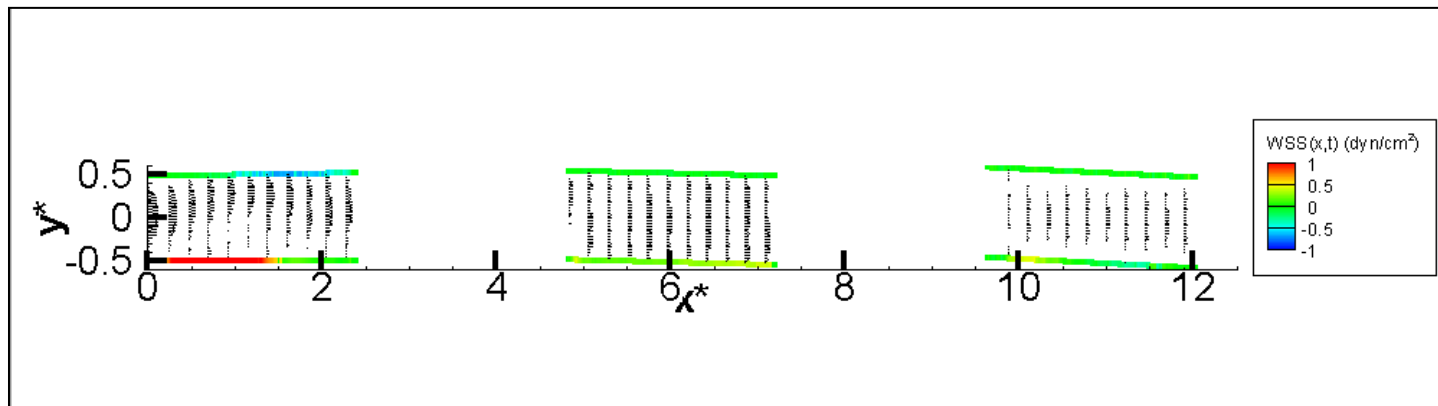
Re ~ 300 pulsatile; with cells; $t = 0$.



Re ~ 300 pulsatile; with cells; $t = T/4$.



Re ~ 300 pulsatile; with cells; $t = T/2$.



Re ~ 300 pulsatile; with cells; $t = 3T/4$.

B.2 Statistical Variation of OSI and Time-Averaged WSS

